

CZECH TECHNICAL UNIVERSITY IN PRAGUE

Faculty of Nuclear Science and Physical Engineering

Am/Co photoelectron source for energy scale
monitoring of the KATRIN neutrino experiment

PhD Thesis

Jaromir Kaspar

Supervisor: Ing. Otokar Dragoun, DrSc.

2008

Declaration

Hereby I declare that this dissertation is a result of my own work, except where explicit reference to the work of others is made, and has not been formerly submitted to another university for degree purposes.

Content

1	Introduction	9
2	Neutrino mass and Katrin	11
2.1	Neutrinos	11
2.1.1	Neutrino characteristics	11
2.1.2	Neutrino mass	12
2.2	KATRIN overview	14
2.2.1	WGTS	15
2.2.2	Differential and cryogenic pumping, electron transport system	16
2.2.3	Spectrometers	16
2.2.4	Detector concept	19
2.2.5	Background	19
2.2.6	Systematics	20
2.3	The KATRIN model	21
2.3.1	Differential beta spectrum	21
2.3.2	Response function	22
3	Energy scale monitoring	23
3.1	Monitor spectrometer concept	26
3.2	Sources of mono-energetic electrons	28
3.3	Optimal distribution of measurement time and points	31
3.3.1	Distribution of the measurement time	31
3.3.2	Distribution of measurement points	33
3.4	Statistics used to analyze Am/Co data	34
3.4.1	Hypothesis testing	34
3.4.2	Neutrino mass systematics caused by an energy scale bias	39
3.4.3	Differential spectrometer	41
3.4.4	Integrating spectrometer	43
3.4.5	Conclusion	45
3.5	Statistics used to analyze Kr lines	46
3.5.1	Preassigned values	46

3.5.2	Differential spectrometer	47
3.5.3	Integrating spectrometer	52
3.5.4	Conclusion	54
3.6	Outlook on statistical methods	55
4	Experiments	59
4.1	First $^{83}\text{Rb}/^{83\text{m}}\text{Kr}$ measurements at Mainz	59
4.1.1	Rb/Kr source	59
4.1.2	Mainz spectrometer setup	60
4.1.3	Results	65
4.1.4	Conclusions of the $^{83}\text{Rb}/^{83\text{m}}\text{Kr}$ measurements	68
4.2	Am/Co measurements at Rez	71
4.2.1	ESA12 spectrometer setup	71
4.2.2	$5\ \mu\text{m}$ Co converter	72
4.2.3	$3\ \mu\text{m}$ Co converter	74
4.2.4	$0.1\ \mu\text{m}$ Co converter	76
4.2.5	Ar etching	77
4.2.6	Conclusions of the Rez measurements	80
4.3	Am/Co measurements at Mainz	81
4.3.1	^{57}Co check	82
4.3.2	Adiabatic mode of the Mainz spectrometer	85
4.3.3	Turning nonadiabatic	89
4.3.4	Ar etching of a Co foil	91
4.3.5	Nonadiabatic mode of the Mainz spectrometer	95
4.3.6	Conclusions of the Mainz $^{241}\text{Am}/\text{Co}$ measurements	97
4.4	Voltage stability & divider calibration in NPI Rez	99
4.5	Long term stability of the ESA 12 electrostatic spectrometer	104
4.5.1	Principles of the method	104
4.5.2	The initial measurements	105
4.5.3	Changed dividing ratio	107
4.5.4	Changed line position	108
4.5.5	Stability of the line position	108
4.5.6	Examples	110
4.5.7	Conclusions and outlook	111
5	Summary	113
6	Conclusions	117
A	Optimal measurement time and point distributions	119
B	Multiple background peaks	131
B.1	Multiple background peaks at Mainz	131

B.2	Experimental evidence	131
B.3	Understanding the effect	133
B.3.1	Not an electronic effect	133
B.3.2	An oscilloscope look	133
B.3.3	Independence of count rate	133
B.3.4	Mirroring effects	137
B.3.5	Shaping time	137
B.3.6	Energy resolution	137
B.3.7	Beam diameter	140
B.3.8	Adiabacity	140
B.3.9	Screening voltage	142
B.4	True secondary electrons	145
B.4.1	Probability of the process	145
B.4.2	A simulation mockup	146
B.5	Conclusion	150
	References	151
	Acknowledgement	155

1 Introduction

KATRIN is a next generation tritium beta decay experiment to measure the neutrino mass with a design sensitivity of 0.2 eV (90 % c.l.). In contrast to neutrinoless double beta decay and cosmological studies, KATRIN will provide a completely model-independent measurement of the neutrino mass. The success of the KATRIN experiment relies on the long-term stability of the energy scale on the metrological level. Therefore, in addition to a measurement of retarding high voltage with the highest available precision, KATRIN plans to utilize a monitor spectrometer of the same type as the main one to check the stability. Several sources of monoenergetic electrons to serve in the monitor spectrometer are being developed in parallel.

The aim of the thesis is a feasibility study of a $^{241}\text{Am}/\text{Co}$ photoelectron source in context of monitoring of the KATRIN experiment. Idealistically, we could use a perfectly stable and precise electric equipment to develop standards of monoenergetic electrons, in particular the $^{241}\text{Am}/\text{Co}$ source. When the standards will be ready, we will consider them stable further on, and will use them to monitor the electric equipment. Unfortunately, this is not realistic. Such the electric devices do not exist. Therefore we will develop both the electron standards and electric equipment in parallel, cross-checking each other. And redundancy will be crucial in this approach.

The report is organized as follows: In the second chapter, the present status of the neutrino physics is sketched, and the KATRIN experiment briefly described including both the setup and simulation.

In the third chapter, monitoring of the KATRIN experiment is introduced, with another section dedicated to the concept of the monitor spectrometer leading to a section devoted to an Am/Co photoelectron source. The KATRIN description is completed with a section on the optimal measurement time distribution. Statistical test suitable to report on stability of energy scale are introduced in a dedicated sections. General approach to statistical test in the framework of KATRIN monitoring is discussed at the end of the chapter.

The fourth chapter is devoted to experimental evidence obtained with spectrometers in Rez and Mainz. Starting with a section on $^{83}\text{Rb}/^{83\text{m}}\text{Kr}$, the Mainz electron spectrometer proved to be a reliable monitor spectrometer. Then, preliminary test of the $^{241}\text{Am}/\text{Co}$ concept with ESA12 spectrometer in Rez is covered, followed by the main section on $^{241}\text{Am}/\text{Co}$ measurements with the Mainz spectrometer with

an increased energy resolution up to 1 eV at an energy region of interest. The main section is followed by several dedicated studies of subtle issues influencing monitoring concept: starting with voltage stability and divider calibration in Rez, up to an outlook study on long term stability of the ESA12 spectrometer.

2 Neutrino mass and Katrin

2.1 Neutrinos

Proposed by Pauli in 1930 to save the energy conservation law, and discovered by Reines & Cowan in 1956 neutrinos entered physics [1, 2] being massless, chargeless, and spin half particles.

2.1.1 Neutrino characteristics

Neutrinos are artificially produced by reactors, accelerators, and nuclear bombs. Geological neutrinos are part of natural background radiation. Atmospheric neutrinos are secondary particles produced by cosmic radiation hitting the atmosphere. Solar neutrinos originate from fusion powering stars, in particular the Sun. Neutrinos are as well produced by some types of supernovæ. And finally, there is background of low energy neutrinos in our Universe left from the Big Bang.

As reported by [3], electroweak measurements performed with data taken at the Z resonance by the experiments operating at the electron-positron colliders SLC and LEP, the number of neutrino flavors is determined to be 2.9840 ± 0.0082 [3], in agreement with the three observed generations of fundamental fermions.

Like all other particles of matter, neutrinos have antimatter partners. Unlike any other fermion, the neutrinos and antineutrinos may in fact be the same particle known as Majorana. (Dirac particles are the cases, if particles and antiparticles are not the same.) The neutrinoless double beta decay would be the ultimate proof of Majorana nature of neutrinos. Even more, observation of the neutrinoless double beta decay would prove that the total lepton number is not conserved, and would prove nonvanishing neutrino mass.

Thanks to oscillation experiments, especially Super-Kamiokande, Kamland, and SNO, we have learned recently that neutrinos have mass, and can mix. Assuming [4] three active mixed neutrinos, the conserved CPT, and the pure vacuum origin of the neutrino mass, solar neutrinos and reactor experiments report on Δm_{12}^2 , and ϑ_{12} (solar sector) (i.e., the mass squared difference and the mixing angle of the first

and the second neutrino mass eigenstates), atmospheric neutrinos and accelerator experiments are sensitive to Δm_{23}^2 , and ϑ_{23} (i.e., the mass squared difference and the mixing angle of the second and the third neutrino mass eigenstates), and the CHOOZ experiment explores the ϑ_{13} sector. Daya Bay reactor experiment is going to focus on ϑ_{13} mixing angle.

Neutrinos fit nicely into the standard model framework. MiniBoone has already disfavored LSND results [5], finding nothing behind the framework of the standard model. The data are consistent with no nonstandard oscillations within a two-neutrino appearance-only oscillation model. The result excludes nonstandard two neutrino appearance-only oscillations as an explanation of the LSND anomaly at 98% CL, if the oscillations of neutrinos and antineutrinos are the same.

The story of neutrinos continues to be written raising the next question. Oscillations tell us about mass differences, but what about the masses themselves?

2.1.2 Neutrino mass

The bounds on neutrino mass come from cosmology and lab experiments. Neutrino masses are small, compared to the masses of their charged partners.

In [6] bounds on the neutrino mass were studied using new data from the WMAP (3 year data), the SDSS observation of the baryon acoustic peak, the Type Ia supernovae from SNLS, and the Lyman- α forest. In the most general cosmological models assumed, the 95% C.L. bound on the sum of neutrino masses is $\sum m_\nu \leq 0.62$ eV. Assuming more conservative cosmological models, the bound on neutrino masses is $\sum m_\nu = 0.48$ eV (95% C.L.), if the Lyman- α data are ignored. If the Lyman- α data are kept in the analysis, then the upper limit on neutrino masses is $\sum m_\nu \leq 0.2 - 0.4$ eV (95% C.L.), depending strongly on the Lyman- α analysis used.

Future cosmological data will be sensitive to the effects of the finite sum of the neutrino masses even as small as ~ 0.06 eV [7], the lower limit guaranteed by present neutrino oscillation experiments.

Lab experiments to determinate the neutrino mass include oscillation experiments, neutrinoless double decay experiments, and direct kinematical searches. Oscillation experiments report on difference of neutrino mass eigenstates. The mass splitting from atmospheric neutrino oscillations amounts [4] $|\Delta m_{23}^2| = (2.4 \pm 0.3) \times 10^{-3}$ eV², (1σ C.L.). The splitting of $\Delta m_{12}^2 = (7.9 \pm 0.4) \times 10^{-5}$ eV² (1σ C.L.) is responsible for the solar neutrino oscillations.

No experiment has observed the neutrinoless double beta decay so far, except for the claim [8] by a part of the Heidelberg-Moscow collaboration. Many experiments with design sensitivities in the range of 100–500 meV are being operated

at the moment. The summary is given e.g. in [2, 9]. Experiments to cover the neutrino mass region of 20–55 meV are in development or construction phase, e.g. SuperNEMO (30–50 meV), Majorana, EXO, and CUORE.

Direct kinematic searches came to upper limits of the neutrino mass of 2.3 eV (95 % C.L.) [10], and 2.05 eV (95 % C.L.) [11]. Both experiments relied on tritium beta decay, and integrating electrostatic spectrometers.

New generation of experiments is aiming to measure the neutrino mass. In particular, KATRIN [12] would like to find out what the neutrino masses are, or at least significantly improve the upper limit. If no neutrino mass signal is observed, the upper limit will be $m_\nu < 0.2 \text{ eV}/c^2$ (90 % c.l.) In the case of a positive signal, the KATRIN reference design has a discovery potential of 5σ (3σ) for the neutrino mass of $m_\nu = 0.35 \text{ eV}/c^2$ ($m_\nu = 0.3 \text{ eV}/c^2$). For the total measurement time of 1 000 days, both the statistical and systematical uncertainties contribute about equally.

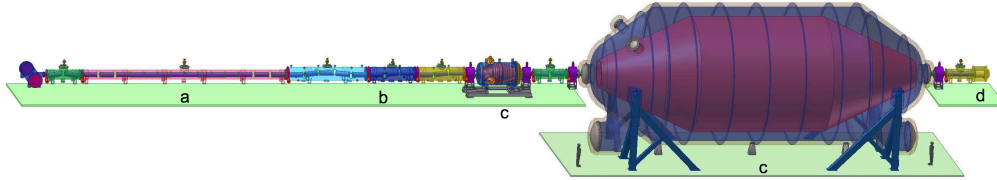


Figure 2.1 The 70 m long KATRIN reference setup with its major components: a) the windowless gaseous tritium source WGTS, b) the transport elements, consisting of an active pumping part and a passive cryotrapping section, c) the two electrostatic spectrometers and d) the detector for β -counting (not shown is the monitor spectrometer).

2.2 KATRIN overview

The Karlsruhe Tritium Neutrino (KATRIN) experiment [13, 14, 12] is the next-generation tritium beta decay experiment with a sensitivity to sub-eV neutrino masses. The sensitivity on the electron neutrino is expected to be $m_\nu \leq 0.20$ eV (90 % c.l.), which is about one order of magnitude better than the sensitivity of the best current experiments [11, 10]. The equipment used in the KATRIN experiment can be subdivided into five functional units:

- a high luminosity windowless gaseous tritium source (WGTS) delivering 10^{10} beta decay electrons per second
- an active differential pumping section at the rear and front side of the WGTS to reduce the flow of tritium molecules from the WGTS into the rest of the system
- a cryotrapping section with Ar-frost to eliminate the remaining flow of tritium molecules and to keep the spectrometer essentially tritium-free
- a system of two electrostatic filters consisting of a pre-spectrometer at fixed retarding potential, which filters out low energy beta decay electrons and a large volume main spectrometer, which analyses the beta electrons close to the tritium endpoint at 18.6 keV
- a segmented semiconductor detector to count the beta electrons transmitted through the electrostatic filters

2.2.1 WGTS

The main working principle of the WGTS is adiabatic transportation of beta decay electrons from a long tube, which is filled with tritium and is differentially pumped out on both ends of the tube with injection of tritium at the middle of it. The WGTS will be a 10 m long cylindrical tube of 90 mm diameter, filled with molecular tritium gas of high isotopic purity ($> 95\%$). The tritium gas density at the middle of the tube will be 10^{15} molecules cm^{-3} . A working temperature around 30 K and a constant injection rate both stabilized to $\pm 0.1\%$ degrees will keep the source strength constant. The tritium tube will be placed inside a chain of superconducting solenoids of 1 m length each, generating homogenous magnetic field of $B_S = 3.6$ T.

The main advantages of the WGTS are as follows:

- practically no smearing or blurring of the investigated tritium beta spectrum, except for the spectrum of final state vibrational and rotational excitations of the daughter molecular ion (${}^3\text{HeT}^+$)
- guaranteed homogeneity of density over the whole source cross section
- use of a high specific activity
- no perturbing solid state effects
- a possibility to measure the energy loss spectrum of electrons inelastically scattered in the source

On the other side, the possible problems are:

- stability of the source strength
- magnetic trapping of charged particles in the local magnetic field minima between the solenoids of the source
- tritium penetration to the spectrometer volume

Apart from the standard long-term measurements of the tritium beta spectrum, other specific modes of the tritium source operation may be required:

- energy loss measurements of 18.6 keV electrons in the WGTS, i.e. the mode providing information on energy loss spectrum, as well as the total inelastic cross section of electrons at this energy. The cross section uncertainty could be the dominating systematic error in the KATRIN measurements
- energy calibration with gaseous ${}^{83\text{m}}\text{Kr}$. The calibration lines of our interest are K-32 conversion line at the electron energy of 17.8 keV, the L-32 lines at 30.4 keV and the N-32 lines at 32.1 keV. Estimated krypton-tritium ratio of the order of 10^{-6} and the WGTS temperature of 100–150 K will be used in this mode

2.2.2 Differential and cryogenic pumping, electron transport system

The electron transport system guides beta decay electrons to spectrometer, which has to be kept tritium free mostly for background reasons. The tritium flow into the spectrometer is required to be smaller than 2.7×10^6 molecules s^{-1} to limit the relevant background contribution to 1 mHz.

More than 99.9 % of tritium molecules are eliminated in this first differential pumping section, which is followed – in the direction pointing to pre-spectrometer – by the second differential pumping section. Additional 0.04 % of tritium molecules are removed in this section.

In the next parts of transport section, both cryotrapping ones, all the remaining tritium molecules will be trapped onto the liquid helium cold surface of the transport system covered by a thin layer of argon snow and surrounded by the homogenous magnetic field ($B = 5.6 \text{ T}$).

99 % of the removed tritium molecules will be immediately returned to the inner tritium loop of the WGTS, remaining approximately 1 % molecules will be recovered by isotope separation in the Tritium Labor Karlsruhe, in order to guarantee tritium purity of 95% or better.

2.2.3 Spectrometers

2.2.3.1 MAC-E-Filter

MAC-E-Filter (Magnetic Adiabatic Collimation combined with an Electrostatic Filter) is a type of spectrometers, that combine high luminosity and low background with a high resolution, both essential to measure neutrino mass from the endpoint region of a beta decay spectrum.

In general, MAC-E-Filter consists of two superconducting magnets placed on both sides of a cascading system of cylindrical electrodes. The beta electrons coming from the source through the entry superconducting solenoid are guided magnetically on a cyclotron motion around the magnetic field lines into the spectrometer. Then, the magnetic field drops by several orders of magnitude between the superconducting solenoid and the central plane of the spectrometer, and transforms most of the transversal (cyclotron) electron energy E_{\perp} into longitudinal motion. The distance between solenoids and central analyzing plane of spectrometer is chosen in such a way, that the magnetic field B varies slowly enough, so the electron momentum transforms adiabatically and therefore the magnetic moment μ keeps constant

$$\mu = \frac{E_{\perp}}{B} = \text{const} \quad . \quad (2.1)$$

So, at the central area of spectrometer, all the electrons fly almost parallel to magnetic field lines, forming a broad beam of area given by conserving magnetic field flow as

$$A_A = A_S \cdot \frac{B_S}{B_A} \quad , \quad (2.2)$$

with A_A being the analyzing plane area, A_S being the effective source area, B_S and B_A being magnetic fields at the source area and the analyzing plane, respectively. This electron beam flies against the electrostatic potential formed by a system of cylindrical electrodes. Those electrons, which pass the electrostatic barrier are accelerated and guided onto a detector, the other ones are reflected. This forms an integrating high-energy pass filter.

Magnetic field at the WGTS is chosen to eliminate electrons which have a very long path within the WGTS and therefore their kinetic energy suffers from systematic uncertainty. Due to the magnetic mirror effect, the magnetic field B_S in the WGTS, the magnetic field B_{\max} at the entry to the spectrometer and the maximum accepted starting angle of electrons ϑ_{\max} fulfill [15]

$$\sin \vartheta_{\max} = \sqrt{\frac{B_S}{B_{\max}}} \quad , \quad (2.3)$$

An important characteristics of the MAC-E-Filter is the transmission function $R(E, T)$, i.e. the function form telling what fraction of electrons with the initial kinetic energy E pass through the central spectrometer plane, if they are being retarded by voltage T/e .

The residual transversal energy E_{\perp} at the spectrometer analyzing plane is

$$E_{\perp} = E \cdot \sin^2 \vartheta \cdot \frac{B_A}{B_S} \quad , \quad (2.4)$$

with E being the initial kinetic energy of the electron and ϑ being the electron starting angle in the source. In order to pass through the electrostatic barrier the electron has to fulfill

$$E - E_{\perp} > T \quad , \quad (2.5)$$

i.e.,

$$\sin^2 \vartheta < \frac{E - T}{E} \cdot \frac{B_S}{B_A} \quad . \quad (2.6)$$

Assuming isotropic beta decay and with respect to eq. (2.3), the spectrometer transmission function can be written as

$$R(E, T) = \frac{1 - \cos \vartheta}{1 - \cos \vartheta_{\max}} \quad . \quad (2.7)$$

Denoting ΔE the maximal residual transversal energy (2.4) (the energy resolution of the spectrometer)

$$\Delta E = E \cdot \sin^2 \vartheta_{\max} \cdot \frac{B_A}{B_S} = E \cdot \frac{B_A}{B_{\max}} \quad , \quad (2.8)$$

the transmission function can be expressed as

$$R(E, T) = \begin{cases} 0 & E - T < 0 \\ \frac{1 - \sqrt{1 - \frac{E-T}{E} \cdot \frac{B_S}{B_A}}}{1 - \sqrt{1 - \frac{\Delta E}{E} \cdot \frac{B_S}{B_A}}} & 0 \leq E - T \leq \Delta E \\ 1 & E - T > \Delta E \end{cases} \quad . \quad (2.9)$$

2.2.3.2 Pre-spectrometer

The cryotrapping sections will be followed by a MAC-E-Filter type prespectrometer. There are two tasks for the prespectrometer in the KATRIN experiment:

- pre-filter, rejecting all the beta electrons except the ones in the region of our interest close to the beta spectrum endpoint
- fast switch, to keep a possible option to run the main spectrometer in a time of flight mode.

The prespectrometer is a cylindrical tank 3.42 m long and 1.70 m wide in the inner diameter. These dimensions have been fixed by the electromagnetic design, especially focused on

- the magnetic fields, which should guarantee the energy resolution $\Delta E < 50$ eV, whole magnetic flux transportation and adiabaticity
- eliminating local inhomogeneities of the electrostatic potential
- avoiding discharges
- removing particles caught in electromagnetic traps (additional dipole electrode for active trap cleaning)

2.2.3.3 Main spectrometer

The KATRIN key part is the large MAC-E-Filter with the diameter of 10 m and the overall length of about 20 m, which will allow us to scan the endpoint region of the tritium beta spectrum with high luminosity and the resolution better than 1 eV. This is reached by combination of superconducting solenoids $B_{\max} = 6$ T at the entry and the exit of the spectrometer vessel and an air coil at the central spectrometer plane producing the magnetic field of 3×10^{-4} T.

Electromagnetic design was done with a special care to

- removing of trapped particles, that seem to play an important role with respect to background. An additional wired electrode capable to work in both

monopole and dipole regime was added to the spectrometer design to sweep the trapped particles away. The principle of removing is based on adiabatic drift, caused by the electrostatic field perpendicular to the magnetic field.

- ideal adiabatic transport conditions. The aim is to suppress all the local magnetic and electrostatic inhomogeneities violating the adiabatic energy transformation, which is crucial here.

2.2.4 Detector concept

The detector requirements can be summed up as follows:

- high efficiency for electron detection
- low gamma background
- capability to operate at high magnetic fields
- the energy resolution better than 600 eV for electron energies at the beta spectrum endpoint
- a reasonable time resolution (better than 100 ns)
- position resolution
- possibility to absorb high count rates

A segmented PIN-Diode array is the leading candidate designed for the KATRIN experiment, in a dart board configuration with 148 segments including a bull's eye with four segments. The detector will operate with electron energies in range from 5 to 50 keV. Made from a 500 μm wafer, the detector could exhibit a dead layer as thin as 50 μm .

2.2.5 Background

The background signal is mostly dominated by:

- environmental radioactivity and cosmic rays around the detector. This background can be suppressed by shielding and the proper choice of materials. An anti-coincidence veto will be applied as well.
- tritium decays in the main spectrometers, that can be decreased under the acceptable limit by a tritium partial pressure $\simeq 10^{-20}$ mbar in the spectrometer.
- the secondary and tertiary charged particles and ions created by cosmic rays penetration into the spectrometer and scattering inside the spectrometer. Again,

a strict limit on the spectrometer vacuum can effectively suppress this contribution to background.

- trapped particles, that can be reduced by careful electrostatic and magnetic design using additional dipole electrodes inside the spectrometer.

2.2.6 Systematics

The main sources of systematic errors that the KATRIN experiment suffers from are:

- inelastic scattering. Note that the electron energy loss function in the tritium source (see (2.14) below) is dependent on 6 parameters, that are given by fit (see [16]) and make this systematic error the dominant one in the experiment.
- uncertainty in column density and homogeneity of the tritium source. This uncertainty can be reduced by isotopic purity checked by online mass spectrometry in the backward direction of the WGTS.
- $^3\text{HeT}^+$ molecule final states. An excitation energy of the first electronic excited state of the $^3\text{HeT}^+$ molecule is 27 eV. Therefore the only uncertainty comes from rotational-vibrational excitations of the daughter molecule ground state. Fortunately, both theoretical and experimental knowledge of these excitations is good.
- transmission function. The theoretical transmission function (2.9) we use does not include fluctuations of magnetic fields as well as electrostatic analyzing plane inhomogeneities, synchrotron radiation and doppler broadening. Anyway, all these effects will be finally included in the beta spectrum shape.
- trapped electrons in the WGTS and the differential pumping section. Note that we are not able to avoid local minima of the magnetic field in the WGTS and the transportation section and therefore we cannot get rid of electrons scattered on these trapped particles with slightly changed energy and momentum.
- energy scale imperfections caused by wrong calibration or time instabilities of voltmeters and a high voltage divider. This kind of systematic errors can be reduced by independent monitoring by e.g. a measurement of the K-32 conversion line of $^{83\text{m}}\text{Kr}$.

2.3 The KATRIN model

KATRIN is not being operated at the moment. So, we used simulation to estimate what results of the experiment could look like. In this section, we describe a model and algorithms we used for the KATRIN experiment simulation. Later, we are going to show that the physical predictions given by our model are in good agreement with the generally expected ones, and that the algorithms we used are accurate enough.

An integrated beta spectrum as measured by MAC-E-Filter is given by the formula

$$S(T, Q, m_\nu) = \int_0^\infty \beta(E, Q, m_\nu) R'(E, T) dE \quad , \quad (2.10)$$

where $\beta(E, Q, m_\nu)$ is a differential beta spectrum (2.11), $R'(E, T)$ denotes the spectrometer response function (2.13), T is the energy determined by a retarding voltage, Q stands for the maximum electron kinetic energy assuming a massless neutrino and m_ν is the neutrino rest mass.

2.3.1 Differential beta spectrum

$$\begin{aligned} \beta(E, Q, m_\nu) = & N_s F(Z, E) \sqrt{E(E + 2m_e c^2)} (E + m_e c^2) \times \\ & \times \sum_i \omega_i (Q - W_i - E) \sqrt{(Q - W_i - E)^2 - m_\nu^2 c^4} \times \quad , \quad (2.11) \\ & \times \Theta(Q - W_i - E - m_\nu c^2) \end{aligned}$$

with N_s denoting norm of spectrum, $F(Z, E)$ being the Fermi function (2.12), Θ standing for the Heaviside (step) function guaranteeing the energy conservation law, E denoting an electron kinetic energy, m_e being the electron rest mass, W_i standing for the i -th rotational-vibrational energy level of the daughter molecule, and ω_i being the probability of the transition to this level. The Fermi function can be approximated as

$$F(Z, E) = \frac{x}{1 - \exp(-x)} \left(a_0 + a_1 \frac{v_e}{c} \right) \quad x = \frac{2\pi Z \alpha c}{v_e} \quad , \quad (2.12)$$

with Z equal to 2 in our case, the fine-structure constant α , an electron velocity v_e , the speed of light in vacuum c , including the empirical values $a_0 = 1.002037$ and $a_1 = -0.001427$.

2.3.2 Response function

$$R'(E, T) = \int_0^{E-T} R(E - \varepsilon, T) \times (P_0 \delta(\varepsilon) + P_1 f(\varepsilon) + P_2 (f \otimes f)(\varepsilon) + \dots) d\varepsilon \quad , \quad (2.13)$$

where $R(E, T)$ is the theoretical instrumental transmission function (2.9) of the spectrometer, $f(\varepsilon)$ defines an electron energy loss function in gaseous tritium and P_i is the probability of an electron to be scattered i times. δ represents the Dirac δ -function and the \otimes symbol denotes convolution.

The energy loss function is approximated by

$$f(\varepsilon) = \begin{cases} A_1 \exp\left(-\frac{2(\varepsilon-\varepsilon_1)^2}{\omega_1^2}\right) & \text{for } \varepsilon < \varepsilon_c \\ A_2 \frac{\omega_2^2}{\omega_2^2 + 4(\varepsilon-\varepsilon_2)^2} & \text{for } \varepsilon \geq \varepsilon_c \end{cases} \quad , \quad (2.14)$$

The parameters $A_{1,2}$, $\varepsilon_{1,2}$, $\omega_{1,2}$ describe an amplitude, a mean value position and a deviation of the Gaussian and the Lorentzian, resp. The matching point ε_c is chosen in such a way that the loss function is continuous.

Further details of the KATRIN simulation are covered in [12, 17], including the standard set of parameters.

3 Energy scale monitoring

As stated above, the beta particles are analyzed by two spectrometers of MAC-E-Filter type. The determination of the neutrino mass from the measurements of the tritium β -spectrum requires for each event the precise knowledge of the energy retarded at the analyzing plane of the main spectrometer. This energy is determined by the retarding electrostatic potential at the analyzing plane and the scanning potential applied to the electron source.

To illustrate the required precision of retarded energy, we can estimate the systematic shift of the measured neutrino mass squared m_ν^2 caused by an unknown Gaussian smearing of the tritium spectrum with the variance of σ^2 as [18]

$$\Delta m_\nu^2 = -2 \cdot \sigma^2 \quad . \quad (3.1)$$

Restricting the systematic effect down to 0.005 eV^2 , we require the stability of the retarding voltage of 50 mV for at least three years data taking. A more detailed study on energy scale imperfections can be found in our study [17]. From that study, two tables are shown to demonstrate what an effect of energy scale imperfections could be.

In tab. 3.1 an effect of a step variation of energy an energy scale bias is given. The simulated data were recorded with an energy scale for a half of the measurement time of 3 years. Then, the energy scale was shifted by δ , and the remaining data were recorded for the second half of the measurement time. Finally, the simulated data were fitted with the energy scale fixed.

δ [eV]	$\overline{m}_\nu - m_\nu$ [eV]
1.00	-0.8017
0.50	-0.3765
0.30	-0.2203
0.10	-0.0718
0.05	-0.0358
0.03	-0.0218
0.01	-0.0050

Table 3.1 A step variation of an energy scale bias. δ stands for the energy scale bias, m_ν represents the initial neutrino mass, and \overline{m}_ν is the fit value.

In tab. 3.2 an effect of a Gaussian blur of the energy scale is studied, which is another variant of a time dependent bias of the energy scale, probably the more realistic one. In this case, the time for which a biased spectrum is measured, is function of the bias, and the function form is Gaussian.

δ [eV]	$\bar{m}_\nu - m_\nu$ [eV]
0.50	-0.7892
0.30	-0.4517
0.10	-0.1435
0.05	-0.0709
0.03	-0.0423
0.01	-0.0140

Table 3.2 A Gaussian blur of an energy scale bias. δ stays for the deviation of energy scale bias, m_ν represents the initial neutrino mass, and \bar{m}_ν is the fit value.

During all the simulations 10 mHz background and an uniform distribution of the measurement time were used. The results are independent of the measurement time. The fictitious neutrino mass created by the Gaussian blur follows the theoretical formula (3.1). The imperfection of the bias step is more critical from the point of stability and monitoring of the energy scale of the KATRIN experiment, and practically covers disturbing effects like dividing ratio jump, time drift of voltmeters, and/or common mode currents.

KATRIN will utilize several methods to monitor the retarding potential of the main spectrometer to achieve a high degree of redundancy:

- direct retarding voltage measurements
- direct calibration of the main spectrometer
- monitor spectrometer (covered in a dedicated section)

Direct retarding voltage measurements

The retarding voltage of the main spectrometer will be reduced by a precision high-voltage divider down to a voltage below 10 V, which is the most convenient for state of the art high-precision voltmeters. Suitable metrological voltmeters are commercially available with a precision and a long-term stability at the ppm-level. Commercial voltage dividers have a long-term stability and precision in the range of tens ppm, which is not enough for the KATRIN needs.

KATRIN collaboration developed and constructed a high precision high voltage divider in cooperation with PTB in Braunschweig aiming for a long-term stability

and precision at the 1 ppm level for a maximum voltage of 35 kV. The divider is in operation since November, 2005. In combination with the best available high voltage power supplies, it proved a long-term stability better than 0.88 ppm (October 2006, upper limit on 90 % c.l.) [19], and the reproducibility of 0.1 ppm. Further, the divider exhibits very small voltage dependence of 0.032 ppm/kV, and short warm-up time.

However, KATRIN can not rely on electrical equipment only, because of the total measurement time of five calendar years.

Direct calibration of the main spectrometer

Spectroscopy of sharp monoenergetic lines from a gaseous source will be done with the KATRIN main spectrometer to absolutely calibrate the retarding energy under measurement conditions. The absolute calibration is necessary not only to check the stability of all monitor systems, but also to compare the endpoint energy obtained by evaluating the measured tritium β spectrum with the helium-tritium mass difference, determined by cyclotron resonance measurements in Penning traps. Any significant difference would point towards an unrecognized systematic error.

It's not just an energy scale to be calibrated in order to achieve compatible and reproducible β spectra, there are many others, e.g. dead layer of the detector, electric and magnetic field profiles at the analyzing plane of the main spectrometer, work function stability of the wire electrodes, pressure profile and temperature stability of the WGTS, space charge stability within the WGTS, and T₂ isotopic purity to name just few of them. In this work, energy scale monitoring is the only one covered.

To summarize, we apply voltage to retarding electrodes and being measured in the KATRIN experiment, and we plug electron energy into the β spectrum formula. Matching the voltage and the energy together we call *calibration*. We have no serious physical motivation for the calibration. A bias of 10 eV would create a fictitious neutrino mass of 1 μ eV. On the other side, stability of the calibration, which is called *monitoring*, is critical for KATRIN. Whatever way we have matched voltage and energy together, that is the way we have to do it always. The experiment can not rely on electrical equipment only.

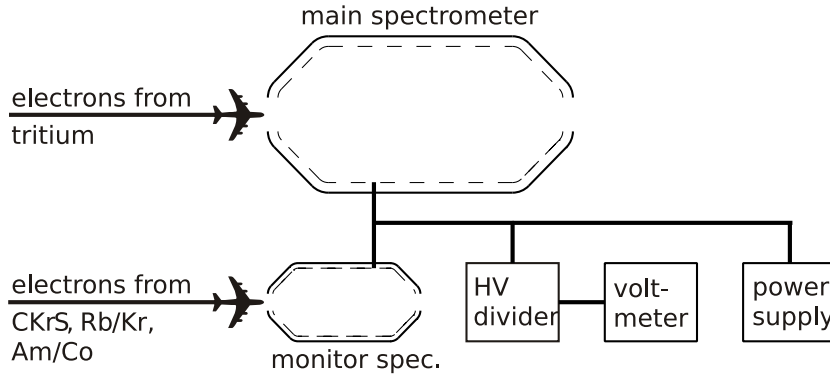


Figure 3.1 A setup of the monitor spectrometer beam line with a calibration source following an atomic/nuclear standard and fed with the main spectrometer retarding potential.

3.1 Monitor spectrometer concept

Calibration measurements in the main system can not run at the same time as the tritium measurements. However, it is critical to monitor the stability of the energy scale in parallel to tritium measurements. The idea is to apply the retarding voltage of the KATRIN main spectrometer to the monitor spectrometer (see fig. 3.1) of the same MAC-E-Filter type. A well-defined, sharp, and stable source of monoenergetic electrons will be scanned by varying the voltage applied directly to it. Assuming stability of the electron source and the monitor spectrometer, stability of the electron line refers directly to stability of the retarding voltage applied.

Fortunately, the MAC-E-Filter spectrometer of the Mainz Neutrino Mass Experiment [10] is available for KATRIN. During the tritium measurements in Mainz, it was operated with a moderate energy resolution of 4.8 eV, the value which has been chosen as a compromise between energy resolution and luminosity. For KATRIN we would like to upgrade the energy resolution of the existing Mainz spectrometer down to about 1 eV. The corresponding reduction on luminosity does not play a role for calibration and monitoring purposes. Sources of mono-energetic electrons has to be developed anyway, then they can be produced with reasonably small area to fit the improved resolution of the monitor spectrometer.

From our point of view, a simplified setup of the Mainz spectrometer could serve as the monitor spectrometer. There is no need of the inner wire electrodes to suppress background. The detector magnet is not needed as well, because of the same reason. All these are just personal comments and recommendations motivated by long term stability of the setup, that has to be proved and guaranteed.

Assuming stable spectrometer setup and stable electron source, and equipped with the electron line measured, following actions make sense:

- to correct the energy scale of the main spectrometer by the measured position of a monitoring line. This necessarily introduces the systematic error of the energy scale equal to the total uncertainty (statistic and systematic) of the line position measured. It can be quite hard to keep the total uncertainty on 90% c.l. below the acceptable limit, due to a short time available. The short time comes from stability of electrical equipment used to determine the scanning voltage applied to the electron source, and stability of spectrometer itself.
- throw out beta spectra measured at the moment when the energy scale is unstable. Then the energy scale suffers from a systematic uncertainty equal to the error of the second kind of the electron line position. Number of unused beta spectra is driven by the error of the first kind of the same quantity. Practically, the throwing out of beta spectra may be done by grouping the beta spectra, if the number of groups is reasonably small. The improvement has been achieved due to much better substrate and ^{83m}Kr film control, laser ablation and ellipsometry. The main advantage of the method is independence of the line position itself. Any quantity or measure relating to the line position may be used, and even more many of them in parallel. Later, we offer some suitable classical statistical tests, and a general framework how to find more dedicated ones.
- anything in between, e.i., group data and correct for the line position inside the particular group, or the other way round: correct the whole groups for the line position, and keep the beta spectra inside the particular groups untouched. With the latter looking quite promising. Anyway in both cases, systematic error of the energy scale may be tricky to estimate.

3.2 Sources of mono-energetic electrons

In the section, stable electron sources of mono-energetic electrons are introduced. The sources of mono-energetic lines should be defined by atomic and nuclear standards, because of the line width and line stability. And electron lines should lay in the tritium endpoint region of about 18 575 eV. We consider the following ones:

- conversion electrons from $^{83\text{m}}\text{Kr}$ in various physical states: the K-conversion electron line of the 32 keV transition in ^{83}Kr (K-32) has an energy of 17.8 keV and a natural width of 2.8 eV [20]. The energy differs by 0.8 keV from the endpoint of the tritium beta spectrum. Even more, the L_3 -32 line with an energy of 30.5 keV and a width of 1.2 eV is highly useful for systematic studies. The half-life of $^{83\text{m}}\text{Kr}$ is only 1.83 h.

Gaseous $^{83\text{m}}\text{Kr}$ source is planned to study the distribution of space charge within the windowless tritium source, and to absolutely calibrate the energy scale. Only the gaseous source can do the job, because of work functions, space charge within the source, and energy losses in the source. And $^{83\text{m}}\text{Kr}$ source is the only one acceptable even in spite of higher operating temperature of about 120 K and necessity of results extrapolation down to work temperature of tritium source of 27 K.

Condensed $^{83\text{m}}\text{Kr}$ source was used by the Mainz Neutrino Mass experiment very successfully. Thanks to an improved reproducibility it is a leading candidate for a monitoring source. The improvement has been achieved due to much better substrate and $^{83\text{m}}\text{Kr}$ film control, laser ablation and ellipsometry. The main advantage of the source is a possibility to place it in the mean beamline of the KATRIN experiment without a worry of a contamination of the main spectrometer, thanks to the short half-life.

To avoid the repeated condensation of $^{83\text{m}}\text{Kr}$ a *solid $^{83}\text{Rb}/^{83\text{m}}\text{Kr}$ electron source* is under development benefiting the ^{83}Rb half-life of 86 days. A possible small contamination of the monitor spectrometer with ^{83}Rb represents no problem, because the background is not critical. Long-term stability of $^{83}\text{Rb}/^{83\text{m}}\text{Kr}$ sources is being studied, as well as the ways how to slow down ^{83}Kr release from a thin layer of vacuum evaporated ^{83}Rb . Since spring 2005 about 18 $^{83}\text{Rb}/^{83\text{m}}\text{Kr}$ sources have been evaporated from ^{83}Rb produced by the cyclotron in Rez. The stability studies include measurements with the ESA12

spectrometer and the Mainz spectrometer. A continuous run of more than 4 months was performed as well. The results are extraordinarily promising.

- a $^{241}\text{Am}/\text{Co}$ photoelectron source: Inspired by [21], a $^{241}\text{Am}/\text{Co}$ photoelectron source has been prepared: γ radiation from ^{241}Am hits a thin cobalt foil resulting in monoenergetic electrons with energy of about 60 eV higher than the endpoint of the tritium beta spectrum. Photoelectrons ejected by $26\,344.6 \pm 0.2$ eV [22] γ -ray photons of ^{241}Am from the atomic K-shell of metallic cobalt with binding energy $E_{b,\text{F}}$ of $7\,708.78 \pm 0.02$ eV [23] have a kinetic energy E_{kin} close to the endpoint of the tritium β -spectrum, in particular,

$$E_{\text{kin}} = E_{\gamma} - E_{b,\text{F}} - E_{e,\text{rec}} - \varphi_{\text{spectr}} \quad , \quad (3.2)$$

where E_{γ} is the γ -ray energy, $E_{b,\text{F}}$ is the binding energy of K-shell electrons related to the Fermi level, $E_{e,\text{rec}} < 0.2\text{ eV}^1$ is the energy of the recoil atom after photoelectron emission, and φ_{spectr} is the work function of a retarding electrode of the monitor spectrometer. Indeed, such a $^{241}\text{Am}/\text{Co}$ photoelectron source would be suitable for our purpose:

- the energy of monitoring photo-electrons, 18 636 eV differs from the tritium endpoint only by about 60 eV and the calibration line would be above the β -spectrum. So the $^{241}\text{Am}/\text{Co}$ electrons have to be slowed down by appropriate positive voltage applied to the $^{241}\text{Am}/\text{Co}$ source. As a direct consequence, the positive voltage will accelerate positive ions towards the spectrometer. This could in principle increase background, but the voltage is low, and an extraordinary low background is of no concern here.
- the natural width of exciting γ -rays, its Doppler broadening at 300 K and recoil energy are less than 0.02 eV, i.e. completely negligible for our purpose
- the natural width of atomic K-shell in cobalt is 1.3 eV
- the ^{241}Am half life of 432 y is practical for long term monitoring, but also limiting possible number of 26 keV gammas due to selfabsorption if ^{241}Am .
- a $^{241}\text{Am}/\text{Co}$ source may suffer by physical-chemical changes of the binding energy. Differences of the binding energies of the Co metal component and possible Co oxides are in the range of 1.9–2.1 eV. Photo-electrons corresponding to the metal Co component originate with higher energy than the ones corresponding to Co oxide states. The differences are both well described and observable in the monitor spectrometer. Moreover, the effect may be suppressed by ion etching.

¹ for a free atom, in solids certainly much less

- a high-voltage photo-electron source (an electron gun). Photo-electrons created by ultraviolet light and accelerated by a high voltage will be used to study the tracking properties of the KATRIN beam line, and the response function of both the main and monitor spectrometer. Line width and line stability of the source are not competitive, but the source is small, can be moved across the beam line, and can be tilted easily.

3.3 Optimal distribution of measurement time and points

This section is plugged in to completely fix up the experiment setup and to ensure us, that we exactly know what has to be calibrated and monitored. That is why it is beta spectrum to be optimized in this section. A later application on monitoring lines is straightforward. So, for a particular experiment setup there are three free parameters to fix:

- distribution of the measurement time
- distribution of measurement points
- statistics used to analyze the experimental data (covered in the dedicated sections)

3.3.1 Distribution of the measurement time

Optimizing the setup of our experiment, we need to distribute the measurement time into individual spectral points, i.e., to set the measurement time for each measurement point. This should be done with respect to the physical quantity of interest, in particular, we would like to minimize the statistical deviation of the selected fit parameter. The point is, we can not set all the measurement points in parallel (numerically not possible). Instead, we can fix the measurement time in points one by one, approaching the optimal time distribution in an iterative way.

To demonstrate the method, an application on the tritium beta spectrum, and the KATRIN setup is shown. Since the optimal distribution of the measurement time is heavily dependent on the setup and spectra parameters, the tritium beta spectrum was preferred to a monitoring line, because both the experiment setup and the tritium source properties are known and fixed. When the properties of the electron sources to monitor the energy scale are known, and parameters of the monitor spectrometer such as resolution and magnetic flux are decided, then the method can be easily applied. At the moment, neither feasibility tests of the electron standards are finished, nor the monitor spectrometer setup is decided.

A full demonstration of the following method is given appendix A, because it is helpful in understanding how the MAC-E-Filter operates. The method itself runs as follows:

Let E_i be a fixed distribution of measurement points, and τ_{tot} the total measurement time. Further, let T_i be the initial time distribution chosen randomly,

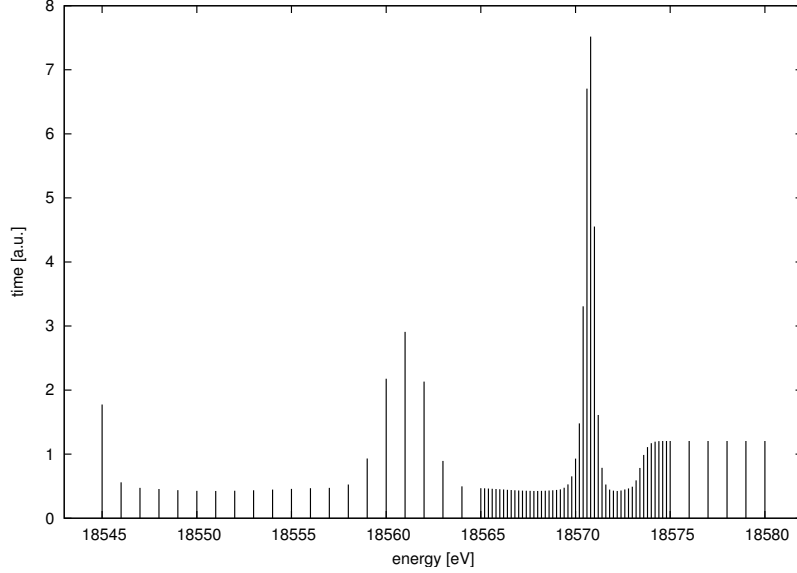


Figure 3.2 An optimal time distribution minimizing the deviation of the neutrino mass fitting four parameters: amplitude, background, the tritium endpoint, and the neutrino mass.

resulting in the initial standard deviation of the neutrino mass $\sigma_{\text{init}} = \sigma(T_i)$ (the parameter of interest). Now, we minimize the neutrino mass deviation varying the time T_1 in the first point only, keeping the total measurement time equal to τ_{tot} , i.e., scaling the measurement times in the remaining points by the same factor. As the result we obtain the time distribution t_i^1 and the corresponding neutrino mass deviation σ^1 . Then we do the same for all the other measurement points. So, we get n time distributions t_i^k , $k = 1 \dots n$ and sigmas σ^k .

The final time distribution T_i' is then given by a weighted sum

$$T_i' = \frac{1}{n} \sum_{k=1}^n \omega_k t_i^k \quad , \quad (3.3)$$

where ω_k are the weight factors. Further, we offer the following method to estimate the weight factors by extrapolating the partial time distributions t_i^k according the partial neutrino mass deviations:

$$\omega_k = \left(\frac{\sigma_{\text{init}} - \sigma^k}{\frac{1}{n} \sum \sigma^k} \right)^s \quad , \quad (3.4)$$

where s is chosen to minimize $\sigma(T'_i)$. Finally we replace the initial time distribution T_i by T'_i and start a new iteration. Practically, we implement the method on grid. This choice of the weight factors speeds the iterative procedure significantly. However, it decreases the numerical stability as well. If the numerical stability is favored, then setting all the ω_k equally to one is a good choice.

The result is shown in fig. 3.2. The neutrino mass deviation was improved by factor 0.85 compared to the uniform time distribution. Keeping the uniform time distribution, the same improvement could be achieved by the total measurement time prolongation by factor 1.9.

3.3.2 Distribution of measurement points

As well as there is the freedom to set the time distribution, there is a freedom to choose a distribution of measurement points. The choice is partially complementary to setting the time distribution. Anyway, a distribution of measurement points (set of bins) faces two problems:

- *numerical*: Nature puts into the bin an integral over the bin width from the spectrum measured that is in addition randomized by the Poisson distribution. During the data evaluation this integral is approximated simply by the theoretical spectrum value taken usually at the bin margin or the bin center.
- *practical and systematical*: e.g., bins are preferably chosen equidistant, however they are not realized exactly as equidistant, and/or sharp values of bin margins are blurred in the particular experiment. Even more, number of bins and particular count rates in the bins may influence fit results (parameter values and their deviations).

3.4 Statistics used to analyze Am/Co data

Fixing the time and point distributions, we have still freedom to choose statistics to evaluate our data. The most usual one—the least squares method—is optimized for normally distributed experimental data depending linearly on the fit parameters, answering the question, what the most probable parameter values are. Even more, the data information contained in an experimental data set is split between all the parameters.

However, in the case of monitor spectra we are interested in the stability of the line, e.i. whether the line position is within the energy interval chosen. We are not interested in the remaining fit parameters. Even more, we are not interested in the absolute value of the line position. Just the fact whether it lies in the chosen energy interval matters.

We are looking for some dedicated and focused statistical methods directly answering the questions raised. We examined performance of some standard test with respect to stability of an energy scale. We compared an differential spectrometer to an integrating MAC-E-Filter. The results are summed up in the next section. Finally, we would like to offer a common strategy leading to an optimized statistics fitting the task of monitoring an energy scale of the KATRIN experiment.

In this section we focus on an Am/Co photoelectron line and its sensitivity to energy scale imperfection. We focus on an energy scale bias as introduced in [17]. Finally, we would like to emphasize that we are interested in monitoring of the KATRIN energy scale only, in particular, in testing partial spectra against a calibration one. We omit compatibility tests [24]—a comparison of partial spectra, that represent another sensitive tool for testing the stability of the measurement conditions.

3.4.1 Hypothesis testing

Phenomenology

This paragraph introduces terminology we are going to use in the following text. First, *the null hypothesis* H_0 represents the state of no effect—the quantity, we are interested in, is kept unchanged, or within a preassigned region. The other possibility is described by *the alternative hypothesis* H_1 . When a hypothesis is fully specified by parameter values, it is called *a simple hypothesis*. A hypothesis is called *a composite hypothesis* if any parameter is kept unspecified. Let the null hypothesis be true, and Z be a subset of the range of possible values W of a test statistics Y . Let the probability that Y belongs to Z be preassigned to any

numerical value α . Then, the region Z is called *the critical region*. Further, the region $W - Z$ is called *the acceptance region* for H_0 . These regions are separated by *the critical value*. The preassigned probability α is called *the significance*, and determines *the significance level* at 100α %. As well, it corresponds to a *Type I error*. There is another possible mistake we can make, in particular, we don't reject the null hypothesis H_0 if the alternative hypothesis H_1 is true. This we call a *Type II error*. The probability of its occurrence we denote β . Finally, the probability $1 - \beta$ is called *the power of the test*.

Am/Co line

A number of Am/Co photoelectrons detected at the energy eT is a random variable $S_{\text{rand}}(T | A, B, E_0, w)$ with the Poisson probability density function (p.d.f.) with a mean value $S(T | A, B, E_0, w)$

$$S(T | A, B, E_0, w) = A \frac{w}{2\pi} \cdot \frac{1}{(w/2)^2 + (E - E_0)^2} \otimes R(E, T) + B \quad , \quad (3.5)$$

where A is an amplitude, mainly given by the specific activity of an Am source, B denotes background, E_0 stands for the line position, w is the line width, T is the voltage applied to spectrometer electrodes, and R represents a spectrometer transmission function. We neglect the width of the Am gamma transition, which is much smaller than w , and can be neglected. The line position E_0 is what we are interested in all the following hypotheses testing.

In particular, our null hypothesis H_0 tested is $E'_0 = E_0$, where E'_0 is the line position of the partial spectrum we examine, and E_0 is the line position of the calibration line. The null hypothesis H_0 is tested against the alternative hypothesis $H_1: E'_0 \in (-\infty, E_0 - \delta E) \cup (E_0 + \delta E, \infty)$. It means we accept the line position in the region $(E_0 - \delta E, E_0 + \delta E)$, where δE is a predefined value.

3.4.1.1 χ^2 test of goodness-of-fit

This is the very basic test we applied. The statistics of the null hypothesis is chosen to be the χ^2 p.d.f. (The normality requested by χ^2 is silently assumed. In general, it should be checked.) The statistics of the alternative hypothesis is the non-central χ^2 p.d.f. with non-centrality parameter λ

$$\lambda = \sum_i \frac{(S_{\text{rand}}(T_i | A, B, E'_0, w) - S(T_i | A, B, E_0, w))^2}{S_{\text{rand}}(T_i | A, B, E'_0, w) + S(T_i | A, B, E_0, w)} \quad , \quad (3.6)$$

where eT_i are the bin energies. Our alternative hypothesis is a composite one, hence the E'_0 tested is the one maximizing a Type II error—practically, we test all the simple alternative hypotheses included in the composite one, and we look for the β probability maximizer. In this case, there are two such maximizers: $E_0 - \delta E$, and $E_0 + \delta E$.

3.4.1.2 Mean values test

The null hypothesis statistics is chosen to be the p.d.f of E_0 —a normal distribution with the mean value equal to E_0 . Deviation of the normally distributed E_0 is found by pseudo-spectra evaluation (least squares method plus error ellipses method [25]). The β probability maximizers are again $E_0 - \delta E$ and $E_0 + \delta E$, hence the statistics of the alternative hypothesis is the normal distribution with the mean value of e.g. $E_0 + \delta E$ (both p.d.f.'s are symmetric), and with the same deviation as the null hypothesis statistics—a mean value and deviation of a normal distribution are mutually independent variables.

3.4.1.3 Sign test

Again, both the hypotheses tested are the same as in the first case. The statistics chosen is the number of observations bigger or less than some value, in particular, it is the number of positive signs in the following expression

$$\begin{cases} S(T_i | A, B, E_0, w) - S_{\text{rand}}(T_i | A, B, E'_0, w) & \text{for } eT_i \leq E_0 \\ S_{\text{rand}}(T_i | A, B, E'_0, w) - S(T_i | A, B, E_0, w) & \text{for } eT_i > E_0 \end{cases}, \quad (3.7)$$

in the case of a differential spectrometer (see below), and

$$S_{\text{rand}}(T_i | A, B, E'_0, w) - S(T_i | A, B, E_0, w) \quad \text{for all } T_i, \quad (3.8)$$

in the case of an integrating spectrometer. This implies a binomial p.d.f. of the null hypothesis statistics, i.e., that one where E'_0 is replaced by E_0 in (3.7), (3.8), respectively. The statistics of the alternative hypothesis is derived by a numerical simulation (E_0 replaced by the β probability maximizers, i.e., $E_0 \pm \delta E$).

3.4.1.4 Test of normal distribution of residuals

The statistics to test is a sum of residuals, i.e.,

$$\begin{aligned} & \sum_i^j \frac{S(T_i | A, B, E_0, w) - S_{\text{rand}}(T_i | A, B, E'_0, w)}{\sqrt{S_{\text{rand}}(T_i | A, B, E'_0, w)}} + \\ & + \sum_{i=j+1}^n \frac{S_{\text{rand}}(T_i | A, B, E'_0, w) - S(T_i | A, B, E_0, w)}{\sqrt{S_{\text{rand}}(T_i | A, B, E'_0, w)}}, \end{aligned} \quad (3.9)$$

in the case of a differential spectrometer, where $j = \max(i | eT_i \leq E_0)$, n is a number of bins in a measured spectrum, and

$$\sum_i \frac{S_{\text{rand}}(T_i | A, B, E'_0, w) - S(T_i | A, B, E_0, w)}{\sqrt{S_{\text{rand}}(T_i | A, B, E'_0, w)}}, \quad (3.10)$$

in the case of an integrating spectrometer. Then, the p.d.f. of the null hypothesis is the normal p.d.f. with a vanishing mean value, and with the variance equal to

the number of bins. As for the p.d.f. of the alternative hypothesis statistics, it is a random variable distributed in the normal way with the mean value

$$\begin{aligned} & \sum_i^j \frac{S(T_i | A, B, E_0, w) - S(T_i | A, B, E_0 \pm \delta E, w)}{\sqrt{S(T_i | A, B, E_0 \pm \delta E, w)}} + \\ & + \sum_{i=j+1}^n \frac{S(T_i | A, B, E_0 \pm \delta E, w) - S(T_i | A, B, E_0, w)}{\sqrt{S(T_i | A, B, E_0 \pm \delta E, w)}} \end{aligned} \quad (3.11)$$

in the case of a differential spectrometer, and

$$\sum_i \frac{S(T_i | A, B, E_0 \pm \delta E, w) - S(T_i | A, B, E_0, w)}{\sqrt{S(T_i | A, B, E_0 \pm \delta E, w)}} \quad (3.12)$$

in the case of an integrating spectrometer. The variance is equal to number of bins in both cases.

3.4.1.5 Kolmogorov-Smirnov test of residuals

Finally, we have tried the Kolmogorov-Smirnov test of residuals. The procedure is following: first, calculate residuals, in particular, the expressions

$$\Xi(T_i | A, B, E_0, w) = \begin{cases} \frac{S(T_i | A, B, E_0, w) - S_{\text{rand}}(T_i | A, B, E'_0, w)}{\sqrt{S_{\text{rand}}(T_i | A, B, E'_0, w)}} & \text{for } eT_i \leq E_0 \\ \frac{S_{\text{rand}}(T_i | A, B, E'_0, w) - S(T_i | A, B, E_0, w)}{\sqrt{S_{\text{rand}}(T_i | A, B, E'_0, w)}} & \text{for } eT_i > E_0, \end{cases} \quad (3.13)$$

in the case of a differential spectrometer, and

$$\Xi(T_i | A, B, E_0, w) = \frac{S_{\text{rand}}(T_i | A, B, E'_0, w) - S(T_i | A, B, E_0, w)}{\sqrt{S(T_i | A, B, E'_0, w)}} \quad (3.14)$$

in the case of an integrating spectrometer. Then, sort them, i.e. let τ be a one-to-one mapping from $\{1, \dots, n\}$ to $\{1, \dots, n\}$ fulfilling

$$\forall i, j \in \{1, \dots, n\}, j > \tau(i); \Xi(T_{\tau(i)} | A, B, E_0, w) \leq \Xi(T_j | A, B, E_0, w) \quad (3.15)$$

and create the cumulative distribution function (c.d.f.) of the sample $C_n(x)$ (a mapping from real numbers to $\langle 0; 1 \rangle$)

$$C_n(x) = \begin{cases} 0 & \text{for } x < \Xi(T_{\tau(1)} | A, B, E_0, w) \\ \frac{i}{n} & \text{for } \Xi(T_{\tau(i)} | A, B, E_0, w) \leq x < \Xi(T_{\tau(i)+1} | A, B, E_0, w) \\ 1 & \text{for } x \geq \Xi(T_{\tau(n)} | A, B, E_0, w) \end{cases} \quad (3.16)$$

where n , again, denotes the number of bins of a spectrum. Finally, compare C_n to an expected distribution F_0 , i.e., the normal c.d.f. with a vanishing mean value and the variance equal to n . Then, the statistics value D_n is

$$D_n = \max |C_n(x) - F_0(x)| \quad . \quad (3.17)$$

The c.d.f.'s of both the null hypothesis statistics— E'_0 replaced by E_0 in the former equations—and the statistics of the alternative hypothesis — E'_0 replaced by $E_0 \pm \delta E$ —are simulated numerically.

3.4.1.6 Preassigned values

- $A = 20$ Hz. About 60 Hz is expected in Mainz if a 1 GBq Am source is assumed. This is a very conservative assumption.
- $B = 2$ Hz. Just a guess.
- $E_0 = 18\,636$ eV. This value, however, has no effect on results of the tests.
- $w = 1.3$ eV.
- $eT \in \langle E_0 - 2.0, E_0 + 2.0 \rangle$ eV, with a step of 0.1 eV, in the case of a differential spectrometer, and $eT \in \langle E_0 - 2.5, E_0 + 1.0 \rangle$ eV, with a step of 0.1 eV, in the case of an integrating spectrometer.
- $\alpha = 1 \times 10^{-2}$. A requested Type I error.
- $\beta = 1 \times 10^{-3}$. A requested Type II error.

3.4.1.7 Remarks

The approach described here assumes that we are not going to correct the energy scale according to monitoring lines i.e., to shift the energy scale to keep the Am/Co line at the same position. This is also possible, but it would introduce a new systematic—even in the ideal case, we would smear our tritium spectra.

In principle, sensitivity of the tests can be improved by introducing a mask vector, i.e., by rejecting some bins from some tests. We have used this method in some cases. In particular, in the case of a differential spectrometer with resolution of 1 eV we masked out channels 1–6, 20–22 and 37–41 in the case of a sign test, channels 1–3, 19–23, 40–41 in the case of a test of normal distribution of residuals and a Kolmogorov-Smirnov test. As for resolution of 2 eV, we masked out channels 1–2, 17–25 and 40–41 in the case of a sign test, and channels 18–25 in the cases of a test of normal distribution of residuals and a Kolmogorov-Smirnov test. Regarding resolution of 5 eV, we masked out channels 18–25 in the case of a test of normal distribution of residuals. As for an integrating spectrometer, in the case

of resolution of 1 eV, we masked out channels 1–7, 36 in the case of a sign test, and channels 1–11 in the case of a test of normal distribution of residuals and a Kolmogorov-Smirnov test. Regarding resolution of 2 eV, we masked out channels 32–36 in the case of a sign test, and channels 1–4 in the case of a test of normal distribution of residuals and a Kolmogorov-Smirnov test. In the case of resolution of 5 eV we masked out channels 34–36 in the case of a test of normal distribution of residuals.

Some of the tests require e.g. normality of input data, and/or some other assumptions. We silently assume all of these fulfilled. Anyway, we are not restricted by these assumptions, because we can provide precise p.d.f. by numerical simulations.

3.4.2 Neutrino mass systematics caused by an energy scale bias

An energy scale bias is one of the major components to the overall systematics of the KATRIN experiment. So, in this section, we discuss a contribution of an energy scale bias to neutrino mass systematics. We focus on a step variation of the bias, in particular.

The results are shown in tab. 3.3. Pseudo-experimental spectra were created assuming a correct energy scale for the first half of the measurement time and a biased energy scale for the second one. Then, these spectra were evaluated fitting the spectra amplitude, background, the endpoint energy, and the neutrino mass. Following parameter values were chosen: a standard KATRIN setup with a optimized energy scale, a bias of 0.1 V, total measurement time of a year, the initial endpoint (i.e., that used to create the spectrum) value of 18 575.0 eV, background equal to 10 mHz. m_ν is the initial neutrino mass, Δm_ν is a difference between the fitted mass and the initial one, E_0 is the fitted endpoint energy, σ_m^+ is the fitted mass deviation, and $\sigma_{m^2}^+$ is the deviation of the fitted neutrino mass squared. The σ_m^+ values were derived by error ellipses method. The $\sigma_{m^2}^+$ value estimations are based on the σ_m^+ value, and their theoretical dependence on σ_m^+ . Further, we neglect the contribution of a $\sigma_{m^2}^+$ value change to neutrino mass systematics. A study of these contributions will be done later.

On the contrary, the requested sensitivity determines the maximum acceptable bias of the energy scale. Therefore, we examine what limits of an energy scale bias are, with respects to some preassigned values of contributions to the neutrino mass squared systematics. We restrict us to some more probable values of the neutrino mass. The results are shown in tab. 3.4.

m_ν [eV]	Δm_ν [eV]	$E_0 - 18575$ [eV]	σ_m^+ [eV]	$\sigma_{m^2}^+$ [eV ²]
0.0	-0.071 820	0.049 990	0.226 648	0.029 149
0.1	-0.029 330	0.049 999	0.113 685	0.028 993
0.2	-0.013 012	0.049 997	0.066 065	0.029 071
0.3	-0.008 594	0.049 992	0.046 435	0.029 219
0.4	-0.006 487	0.049 986	0.035 750	0.029 414
0.5	-0.005 265	0.049 978	0.029 133	0.029 675
0.6	-0.004 493	0.049 966	0.024 699	0.030 026
0.7	-0.003 983	0.049 952	0.021 609	0.030 547
0.8	-0.003 597	0.049 936	0.019 259	0.031 047
0.9	-0.003 323	0.049 917	0.017 469	0.031 634
1.0	-0.003 136	0.049 893	0.016 111	0.032 380
1.5	-0.002 915	0.049 697	0.012 983	0.039 042
2.0	-0.003 001	0.049 465	0.013 251	0.053 100

Table 3.3 A contribution of an energy scale bias to neutrino mass systematics.

m_ν [eV]	allowed contribution to m_ν^2 systematics [eV ²]				
	0.0100	0.0075	0.0050	0.0025	0.0010
0.0	138	120	98	69	44
0.1	141	122	99	70	44
0.2	140	122	99	70	44
0.3	140	121	99	70	44
0.4	139	120	98	69	44
0.5	137	119	97	69	44

Table 3.4 Energy scale biases (in mV) to keep systematics of the neutrino mass squared below some preassigned values, with respect to various initial values of the neutrino mass. For details on spectra parameters see text. Note, that we deal true systematic effects, hence the results are independent of the total measurement time.

3.4.3 Differential spectrometer

In the previous section, we have answered the question what an acceptable energy bias is, in order to keep its contribution to neutrino mass systematics below some preassigned values. Now, we would like to show what the total measurement time of an Am/Co line is to recognize such the bias, using the statistical tests described in the first section. An Am/Co line we are interested in, includes two components—a metallic one, and an oxide one. Further, we neglect the oxide component, however, the code, we use to evaluate spectra and tests, is capable to deal both components.

We split our effort into two parts, in particular, a differential spectrometer, and an integrating spectrometer. A differential spectrometer comes first. The response function $R(E, T)$ is, in this particular case,

$$R(E - eT) = \frac{1}{\sigma_d \sqrt{2\pi}} \exp \left[-\frac{(E - eT)^2}{2\sigma_d^2} \right] , \quad \sigma_d = \frac{w_d}{2\sqrt{2 \ln(2)}} , \quad (3.18)$$

where w_d is the spectrometer resolution. The dependence of the deviation of the Am/Co line position σ_{E_0} on the spectrometer resolution w_d is shown in tab. 3.5.

w_d [eV]	σ_{E_0} [meV]
5.0	102.5
4.0	66.2
3.0	41.2
2.0	25.3
1.0	16.3
0.5	13.4

Table 3.5 The dependence of the deviation of the Am/Co line position σ_{E_0} on the spectrometer resolution w_d . A total measurement time of 30 min is assumed, and the fitted parameters are A , B , E_0 , and w .

We picked up some resolutions and energy scale biases, and found the total measurement times needed to observe the biases using the statistical tests described before. The results are summarized in tab. 3.6 for a spectrometer resolution $w_d = 1.0$ eV, tab. 3.7 for $w_d = 2.0$ eV, and tab. 3.8 for $w_d = 5.0$ eV. In the following tables, χ^2 denotes a χ^2 test of goodness-of-fit (section 3.4.1.1), E_0 stands for a mean values test (section 3.4.1.2), and \pm is a sign test (section 3.4.1.3). Further, "residua" abbreviates a test of residua normal distribution (section 3.4.1.4), and "K-S" is a Kolmogorov-Smirnov test (section 3.4.1.5).

ΔU [mV]	χ^2	E_0	\pm	residua	K-S
44	306	121	235	134	223
69	125	50	95	55	91
98	62	25	48	27	45
120	42	17	32	18	30
138	32	13	24	14	23

Table 3.6 A total measurement time (in minutes) needed to distinguish some energy scale biases. A spectrometer resolution $w_d = 1.0$ eV was assumed.

ΔU [mV]	χ^2	E_0	\pm	residua	K-S
44	738	292	565	306	480
69	300	119	235	125	195
98	149	59	115	62	97
120	100	40	78	42	65
138	76	30	59	32	49

Table 3.7 A total measurement time (in minutes) needed to distinguish some energy scale biases. A spectrometer resolution $w_d = 2.0$ eV was assumed.

ΔU [mV]	χ^2	E_0	residua
44	11743	4649	5150
69	4775	1890	2095
98	2368	937	1039
120	1579	625	693
138	1194	473	524

Table 3.8 A total measurement time (in minutes) needed to distinguish some energy scale biases. A spectrometer resolution $w_d = 5.0$ eV was assumed. Here, we restricted ourselves to the best statistical tests only.

3.4.4 Integrating spectrometer

This section is mainly motivated by Am/Co feasibility tests in Mainz, and future calibration and monitoring measurements for the KATRIN experiment. The response function $R(E, T)$ is, in this particular case,

$$R(E, T) = \begin{cases} 0 & E - eT < 0 \\ \frac{1 - \sqrt{1 - \frac{E - eT}{E} \cdot \frac{B_S}{B_A}}}{1 - \sqrt{1 - \frac{\Delta E}{E} \cdot \frac{B_S}{B_A}}} & 0 \leq E - eT < \Delta E \\ 1 & \Delta E \leq E - eT \end{cases} \quad (3.19)$$

with B_A and B_S being a magnetic field at the analyzing area, and within the source, respectively. ΔE is a spectrometer resolution

$$\Delta E = \frac{B_A}{B_{\max}} \cdot E \quad , \quad (3.20)$$

where B_{\max} is the magnetic field at an entry of the spectrometer. We are not interested in particular values of the magnetic fields, because only the spectrometer resolution matters. As well, we assume no inelastic scattering of electrons in the source. The dependence of deviation of the Am/Co line position σ_{E_0} on the spectrometer resolution ΔE is shown in tab. 3.9.

ΔE @ 20 keV [eV]	σ_{E_0} [meV]
5.0	133.6
4.0	117.1
3.0	95.3
2.0	51.2
1.0	30.8
0.5	28.8

Table 3.9 The dependence of deviation of the Am/Co line position σ_{E_0} on the spectrometer resolution ΔE at 20 keV. The total measurement time of 30 min is assumed. The fitted parameters are A , B , E_0 , and w .

Similarly as in the case of a differential spectrometer, we picked up some resolutions and energy scale biases, and found the total measurement times needed to observe the biases using the statistical tests described before. The results are summarized in tab. 3.10 for a spectrometer resolution $\Delta E = 1.0$ eV, tab. 3.11 for $\Delta E = 2.0$ eV, and tab. 3.12 for $\Delta E = 5.0$ eV. The abbreviations used are the same as in section 3.4.1. So, χ^2 denotes a χ^2 test of goodness-of-fit (sec. 3.4.1.1), E_0

stands for a mean values test (sec. 3.4.1.2), and \pm is a sign test (sec. 3.4.1.3). Further, "residua" abbreviates a test of residua normal distribution (sec. 3.4.1.4), and "K-S" is a Kolmogorov-Smirnov test (sec. 3.4.1.5).

ΔU [mV]	χ^2	E_0	\pm	residua	K-S
44	266	436	364	123	206
69	109	178	148	51	84
98	54	88	74	25	42
120	36	59	49	17	28
138	28	45	37	13	21

Table 3.10 A total measurement time (in minutes) needed to distinguish some energy scale biases. A spectrometer resolution $\Delta E = 1.0$ eV at 20 keV was assumed.

ΔU [mV]	χ^2	E_0	\pm	residua	K-S
44	303	1374	412	138	272
69	125	559	168	56	111
98	62	277	84	28	55
120	41	185	56	19	37
138	31	140	42	15	28

Table 3.11 A total measurement time (in minutes) needed to distinguish some energy scale biases. A spectrometer resolution $\Delta E = 2.0$ eV at 20 keV was assumed.

ΔU [mV]	χ^2	E_0	residua
44	669	20025	289
69	272	8145	118
98	139	4040	59
120	90	2693	39
138	68	2036	30

Table 3.12 A total measurement time (in minutes) needed to distinguish some energy scale biases. A spectrometer resolution $\Delta E = 5.0$ eV at 20 keV was assumed. Here, we restricted ourselves to the best statistical tests only.

3.4.5 Conclusion

We studied possibilities of an Am/Co monoenergetic photoelectrons to monitor a energy scale of the KATRIN experiment. First, we introduced several statistical methods to test measured Am/Co lines against a calibration one. Then, we studied the contribution of an energy scale bias to neutrino mass systematics. And finally, we investigated what a reasonable measurement time of an Am/Co line is, in order to monitor such the bias. Both a differential spectrometer and an integrating spectrometer were discussed. The results are very promising. Further improvements are possible, e.g. an optimized time distribution of measurement points. Further, we gained some experience, what behaviour of a differential and an integrating spectrometer could be in such case.

3.5 Statistics used to analyze Kr lines

We briefly applied the same hypothesis tests as in section 3.4.1 at page 34 to the Kr lines covering both the differential and integrating spectrometer. We do not aim to study all the Kr lines and spectrometer resolutions. The purpose of the following tests is to get performances of the Am/Co and Kr sources compared to each other. We focus on Kr lines induced by 32 keV transition.

3.5.1 Preassigned values

Keeping the labels introduced in eq. 3.5 section 3.4.1 at page 34, we estimate and assign the following values:

- $a = 1$ kBq. With respect to branching ratios of 0.238 (K line), 0.381 (L_3 line), and $(0.0038 + 0.0057)$ ($N_{2,3}$) we get amplitudes: $A = 39.7$ Hz for the K line, $A = 0.381$ Hz for the L_3 line, and $A = 1.6$ Hz for the $N_{2,3}$ line.
- $B = 1$ Hz. Just a guess again.
- $E_0 = 17\,824.4$ eV for the K line, $E_0 = 30\,472.4$ eV for the L_3 line, and $E_0 = 32\,136.9$ eV $E_0 = 32\,137.6$ eV for the N_2 and N_3 line, respectively. These values have no effect on results of the tests.
- $w = 2.8$ eV, $w = 1.4$ eV, and $w = 0.03$ eV for the K line, L_3 line, and $N_{2,3}$ line, respectively.
- $eT \in \langle E_0 - 2.0, E_0 + 2.0 \rangle$ eV, with a step of 0.1 eV, in the case of a differential spectrometer, and $eT \in \langle E_0 - 2.5, E_0 + 1.0 \rangle$ eV, with a step of 0.1 eV, in the case of an integrating spectrometer.
- $\alpha = 1 \times 10^{-2}$. A requested Type I error.
- $\beta = 1 \times 10^{-3}$. A requested Type II error.

ΔU [mV]	χ^2	E_0	\pm	residua	K-S
44	744	254	485	273	395
69	303	104	198	111	162
98	150	52	99	56	81
120	101	35	66	37	54
138	76	26	50	28	41

Table 3.13 A total measurement time (in minutes) needed to distinguish some energy scale biases. A spectrometer resolution $w_d = 1.0$ eV at 20 keV was assumed.

3.5.2 Differential spectrometer

A differential spectrometer is driven by resolution given in eq. 3.18 page 41. Each time we talk about a general differential spectrometer we tacitly assume the ESA12 spectrometer in Rez, which is not limiting. All the results are perfectly valid. Further we implement an artificial luminosity to be equal to luminosity of an integrating MAC-E-Filter with an accepted angle of 51° and a detector efficiency of 0.9.

We pay some attention also to L3 and N2,3 lines. Although these lines are of no use with respect to monitoring of the KATRIN experiment, they are very useful in development of sources of monoenergetic electrons. They provide valuable cross checks and methods to understand spectrometers themselves. In particular, L lines induced by 9.4 keV gammas are studied with the Rez spectrometer. The information on long term stability of these L lines, can be transformed into stability of the K-32 line, as well as stability of the electrical equipment in use, and stability of the experimental setup.

3.5.2.1 K-32 line

Because of the wide energy range of all the Kr lines, we stick to spectrometer resolutions at 20 keV. Then the same resolution corresponds to the same setup of the spectrometer. The absolute spectrometer resolution at the energy range of a particular Kr line, can be easily derived from the constant relative resolution.

The results obtained for resolution of 1 eV at 20 keV are summarized in tab. 3.13. As for resolution of 2 eV at 20 keV, the relevant total measurement times are given in tab. 3.14, and resolution of 0.5 eV at 20 keV is covered in tab. 3.15.

Regarding the mask vector introduced in sec. 3.4.1.7, we use it as well as in the Am/Co case to improve the performance of the particular statistical tests. For the K-32 line and the resolution of 1 eV at 20 keV we masked out bins 1–5, 30–33, and 57–61 in the case of a sign test, bins 29–33 in the case of a test of normal

ΔU [mV]	χ^2	E_0	\pm	residua	K-S
44	1003	343	610	360	525
69	408	140	249	147	225
98	203	70	123	73	112
120	135	47	83	49	75
138	102	35	63	36	57

Table 3.14 A total measurement time (in minutes) needed to distinguish some energy scale biases. A spectrometer resolution $w_d = 2.0$ eV at 20 keV was assumed.

ΔU [mV]	χ^2	E_0	\pm	residua	K-S
44	648	222	410	242	362
69	264	91	167	99	153
98	131	45	83	49	76
120	88	30	56	33	51
138	66	23	42	25	39

Table 3.15 A total measurement time (in minutes) needed to distinguish some energy scale biases. A spectrometer resolution $w_d = 0.5$ eV at 20 keV was assumed.

ΔU [mV]	χ^2	E_0	\pm	residua	K-S
44	147	51	115	55	84
69	57	21	47	23	35
98	29	11	24	12	17
120	19	7	16	8	12
138	15	6	12	6	9

Table 3.16 A total measurement time (in minutes) needed to distinguish some energy scale biases. A spectrometer resolution $w_d = 1.0$ eV at 20 keV was assumed.

distribution of residuals, and bins 29–34 in the case of a Kolmogorov-Smirnov test. As for the resolution of 2 eV at 20 keV we masked out bins 29–33 for the sign test, bins 28–34 in the cases of normal distribution of residuals and Kolmogorov-Smirnov tests. And finally for the resolution of 0.5 eV at 20 keV, we masked out bins 1–2, 60–61, and 30–32 in the case of a sign test, bins 30–33 for a residuals test, and bins 30–33 for the case of a Kolmogorov-Smirnov test.

ΔU [mV]	χ^2	E_0	\pm	residua	K-S
44	428	156	280	105	261
69	175	64	114	68	107
98	87	32	57	34	53
120	58	21	38	23	36
138	44	16	29	17	27

Table 3.17 A total measurement time (in minutes) needed to distinguish some energy scale biases. A spectrometer resolution $w_d = 2.0$ eV at 20 keV was assumed.

ΔU [mV]	χ^2	E_0	\pm	residua	K-S
44	83	31	59	36	56
69	34	13	26	15	23
98	17	7	13	8	12
120	12	5	9	5	8
138	9	4	7	4	6

Table 3.18 A total measurement time (in minutes) needed to distinguish some energy scale biases. A spectrometer resolution $w_d = 0.5$ eV at 20 keV was assumed.

3.5.2.2 L3-32 line

It is relative energy resolution which is given by a spectrometer setup. Then absolute energy resolution at the energy range of the L3-32 line is about factor 1.6 larger compared to absolute energy resolution at 20 keV. The simulation results relevant for resolution of 1 eV at 20 keV are shown in tab. 3.16. Regarding resolution of 2 eV at 20 keV, the measurement times are covered in tab. 3.17, and finally resolution of 0.5 eV at 20 keV is given in tab. 3.18.

The mask vectors were introduced as follows: for the resolution of 1 eV at 20 keV, we masked out bins 1–6, 25–28, and 47 in the case of a sign test, bins 24–28 in both the cases of a residuals normality test and a Kolmogorov-Smirnov test. As for the resolution of 2 eV at 20 keV, we masked out bins 22–30 for a sign test, and bins 22–31 in both the cases of a test of normal distribution of residuals and a Kolmogorov-Smirnov test. And finally, in the case of 0.5 eV at 20 keV we masked out bins 1–8, 26–27, and 44–51 in the case of a sign test, and bins 1–5, 25–27, and 47–51 in both the cases of a test of residuals normality and a Kolmogorov-Smirnov test.

ΔU [mV]	χ^2	residua
44	5775	1999
69	2351	813
98	1168	404
120	780	270
138	591	204

Table 3.19 A total measurement time (in minutes) needed to distinguish some energy scale biases. A spectrometer resolution $w_d = 1.0$ eV at 20 keV was assumed.

ΔU [mV]	χ^2	residua
44	46 194	15 629
69	18 816	6 366
98	9 337	3 166
120	6 234	2 117
138	4 717	1 605

Table 3.20 A total measurement time (in minutes) needed to distinguish some energy scale biases. A spectrometer resolution $w_d = 2.0$ eV at 20 keV was assumed.

3.5.2.3 N_{2,3}-32 line

In this case we restricted ourselves just to a χ^2 test and a test of normal distribution. We hope it is pedagogical enough, and a complete picture can be easily reconstructed with the knowledge gained for K and L₃ lines. The results obtained for resolution of 1 eV at 20 keV are shown in tab. 3.19. As for resolution of 2 eV at 20 keV, the total measurement times are given in tab. 3.20, and resolution of 0.5 eV at 20 keV is shown in tab. 3.21.

Regarding the mask vector employed for the N_{2,3} line it is as follows: bins 1–5, 37–45, and 74–75 were masked out in a test of residuals normality for the resolution of 1 eV at 20 keV. As for the resolution of 2 eV at 20 keV, we masked out bins 33–45 for a test of normal distribution of residuals, and bins 1–8, 42–45, and 70–75 in the case of the same test and resolution of 0.5 eV at 20 keV.

ΔU [mV]	χ^2	residua
44	1709	765
69	699	311
98	349	155
120	234	103
138	178	78

Table 3.21 A total measurement time (in minutes) needed to distinguish some energy scale biases. A spectrometer resolution $w_d = 0.5$ eV at 20 keV was assumed.

ΔU [mV]	χ^2	E_0	\pm	residua	K-S
44	396	1083	365	156	236
69	162	441	149	64	97
98	81	212	74	32	49
120	55	135	50	21	34
138	42	103	38	16	26

Table 3.22 A total measurement time (in minutes) needed to distinguish some energy scale biases. A spectrometer resolution $\Delta E = 1.0$ eV at 20 keV was assumed.

ΔU [mV]	χ^2	E_0	\pm	residua	K-S
44	399	1288	315	157	236
69	163	525	129	64	98
98	82	258	64	32	49
120	55	172	43	21	34
138	42	130	33	16	26

Table 3.23 A total measurement time (in minutes) needed to distinguish some energy scale biases. A spectrometer resolution $\Delta E = 2.0$ eV at 20 keV was assumed.

3.5.3 Integrating spectrometer

Resolution of an integrating spectrometer is given by eq. 3.19. This is to be plugged in eq. 3.5 to get a simulated line. Again, we tacitly assume the monitor spectrometer (the Mainz spectrometer) each time we talk about an integrating MAC-E-Filter. Further in our setup, we fixed the accepted angle of an integrating spectrometer to a value of 51° , and detector efficiency to 0.9.

3.5.3.1 K-32 line

The results obtained for resolution of 1 eV at 20 keV are summarized in tab. 3.22. As for resolution of 2 eV at 20 keV, the relevant total measurement times are given in tab. 3.23, and resolution of 0.5 eV at 20 keV is covered in tab. 3.24.

Regarding the mask vector introduced in sec. 3.4.1.7, we employ it to mask out the following bins: in the case of resolution of 1 eV at 20 keV, we mask out bins 1–10 for a sign test, bins 1–15 in the case of a test of normal distribution of residuals, and bins 1–15 in the case of a Kolmogorov-Smirnov test. As for resolution of 2 eV at 20 keV we masked out bins 1–3, and 51 in the case of a sign test, bins 1–8 in for both a test of residuals normality and a Kolmogorov-Smirnov test. And finally

ΔU [mV]	χ^2	E_0	\pm	residua	K-S
44	403	1323	350	159	247
69	165	473	142	65	102
98	83	211	71	32	52
120	56	132	47	21	36
138	43	97	35	16	26

Table 3.24 A total measurement time (in minutes) needed to distinguish some energy scale biases. A spectrometer resolution $\Delta E = 0.5$ eV at 20 keV was assumed.

ΔU [mV]	χ^2	E_0	\pm	residua	K-S
44	128	772	88	48	73
69	52	314	36	20	32
98	26	152	18	10	16
120	18	100	12	7	11
138	14	75	9	5	8

Table 3.25 A total measurement time (in minutes) needed to distinguish some energy scale biases. A spectrometer resolution $\Delta E = 1.0$ eV at 20 keV was assumed.

for resolution of 0.5 eV at 20 keV we masked out bins 1–17, and 51 in the case of a sign test, and bins 1–19 for both tests of normal distribution of residuals and a Kolmogorov-Smirnov test.

3.5.3.2 L-3 line

We are going to cut our simulation by the last list of measurement times for the case of an integrating spectrometer with resolution of 1 eV at 20 keV. We hope, that the picture how Kr sources perform in our spectrometers is more or less complete. Even more, the line is of no use for calibration and monitoring. The line is extremely useful to understand systematics and the monitor spectrometer itself, anyway, these statistical tests do not help in the understanding in any way. The results obtained are covered in tab. 3.25. In this case, we masked out bins 1–15 in the case of a sign test, and a bin 1 for both a test of residuals normality and a Kolmogorov-Smirnov test.

3.5.4 Conclusion

By this section we aimed to compare a differential and an integrating spectrometer spectrometers with respect to their performance in monitoring stability of an energy scale. A differential spectrometer is easier to understand compared to an integrating one, most probably because of a correlation of the line position and line width in the case of an integrating spectrometer. As expected, the line position itself is a good measure on line stability in the case of a differential spectrometer, Surprisingly, this statement is not true for an integrating spectrometer. At that case, all the test perform better than the position fit, with a test of normal distribution of residuals being the leader. We also aimed to show, how the particular statistical tests scale with time, line width, and signal to background ratio.

3.6 Outlook on statistical methods

To summarize the experience with statistical tests in previous sections, they seem to be a great complementary option to the usual parameter estimation methods with even higher sensitivity to the effects of interest. Both the methods are based on the same prerequisites. These are: a question asked, an experimental spectrum measured, and a theoretical spectrum to be compared to the measured spectrum. With respect to an experimental spectrum and a fixed setup, we decide where to measure and for how long (in the case of single channel experiment, which is the case). These were discussed in the section 3.3 (in the parameter estimation framework). As for the theoretical spectrum, binning is the main issue (where the theoretical spectrum is evaluated). This is usually at the bin center, anyway, the energy distribution within the bin is known, and should be taken into account. The energy distribution is not Gaussian, due to ad/da pathologies. Another numerical blur comes from using the real devices returning always a random number. These can be easily built into the theoretical spectrum to be compared to experiment. We offer the following two methods: 1. let's ignore the binning at all, e.i., let's have the same number of bins as the measured points; 2. use arbitrary reasonable number of bins to satisfy assumptions of statistical methods used, and evaluate the theoretical spectrum as the averaged theoretical value over all the measured energies in the bin.

Regarding the former way, let us assume we measured a spectrum of N sweeps of p bins each obtaining $N \times p$ energy-count-rate pairs $\{E_i^{(j)}, n_i^{(j)}\}_{i=1..p}^{j=1..N}$. Let us take all the $N \times p$ pairs as one set and reorder it in the sense of increasing energies

$$\{(E_k, n_k); E_k < E_{k+1}\}_{k=1}^{N \times p} \quad (3.21)$$

Formally, this is one spectrum measured in very many points and it can enter directly into a minimizing procedure. We can assume, that n_k follow the Poisson distribution. (This assumption may be easily checked, and actually should be, because a measured spectrum is usually a mixture of signal and various background components.) Then we can minimize the following two functions in place of the usual chi-square one [26, 27, 28]

$$\chi_{BC}^2 = \frac{2}{N \times p} \sum_{k=1}^{N \times p} \left(Th(x; E_k) - n_k + n_k \cdot \ln \frac{n_k}{Th(x; E_k)} \right) , \quad (3.22)$$

$$\chi_P^2 = \frac{1}{N \times p} \sum_{k=1}^{N \times p} \left(2(Th(x; E_k) - n_k) + (2n_k + 1) \cdot \ln \frac{2n_k + 1}{2Th(x; E_k) + 1} \right) , \quad (3.23)$$

where $Th(x, E_k)$ are theoretical expectations for the x vector of parameters and the E_k energy. The standard deviations of fit parameters may be, as usually, estimated by “chi-square plus one” way, substituting the chi-square function by any of the previous two functions.

Focusing on the statistical tests, we propose the following concept. Let’s assume we have chosen our H_0 and H_1 hypothesis and let us find the best statistical test to reject the H_0 hypothesis. We define the best test as the statistics minimizing both the errors of the first and the second kind, e.i., the intersection of H_0 and H_1 histograms (distributions) is the measure, how the statistics good is. As the reference statistics we would utilize the standard parameter fit (which is a good statistics as well, because the fit maps an experimental spectrum to a parameter value).

As for the parameters the statistics should depend on we choose: the theoretical spectrum, the experimental spectrum, and the energy points, where the experimental spectrum has been measured. Further, we would like to restrict us to the statistics that are smooth (continuous, and derivable). This is highly practical, anyway we reject statistics such as the Kolmogorov-Smirnov one. The statistics chosen are expandable into Taylor series. And we search the optimal coefficients in the series minimizing the intersection of the H_0 and H_1 hypothesis, thus forming the best statistics for our choice of the hypothesis. We consider the following two series useful for us:

$$\begin{aligned}
S(\Sigma \text{Exp}_i, \Sigma \text{Th}_i, \Sigma \text{Eng}_i) &= c_0 + c_1 \Sigma \text{Exp}_i + c_2 \Sigma \text{Th}_i + c_3 \Sigma \text{Eng}_i + \\
&+ c_4 (\Sigma \text{Exp}_i)^2 + c_5 (\Sigma \text{Th}_i)^2 + c_6 (\Sigma \text{Eng}_i)^2 + \\
&+ c_7 (\Sigma \text{Exp}_i)(\Sigma \text{Th}_i) + c_8 (\Sigma \text{Exp}_i)(\Sigma \text{Eng}_i) + \dots \quad ,
\end{aligned} \tag{3.24}$$

$$\begin{aligned}
S(\text{Exp}, \text{Th}, \text{Eng}) &= \sum S_i(\text{Exp}_i, \text{Th}_i, \text{Eng}_i) = \\
&= c_0 + \Sigma c_{1i} \text{Exp}_i + \Sigma c_{2i} \text{Th}_i + \Sigma c_{3i} \text{Eng}_i + \\
&+ \Sigma c_{4i} (\text{Exp}_i)^2 + \Sigma c_{5i} (\text{Th}_i)^2 + \Sigma c_{6i} (\text{Eng}_i)^2 + \\
&+ \Sigma c_{7i} (\text{Exp}_i)(\text{Th}_i) + \Sigma c_{8i} (\text{Exp}_i)(\text{Eng}_i) + \dots \quad .
\end{aligned} \tag{3.25}$$

Now, we introduce *global transformations* of statistics as a tool to cut down number of terms in the Taylor series. The idea is as follows: Let g is a global transformation, e.i, a mapping of a statistics S to a statistics S' , which is invertible and smooth in both directions. Then, both the statistics S and $S' = g(S)$ are equally good, e.i. the intersections of relevant H_0 and H_1 are the same. This can be proved in math rigor. As an example of such a global transformation let us consider:

$$S' = S + \text{const} \quad , \tag{3.26}$$

which shifts the scale, and makes the c_0 constants useless in both the Taylor series above. Or, let us consider:

$$S' = \text{const} \cdot S \quad , \quad (3.27)$$

which scales the scale, and lets us fix the c_1 to an arbitrary value in the first series, and let us fixed the sum $\sum c_{1i}$ to an arbitrary value as well. We tested feasibility of the concept on the constant and linear spectra. In both cases, the optimal coefficients in both the Taylor series were found in a perfect agreement with analytical solutions, that were possible in both the cases.

Finally, we would like to stress the importance of the proper H_0 and H_1 hypothesis formulation, that are plug into the concept. The final statistics found is optimal with respect to the hypothesis. For sure, as many statistics may be find as the relevant choices of the hypothesis we have and need to answer all the question, and completely digest the experimental data.

4 Experiments

4.1 First $^{83}\text{Rb}/^{83\text{m}}\text{Kr}$ measurements at Mainz

In June, 2005, we studied a Rb/Kr source at Mainz. A brief description of the Rb/Kr source, a spectrometer setup, and results are covered in the section. A solid $^{83}\text{Rb}/^{83\text{m}}\text{Kr}$ source was produced by ^{83}Rb evaporated on an Al backing. The challenge is to capture the $^{83\text{m}}\text{Kr}$ within the thin ^{83}Rb layer sample till its decay. For a detail introduction to the $^{83}\text{Rb}/^{83\text{m}}\text{Kr}$ source see [12].

The development of $^{83}\text{Rb}/^{83\text{m}}\text{Kr}$ was at the very beginning, so we aimed to provide any evidence of zero energy-loss electrons of $^{83\text{m}}\text{Kr}$ lines. Consequently we aimed to demonstrate, that the Mainz spectrometer might be operated with energy resolution of about 1.5 eV at the 18 keV region.

4.1.1 Rb/Kr source

The $^{83}\text{Rb}/^{83\text{m}}\text{Kr}$ source of 30 kBq was prepared at NPI Rez by vacuum evaporation onto an aluminum backing of 8 mm in diameter at temperature of about 800 °C and vacuum of 3×10^{-5} mbar. ^{83}Rb was produced via (p, xn) reaction using the NPI Rez cyclotron. The target was a gaseous Kr in a natural isotope mixture. The efficiency of evaporating procedure was about 6 %. The activity of the final source was determined by gamma spectroscopy. Non-radioactive Rb solution (RbNO_3) was added to an ^{83}Rb solution to achieve the same number of Rb atoms as the source prepared by A. Kovalik, who studied the complete conversion-electron spectrum of the 9.4 keV M1 + E2 transition in ^{83}Kr [29].

Anyway, gamma measurements of 9 keV and 32 keV lines from $^{83}\text{Rb}/^{83\text{m}}\text{Kr}$ showed that only about 10 % of $^{83\text{m}}\text{Kr}$ remain in the source.

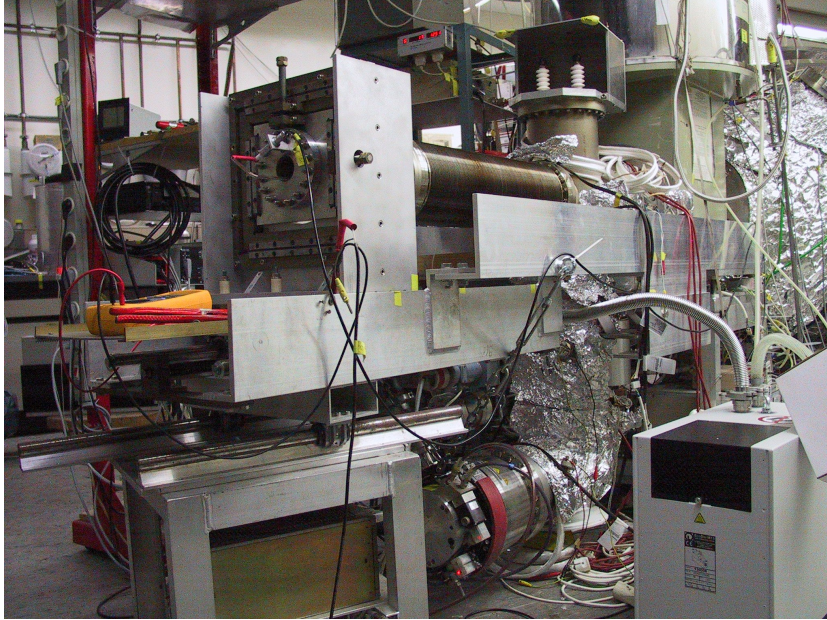


Figure 4.1 The setup of a $^{83}\text{Rb}/^{83\text{m}}\text{Kr}$ source. The source is placed just in the pinch magnet of the spectrometer and pumped down to pressure range of 10^{-9} mbar.

4.1.2 Mainz spectrometer setup

Both the pinch magnets A and B were set to currents of $I_A = I_B = 45$ A generating moderate magnetic fields of about $B_B = B_A = 5.4$ T. The detector magnet C was set to its full field of about $B_C = 1.7$ T ($I_C = 60$ A). The spectrometer tank was pumped down to pressure of 5×10^{-10} mbar (both the source valve and the detector valve opened).

The source part of the spectrometer was reassembled to place $^{83}\text{Rb}/^{83\text{m}}\text{Kr}$ (and alternatively $^{241}\text{Am}/\text{Co}$) sources directly into the spectrometer magnet B (see fig. 4.1). The electron sources were mounted at an ESA12 holder (the one used at the Rez/Prague ESA12 spectrometer), and then fixed in a former quenched condensed tritium source (see fig. 4.2). The $^{83}\text{Rb}/^{83\text{m}}\text{Kr}$ source was pumped down to pressure of 8×10^{-9} mbar. We did not bake up the $^{83}\text{Rb}/^{83\text{m}}\text{Kr}$ part of the spectrometer to avoid possible ^{83}Rb release to the spectrometer.

The detector was charged up to 40 V. During the $^{83}\text{Rb}/^{83\text{m}}\text{Kr}$ measurements we took data from the very inner segment only (sensitive area of 1 cm^2). Signal quality of the other segments was significantly lower.

First of all, the scope of our interest included the K-conversion electron line in ^{83}Kr (denoted K-32) with the energy of about 17 824 eV, and the line width of 2.8 eV. We begun the measurements with moderate resolution of 3.8 eV at 17 824 eV (air



Figure 4.2 The former holder of quenched condensed tritium modified to house a $^{83}\text{Rb}/^{83\text{m}}\text{Kr}$ source. A detail picture of the $^{83}\text{Rb}/^{83\text{m}}\text{Kr}$ source on the right.

coils current of -0 A leading to the magnetic field at the analyzing plane of 11.5 G) resulting in beam flux diameter at the analyzing plane of 43.4 cm, mapping the source area of 6.7 mm in diameter (assuming magnetic field at the source area equal to $0.9B_B$), and guaranteeing good adiabatic conditions along a magnetic field line. For our first scan of K-32 line see fig. 4.3.

Keeping the moderate conditions, and moving the source 4.5 mm down and 1.0 mm left we reached the optimal source position (with respect to signal to noise ratio) being just 1.0 mm above the inner wall of the magnet B. The spectrum we obtained is shown in fig. 4.4.

Then, we improved the resolution to 1.6 eV by setting the air coil current to -7.5 A, and the detector magnet C current to 35 A resulting in magnetic field at the analyzing plane of 4.9 G, and detector field of 1.0 T. The lower detector field is to avoid the beam to hit the spectrometer wall. The result is shown in fig. 4.5. As for the decreased background, the better resolution worsened adiabatic condition along a magnetic field line. Thus, the decreased background is a proof of the background component originating in the source area.

Finally, we optimized the source area mapped to the detector by a set of scans with I_C equal to 55, 45, 35, and 25 A, and the fixed air coil current of -7.5 A (leading to magnetic fields at the analyzing plane of 5.6, 5.3, 4.9, and 4.6 G, resulting in energy resolutions of 1.8, 1.7, 1.6, and 1.5 eV, respectively). The result is shown in

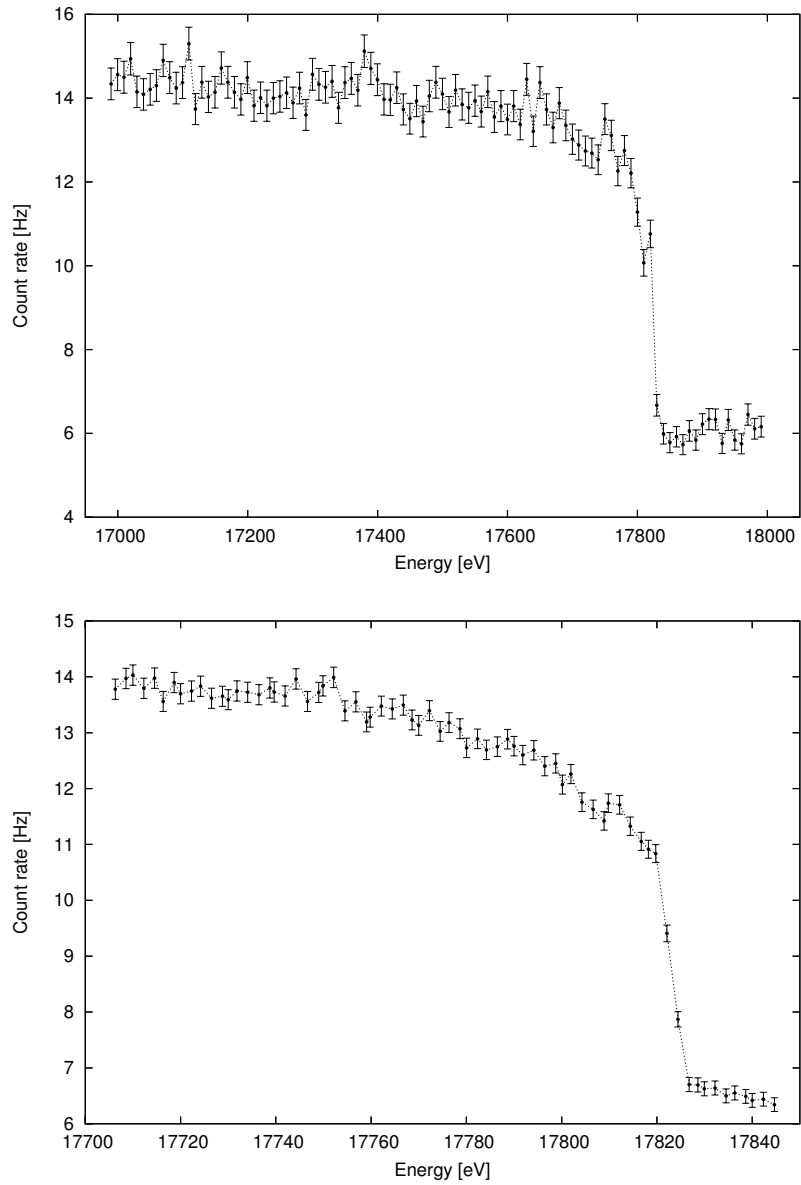


Figure 4.3 The first spectrum of K-32 line measured from the $^{83}\text{Rb}/^{83\text{m}}\text{Kr}$ solid source using the Mainz MAC-E-Filter. A wide region scan at the top, and a narrow one at the bottom.

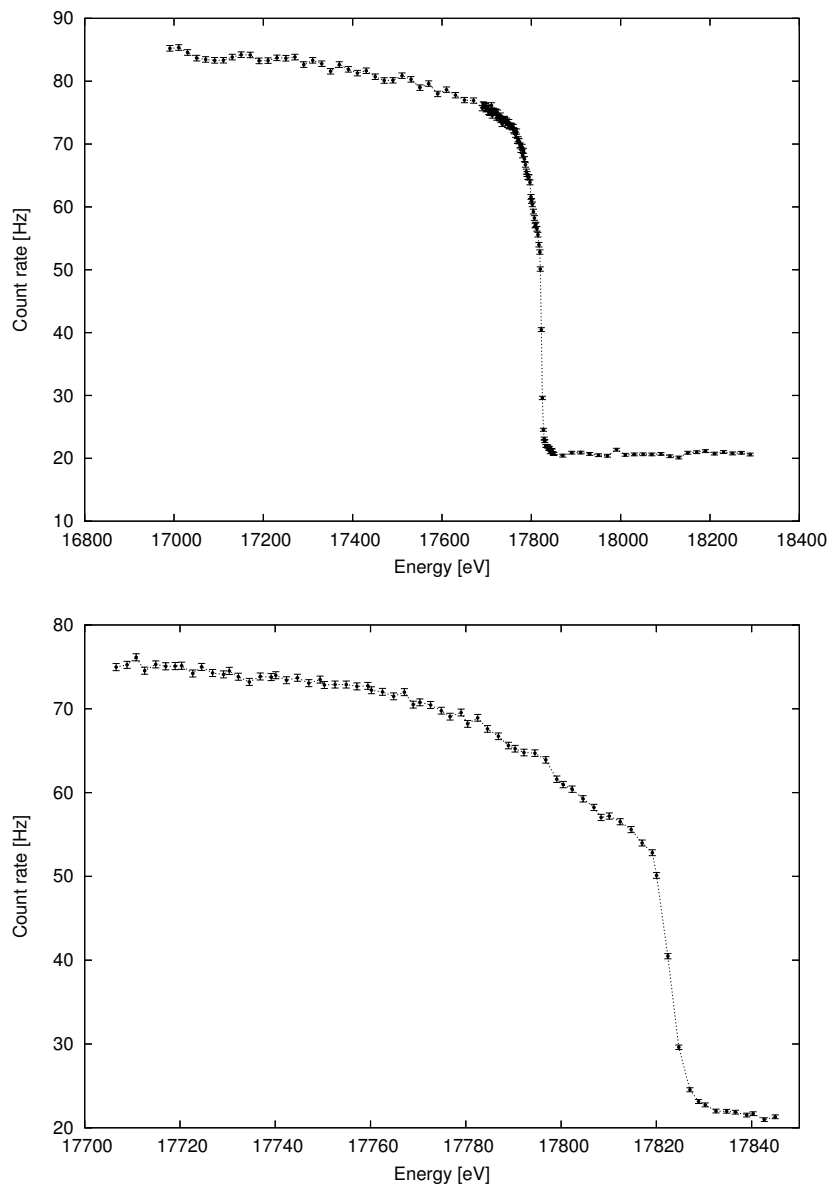


Figure 4.4 An optimized position of the $^{83}\text{Rb}/^{83\text{m}}\text{Kr}$ source in the pinch magnet of the Mainz spectrometer. A wide region scan of the K-32 line at the top, and a narrow one at the bottom.

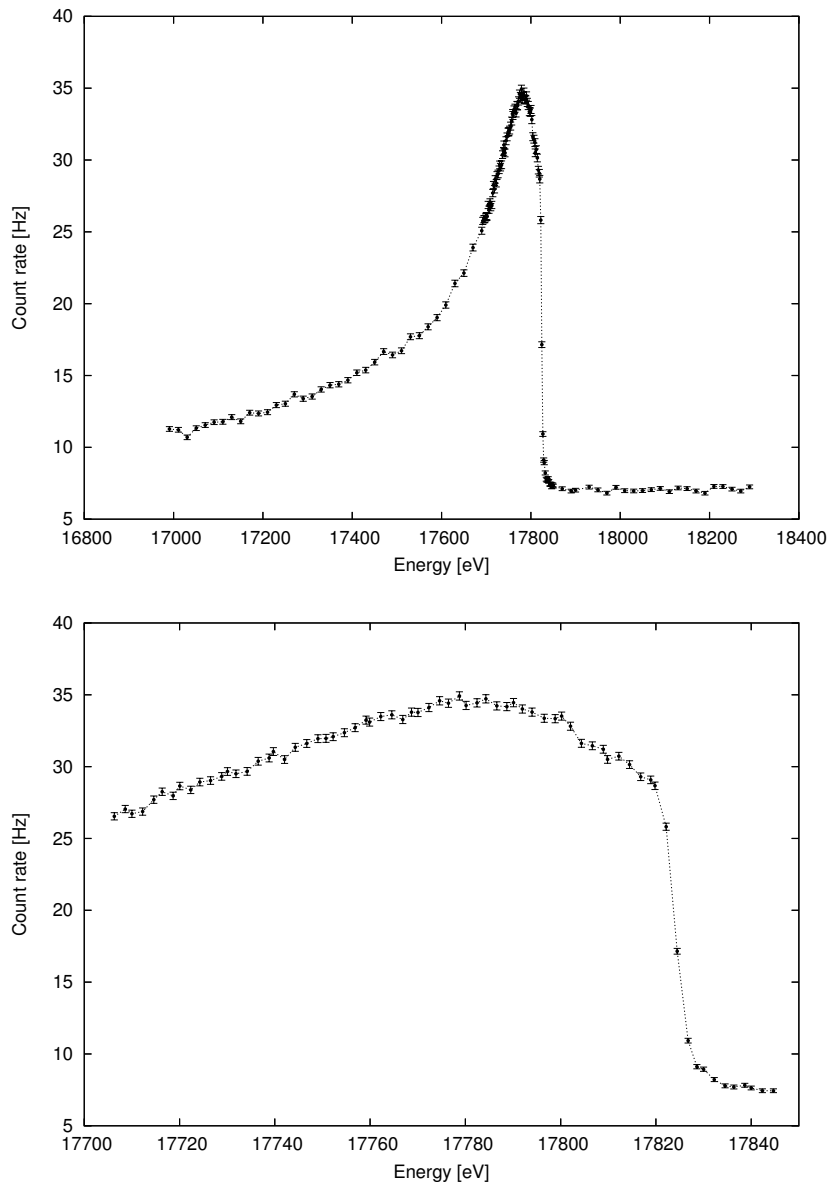


Figure 4.5 Fixing the energy resolution to 1.6 eV. A wide scan of the $^{83}\text{Rb}/^{83\text{m}}\text{Kr}$ K-32 line measured with the Mainz spectrometer at the top figure, and a zoom at the bottom one.

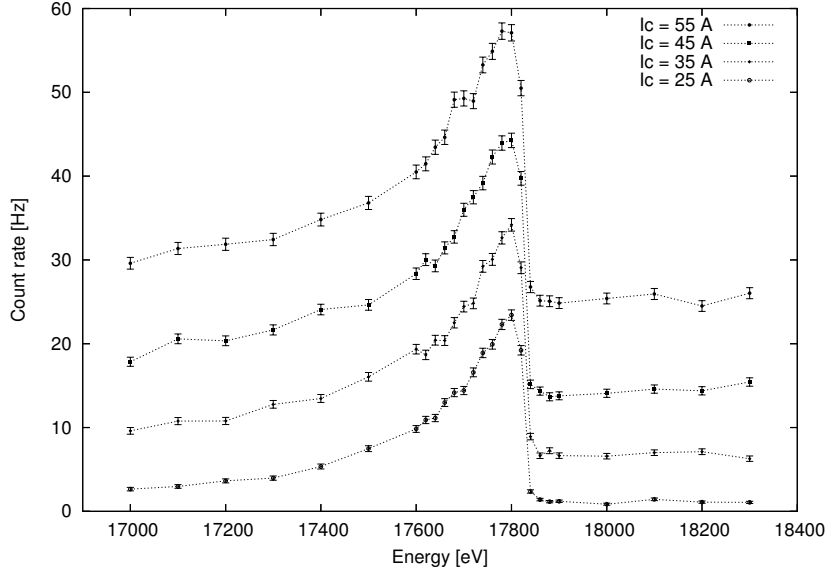


Figure 4.6 Optimizing the $^{83}\text{Rb}/^{83\text{m}}\text{Kr}$ source area seen by the detector of the Mainz spectrometer. Optimization is achieved by tuning the magnetic field at the detector. I_C is the current of the detector magnet. Scans of $^{83}\text{Rb}/^{83\text{m}}\text{Kr}$ K-32 line are shown.

fig. 4.6. The best signal to background ratio was obtained for the detector magnet C current of $I_C = 25$ A, i.e. magnetic field of 0.7 T, mapping a source area of 4.3 mm in diameter (29 % of the source).

4.1.3 Results

4.1.3.1 K-32 line

A scan of the K-32 line measured with resolution of 1.5 eV at 17 824 eV is shown in fig. 4.7. Based on the scan we estimated the $^{83\text{m}}\text{Kr}$ source activity. Assuming accepted angle of 25 % out of 4π , detector efficiency of 0.8, a relative source area of 0.29, decay ratio of 0.176, and the measured effect of 19.4 Hz the $^{83\text{m}}\text{Kr}$ activity at the $^{83}\text{Rb}/^{83\text{m}}\text{Kr}$ source is 1.9 kBq. Compared to ^{83}Rb activity of 29 kBq measured by gamma spectroscopy, we may conclude that just 7 % of $^{83\text{m}}\text{Kr}$ was being kept within the $^{83}\text{Rb}/^{83\text{m}}\text{Kr}$ source until its decay.

Fitting the data assuming theoretical spectrometer resolution of 1.5 eV, e.i. neglecting electrical inhomogeneities of the analyzing plane (about 0.5 V), and HV ripple of about 0.8 V (peak to peak), we obtain the following values: the amplitude

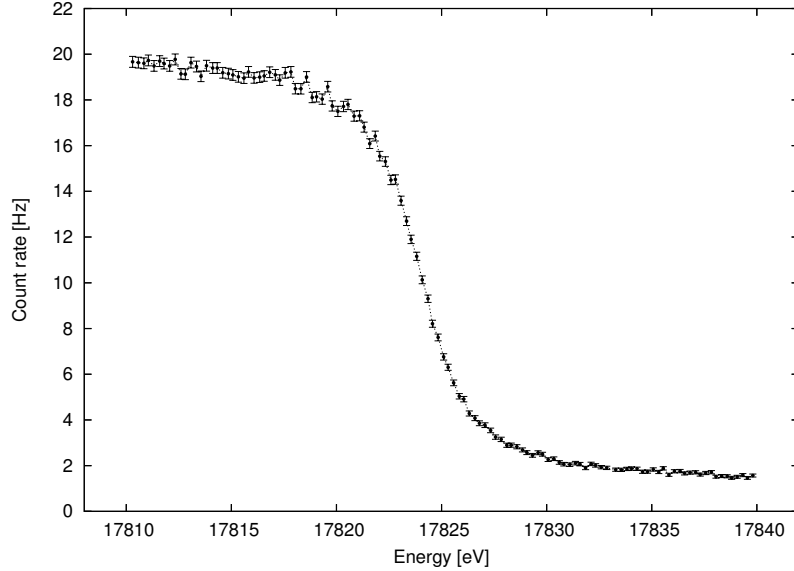


Figure 4.7 A narrow scan of the $^{83}\text{Rb}/^{83\text{m}}\text{Kr}$ K-32 line as recorded by the Mainz spectrometer operated with energy resolution of 1.5 eV at 17.8 keV.

of 19.5 Hz, the background of 1.3 Hz, the line position of $17\,824.83 \pm 0.03$ eV, and the line width of 3.16 ± 0.12 eV. $\chi^2/\text{d.o.f.} = 0.94$.

Estimating the contribution of electrical inhomogeneities to 0.5 eV, thus increasing the theoretical resolution to 2.0 eV we get the fitted parameters: the amplitude of 19.4 Hz, the background of 1.3 Hz, the line position of $17\,825.12 \pm 0.03$ eV, and the line width of 2.96 ± 0.12 eV. $\chi^2/\text{d.o.f.} = 0.94$. The fit is shown in fig. 4.8.

Both the fits provide reliable parameter values, and the values of line positions differ significantly by 0.29 eV, i.e., by $\sim 10\sigma$. One should take care of that if calibrating the energy scale.

In the fig. 4.9 a low energy tail of the K-32 line is shown proving a perfect quality of the electron source measured, i.e., no disturbing kinks or jumps are apparent at the low energy tail, and the count rate is raising very slowly towards the low energies.

4.1.3.2 L-9.4 lines

A wide scan of a L1-9.4 line (populated in both ^{83}Rb and $^{83\text{m}}\text{Kr}$ decays) is shown in fig. 4.10 measured with resolution of 0.6 eV at 7 840 eV (the same spectrometer setup as for the K-32 measurements in the previous section). A zoom of L1-9.4 line is in the fig. 4.10 as well. The same region can be measured by the Rez/Prague ESA 12 spectrometer. Then, the data can provide valuable comparison. Anyway,

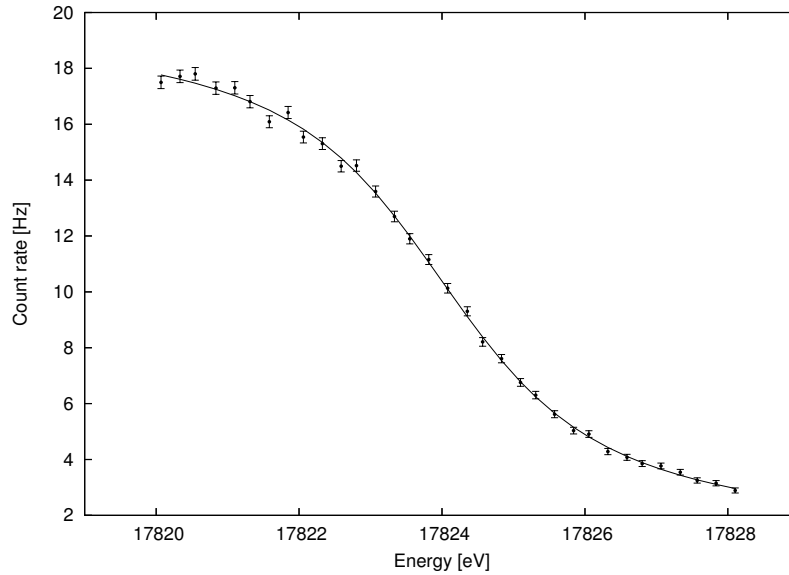


Figure 4.8 A fitted K-32 line. There were four free fit parameters: the line position, the line width, the amplitude and the background. Possible inhomogeneities of both the electric and magnetic field at the analyzing plane were neglected.

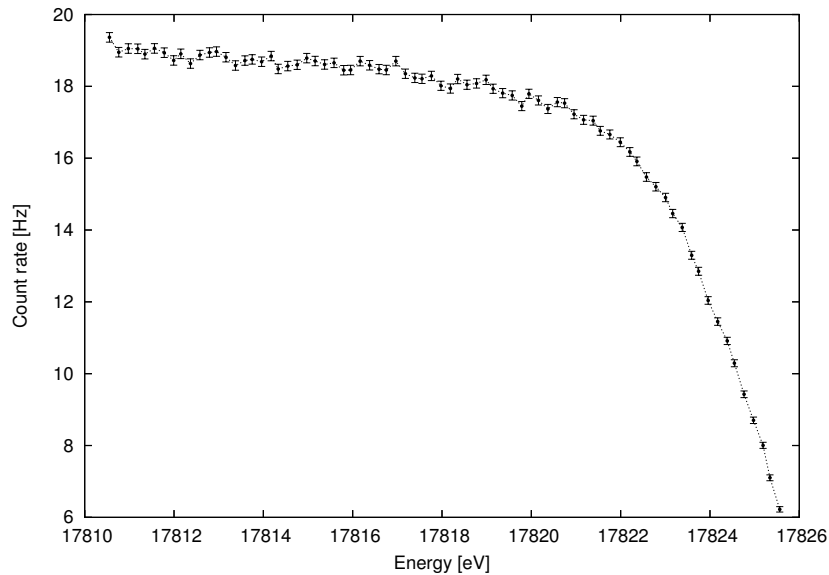


Figure 4.9 A low-energy tail of the $^{83}\text{Rb}/^{83\text{m}}\text{Kr}$ K-32 line reporting on good quality of the solid $^{83}\text{Rb}/^{83\text{m}}\text{Kr}$ source. No disrupting effects are present, and the count rate is raising very slowly towards the low energies.

one should take into account that detector efficiency at L1-9.4 region is about 3 times lower (a very rough estimation) than efficiency at the K-32 energy region.

4.1.3.3 L-32 lines

Finally, keeping the spectrometer setup constant we scanned the L-32 lines region with resolution of 2.6 eV at 30 470 eV. The result and a zoom of the L3-32 line is shown in fig. 4.11 The data report on properties of the Mainz spectrometer.

4.1.4 Conclusions of the $^{83}\text{Rb}/^{83\text{m}}\text{Kr}$ measurements

All the $^{83}\text{Rb}/^{83\text{m}}\text{Kr}$ lines we are interested in were clearly observed with no disturbing background. Source quality seems to be superior to monitor the energy scale. On the other side, source intensity should be definitely enhanced. (Few hundred times stronger sources have been already produced and tested in Rez.)

The Mainz spectrometer can be operated with the energy resolution of 1.5 eV at 17.8 keV. The setup is stable from the electron energy of 7.4 keV up to 30.5 keV. Inhomogeneities of neither the electric field nor the magnetic field were observed. The measured lines were easy to fit. The Mainz spectrometer proved to be a great device for the following development of a $^{241}\text{Am}/\text{Co}$ photoelectron source.

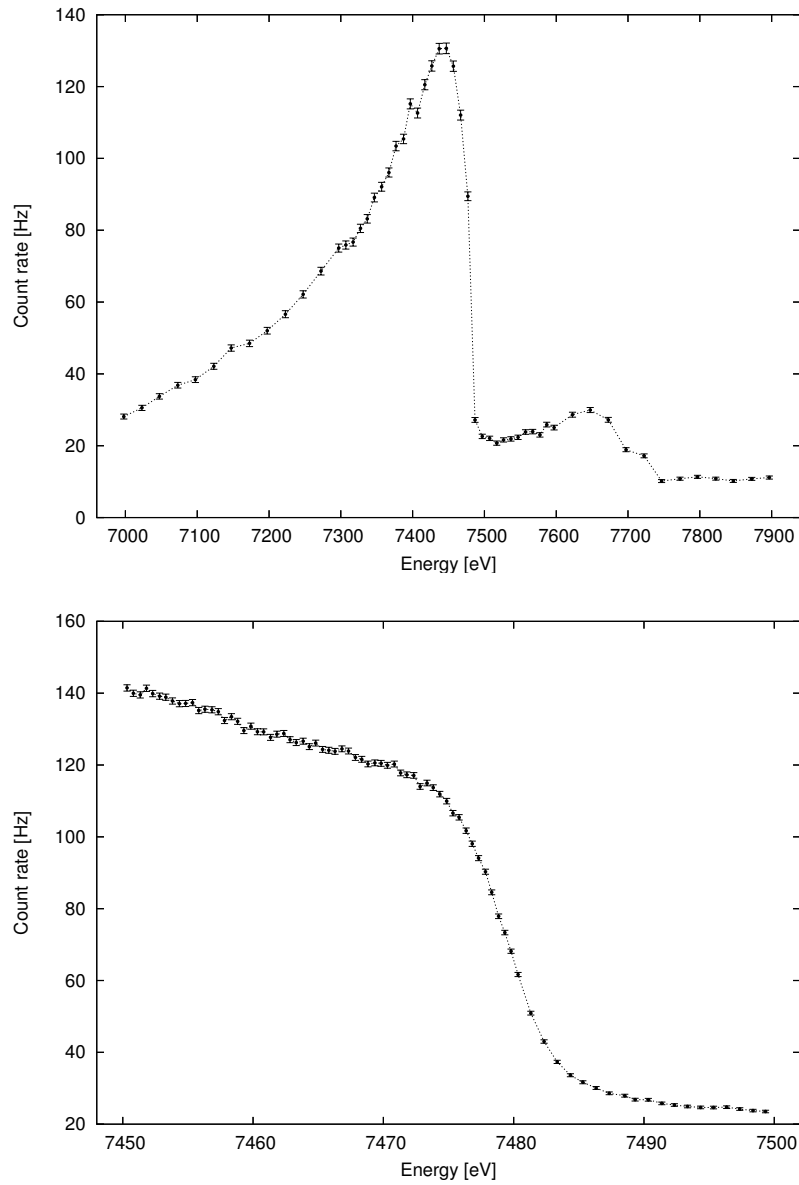


Figure 4.10 $^{83}\text{Rb}/^{83\text{m}}\text{Kr}$ L-9.4 lines as recorded by the Mainz spectrometer provide a valuable input for the $^{83}\text{Rb}/^{83\text{m}}\text{Kr}$ solid source development. A wide scan of L-9.4 lines at the top, and a zoom of the L1-9.4 line at the bottom.

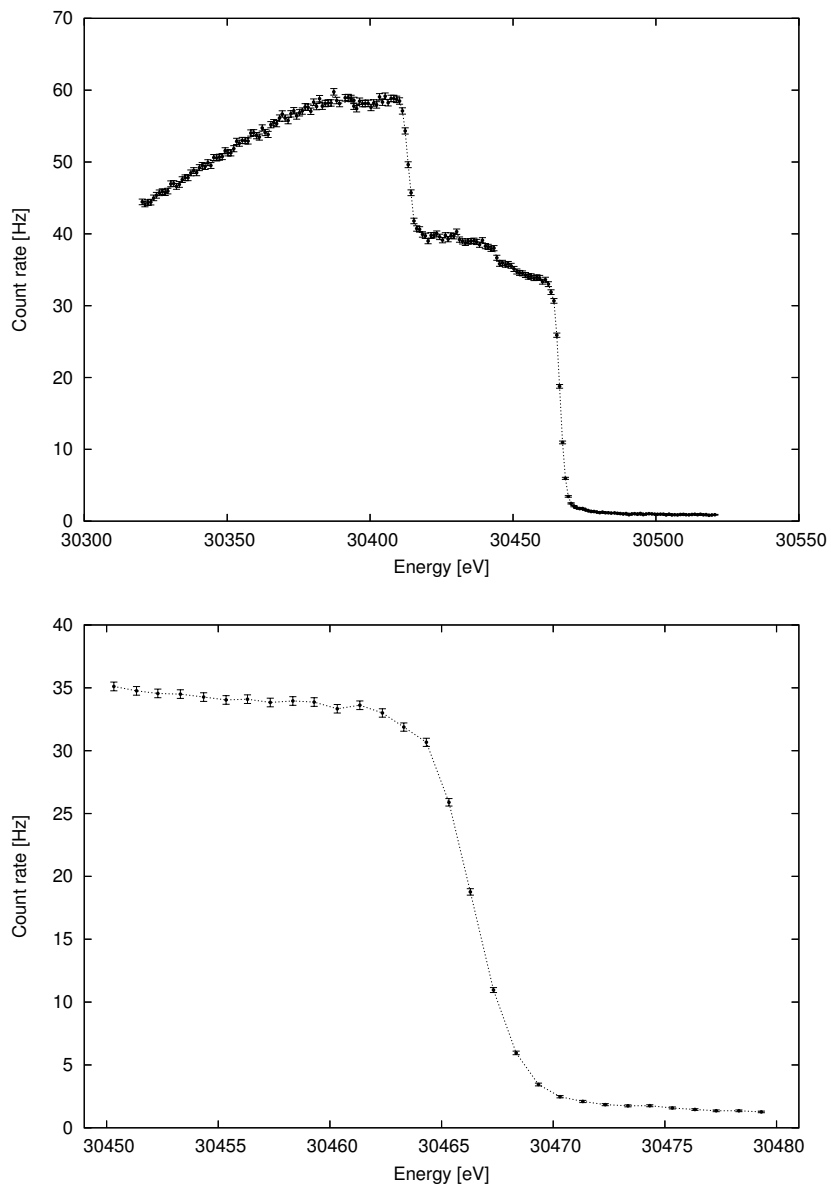


Figure 4.11 $^{83}\text{Rb}/^{83\text{m}}\text{Kr}$ L2,L3-32 keV lines at the top, and a zoom of the L3-32 keV line at the bottom as measured by the Mainz spectrometer operated with the energy resolution of 2.6 eV at 30 470 eV.

4.2 Am/Co measurements at Rez

From September, 2003 to April, 2004 tests of a $^{241}\text{Am}/\text{Co}$ source were running at the NPI Rez aiming to check ability of the source to produce monoenergetic electrons in sufficient count rate to monitor the energy scale of the KATRIN experiment. Further, we aimed to estimate the count rate expected in the monitor spectrometer, and to find the best thickness of a Co converter with respect to signal to background ratio. We did not hope to report on stability of the source and/or zero energy-loss electrons ratio.

4.2.1 ESA12 spectrometer setup

The ESA12 spectrometer is a differential double-pass cylindrical mirror spectrometer with a pre-retardation lens. Retardation was not used during the measurements to gain the maximum transmission (solid angle) of 0.74% out of 4π . In this measurement mode, the instrumental relative energy resolution was $\Delta E/E = 0.011$ (FWHM), and luminosity of 0.007 out of 4π . It is a nonbakeable system reaching vacuum level of 10^{-7} mbar². Electrons are detected by a windowless channel electron multiplier (CEM).

The ^{241}Am source used was a commercial source by Amersham. It is a technically closed source with a 1 mm Be window of 8 mm in diameter with activity of 1.11 GBq (30 mCi) [30]. ^{241}Am decays to ^{237}Np emitting a number of gamma lines, with a dominant 59.6 keV line. The intensity of the dominant transition is 35.9 per 100 decays. As introduced in section 3.2, the gamma line of interest is the 26.3 keV transition with the intensity of 2.4 per 100 decays. Due to high activity of the ^{241}Am source with the half-life of 432 years, and small geometrical size, 26.3 keV gammas suffer from serious self-absorption.

The effect was simulated by MC means and the suppression factor in intensity of 26.3 keV photons emerging from this Amersham source was estimated to 2.2. The MC simulation covered the geometry of the ^{241}Am source, and gammas scattering in enamel and ^{241}Am . A measurement confirmed the factor value, indicating a good understanding of the gamma-ray source in the MC sense. It is thus obvious that further increasing of the source activity would not be beneficial.

² At present, the spectrometer vacuum amounts to 10^{-8} mbar thanks to an upgraded vacuum part.

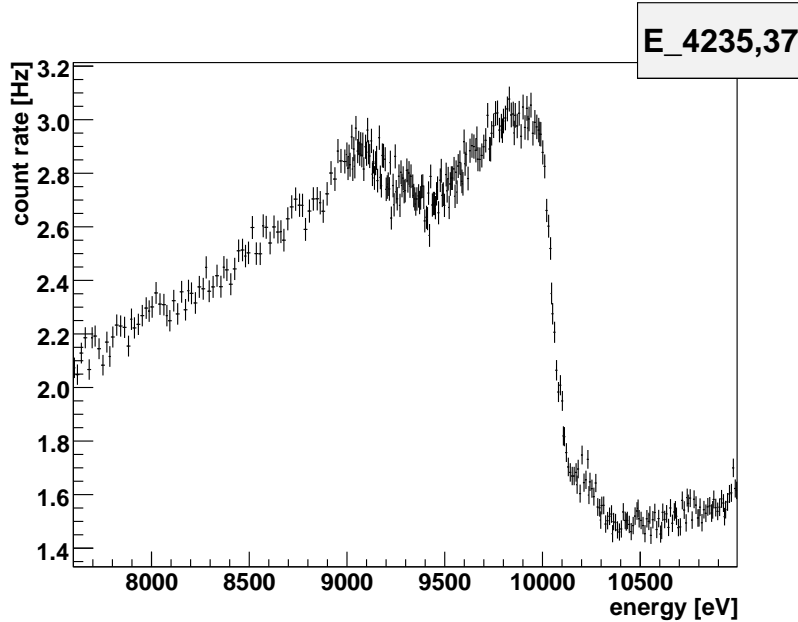


Figure 4.13 Photoelectrons emitted from Co K-shell by Np L X-rays with energy of 17.8 keV, measured with the ESA 12 electron spectrometer.

The 59.6 keV photons contribute mainly to background of the photoelectron spectrum (due to low energy tails of photo-electron lines emitted from the cobalt converter). Other contribution to background originate in ^{237}Np L X-rays undergoing photoeffect on various Co shells. The ^{241}Am source emits $\sim 10^4$ neutrons/sec/Ci. Their contribution to measured background is fully negligible.

To monitoring of the KATRIN experiment, we are interested in photoelectrons emitted from the Co K shell by Am gammas with energy of 26.3 keV. The kinetic energy of such photoelectrons falls into the energy region of 18.6 keV. The energy region of 18.6 keV is at the edge of possibilities of the ESA 12 electron spectrometer. With respect to low luminosity and resolution of 205 eV at 18.6 keV, we focused on ^{237}Np L X-rays with energies of 13.9 and 17.8 keV. These are much broader than the 26.3 keV line. Anyway, the width is completely negligible compared to the spectrometer resolution.

4.2.2 $5\ \mu\text{m}$ Co converter

First, a $5\ \mu\text{m}$ Co foil by Goodfellow was studied starting with an electron line with the energy of 6.24 keV emitted from Co K-shell by Np L X-rays with the energy of 13.9 keV. The line measured with energy resolution of 66 eV (FWHM) ($\Delta E/E = 0.011$) is shown in fig. 4.12.

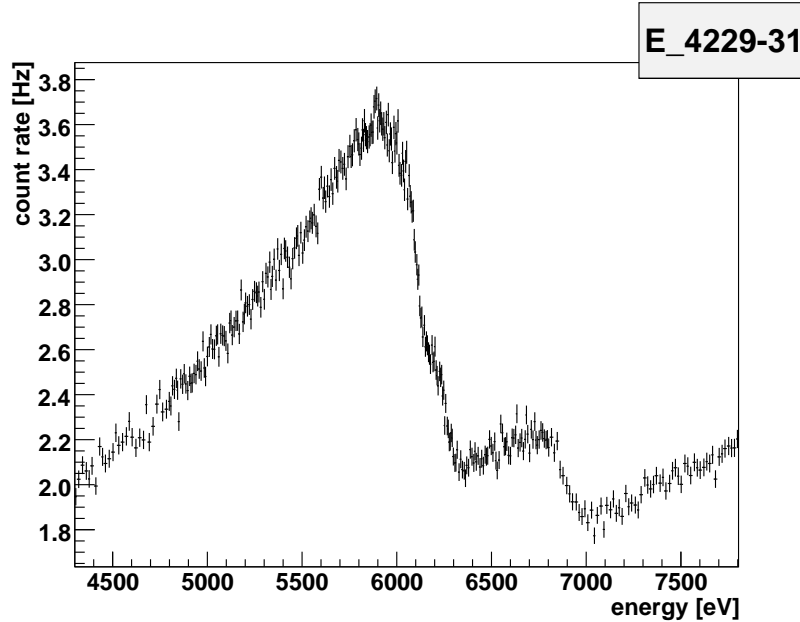


Figure 4.12 Photoelectrons emitted from Co K-shell by Np L X-rays with energy of 13.9 keV, resulting in kinetic energy of zero energy-loss electrons of 6.2 keV, measured with the ESA 12 electrostatic spectrometer.

Then, we switched to an energy region of photoelectrons emitted from Co K-shell by Np L X-rays with the energies of 17.8 keV. The lines measured with energy resolution of 100 eV are shown in fig. 4.13

These electron lines were compared to a MC simulation in fig. 4.14. In our MC calculation (model approach described in [31], the arrangement of the ^{241}Am emitter, angular distribution of photoelectrons, their scattering and energy losses in a cobalt layer, and also the setup of the ESA 12 spectrometer were taken into account, including the detector efficiency of 0.24 [32]. A reasonable conformity of the MC simulation with the experimental data is apparent. Some deviations may result from uncertainties in the structure of the commercial ^{241}Am emitter, ESA 12 transmission and detector efficiency. We would like to stress, that there is no free parameter in the MC simulation but background.

Then, background was checked to identify low energy tail contributions to the measured spectra. A background scan with the ^{241}Am source inside the spectrometer without the Co converter was done resulting in mean count rate of $0.698 \pm 0.002 \text{ s}^{-1}$ in the energy region of interest. A background measurement with the ^{241}Am source removed from the spectrometer resulted in $0.534 \pm 0.005 \text{ s}^{-1}$. Both the measurements are shown in fig. 4.15.

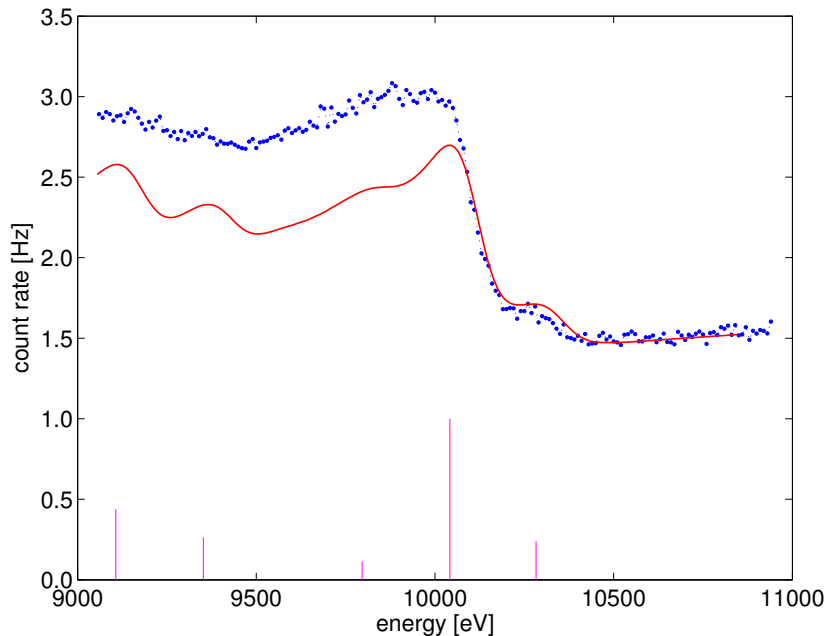


Figure 4.14 A part of the $^{241}\text{Am}/\text{Co}$ photoelectron spectrum taken in the ESA 12 spectrometer with a $5\ \mu\text{m}$ foil. The solid line represents a Monte Carlo simulation of ^{237}Np X-ray photoelectron energy distribution in this region (see text). The instrumental energy resolution and transmission of the spectrometer are 100 eV and 0.74% of 4π , respectively. The vertical bars show the positions of X-ray photoelectrons. The heights of the bars are proportional to the tabulated ^{237}Np X-ray intensities.

The small difference in between the measurements can be explained by true secondary electrons populated by the ^{241}Am gammas on the full electrodes of the spectrometer. These randomly travel through the spectrometer, and few of them hit the detector contributing to background. The low-energy tails contribution of about 0.9 Hz would be a disaster in the monitor spectrometer, but this experience can not be directly transferred, because there are many intense electron lines above this region compared to region of 18.6 keV.

4.2.3 $3\ \mu\text{m}$ Co converter

$3\ \mu\text{m}$ Co converter by the Goodfellow was studied, because it is the thinnest self-supported Co foil available. Optically it exhibits more homogeneous surface than the $5\ \mu\text{m}$ foil, with two different surfaces. The first one is shine, while the other looks dim. Starting with the shiny face towards the spectrometer the fig. 4.16 was

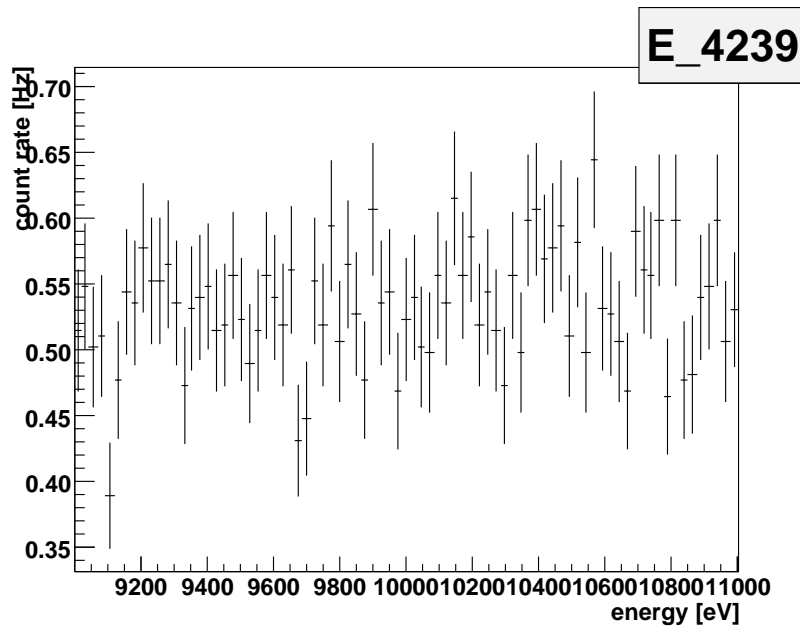
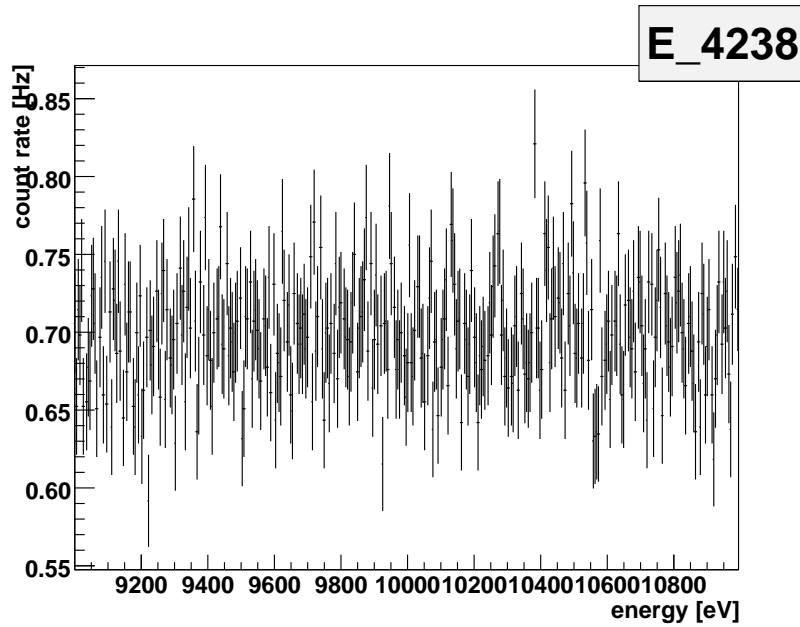


Figure 4.15 At the top, a background measurement with the Am source inside the ESA 12 electron spectrometer without the Co converter, and at the bottom a background measurement without both the Am source and the Co converter are shown.

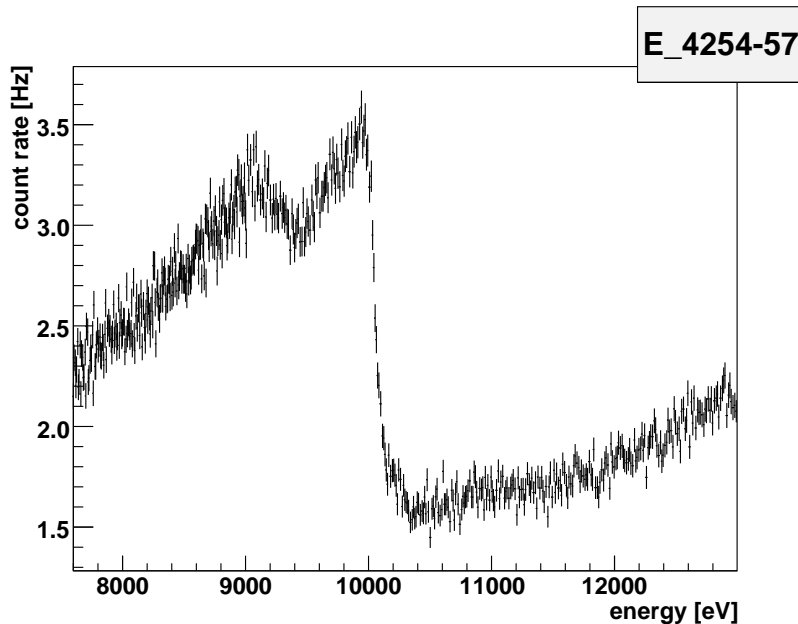


Figure 4.16 Photoelectrons emitted from $3\ \mu\text{m}$ Co K-shell by Np L X-rays with energy of 17.8 keV. The shiny surface of the Co foil faced the EAS 12 spectrometer.

obtained in the usual energy range of photoelectrons emitted from Co K-shell by Np L X-rays with the energies of 17.8 keV.

The spectrometer setup was exactly the same as in the previous scan in fig. 4.13. The foil performed significantly better than the the $5\ \mu\text{m}$ foil.

Planning a measurement with the dim face of foil towards the spectrometer we suffered with a CEM failure. Thanks to immediate resuscitation it recovered in about a week. Definitely its efficiency was lower than before the failure. To demonstrate that fig. 4.17 was recorded to reproduce fig. 4.16. The cause of the CEM accident has remained unexplained.

To conclude, $3\ \mu\text{m}$ Co performed better than the $5\ \mu\text{m}$ one, exhibiting higher count rate, and more homogeneous surface. So far, it was the leading candidate for a Co converter.

4.2.4 $0.1\ \mu\text{m}$ Co converter

$0.1\ \mu\text{m}$ Co foil is the thinnest Co converter produced. Unfortunately it is deposited on a $3.5\ \mu\text{m}$ Mylar foil, and hence it is unbakeable and can not be etched with Ar ions. This may be unacceptable in the monitor spectrometer. Thanks to the

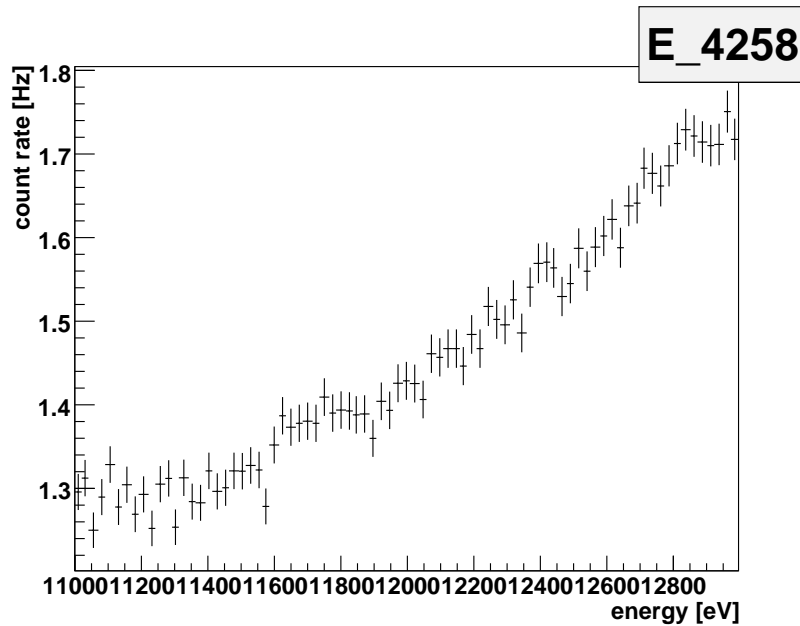


Figure 4.17 Photoelectrons emitted from $3\ \mu\text{m}$ Co converter as recorded after the detector failure.

thickness of $0.1\ \mu\text{m}$ it should exhibit practically no background, while the effect intensity should be kept. And thanks to the way it is manufactured, it should also be the most homogeneous foil within the ones tested. And this showed to be correct in fig. 4.18 scanned with exactly same setup as the previous $3\ \mu\text{m}$ and $5\ \mu\text{m}$ foils.

KLL Auger lines and K-13.9 keV Co line reports on how low energy electrons can escape the Co foil and how fast the low energy tail drops. Both indicate high foil quality in fig. 4.19

4.2.5 Ar etching

To guarantee a reproducible Co surface free of Co oxides Ar etching was employed. The $3\ \mu\text{m}$ Co foil studied before was etched by Ar ions in the Institute of Physics, ASCR, Prague. In order to etch the foil, it was glued to a Al backing. It was not feasible to solve the glue after the etching without contamination of the etched surface. The count rate suppression due to $17.8\ \text{keV}$ ^{241}Am gammas absorption in the Al backing was estimated by factor 0.27.

As a reference we scanned a new $3\ \mu\text{m}$ foil as delivered. For the data recorded with the shiny face towards the spectrometer see fig. 4.20. Contrary to our expectation, the dim surface of the foil performed even better. The scan is shown in fig. 4.21.

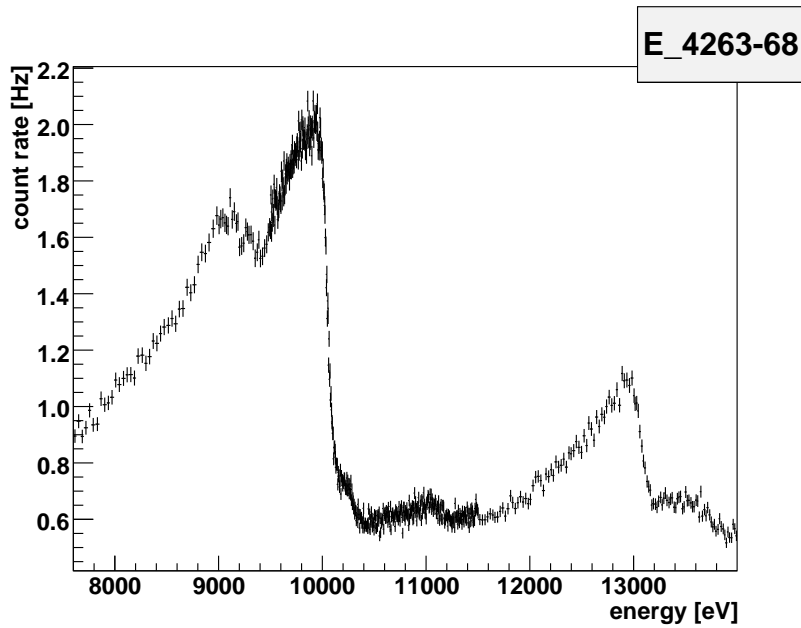


Figure 4.18 Photoelectrons emitted from 0.1 μm Co foil deposited on a Mylar backing, measured by the ESA 12 electron spectrometer.

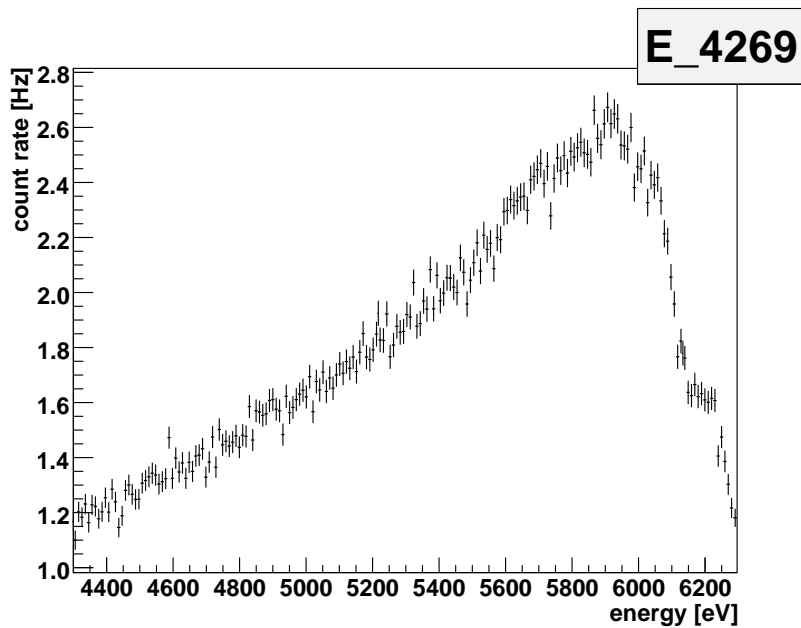


Figure 4.19 KLL Auger line and K-13.9 keV photoelectron line emitted from the 0.1 μm Co foil deposited on a Mylar backing.

Finally, the etched foil was measured. The result is shown in fig. 4.22. Actually,
78

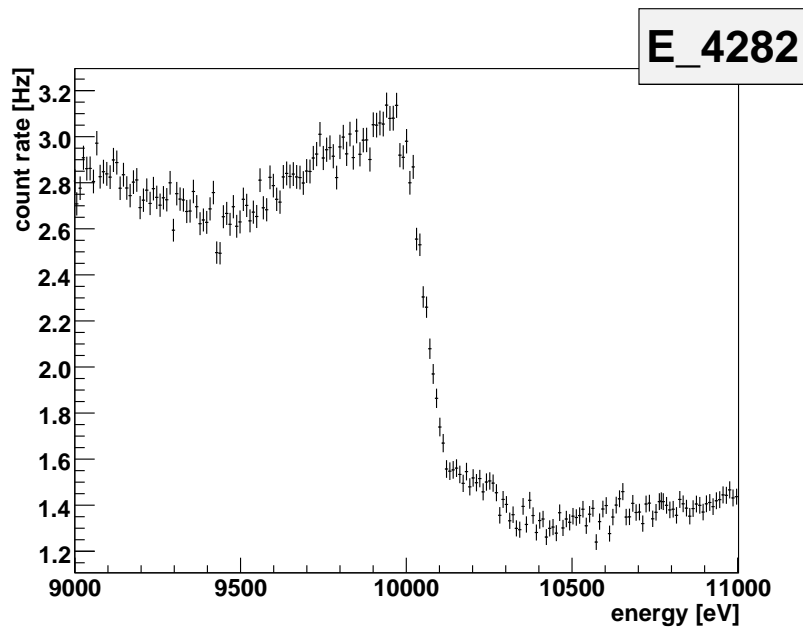


Figure 4.20 Photoelectrons emitted from $3\ \mu\text{m}$ Co converter as delivered with the shiny surface facing the spectrometer.

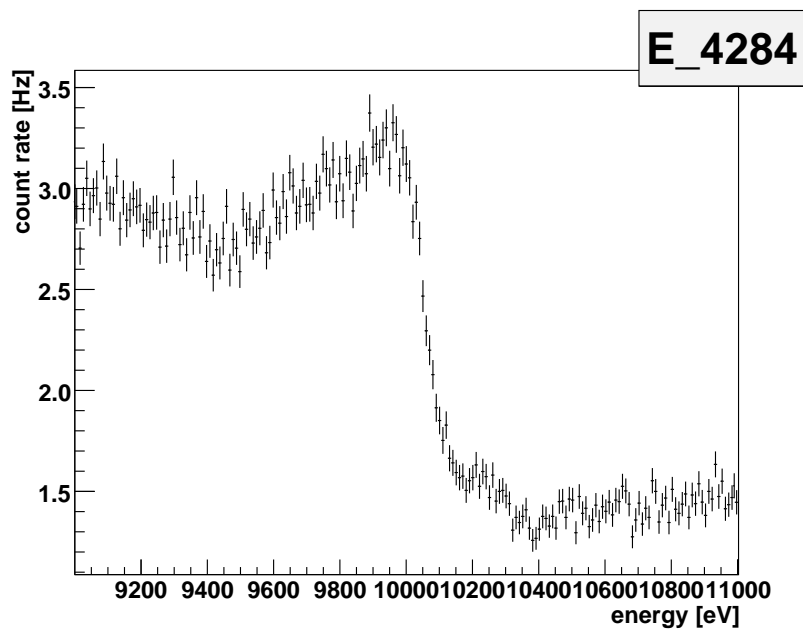


Figure 4.21 Photoelectrons emitted from $3\ \mu\text{m}$ Co converter as delivered with the dim surface facing the spectrometer.

no change of count rate was observed after the Ar etching.

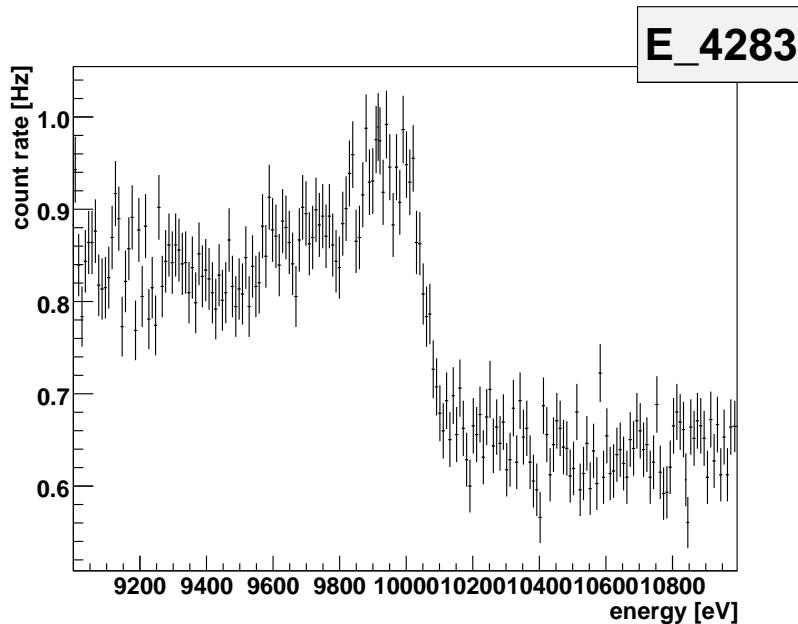


Figure 4.22 Photoelectrons emitted from the etched Co foil by Np L X-rays with energy of 17.8 keV, measured by the ESA 12 electron spectrometer.

4.2.6 Conclusions of the Rez measurements

^{241}Am photoelectron source looks feasible in principle. The concept was tested in energy regions reachable with the ESA12 spectrometer. Measurements with resolution of 100 eV correspond well to MC simulation. There was no free parameter in the MC simulation but background. As for various Co foil comparison, the $5\ \mu\text{m}$ is optically less homogeneous than the $3\ \mu\text{m}$ one, which even perform better in both the absolute count rate and the effect to background ratio.

As far as background is concerned, the $0.1\ \mu\text{m}$ Co foil deposited on $3.5\ \mu\text{m}$ Mylar backing exhibits the lowest background in general, and low energy tails drop fast thanks to lower probability of electrons to loose energy within the Co layer Unfortunately this foil is not bakeable, and can not be sputtered with Ar ions to clean the surface. So finally, Ar etching was tested using the $3\ \mu\text{m}$, and no change of count rate was observed.

Zero energy-loss electrons are critical for monitoring of the energy scale, and we can not report on them due to low luminosity of the ESA12 spectrometer. Anyway, the leading candidate for a Co converter is the $3\ \mu\text{m}$ Co foil as delivered.

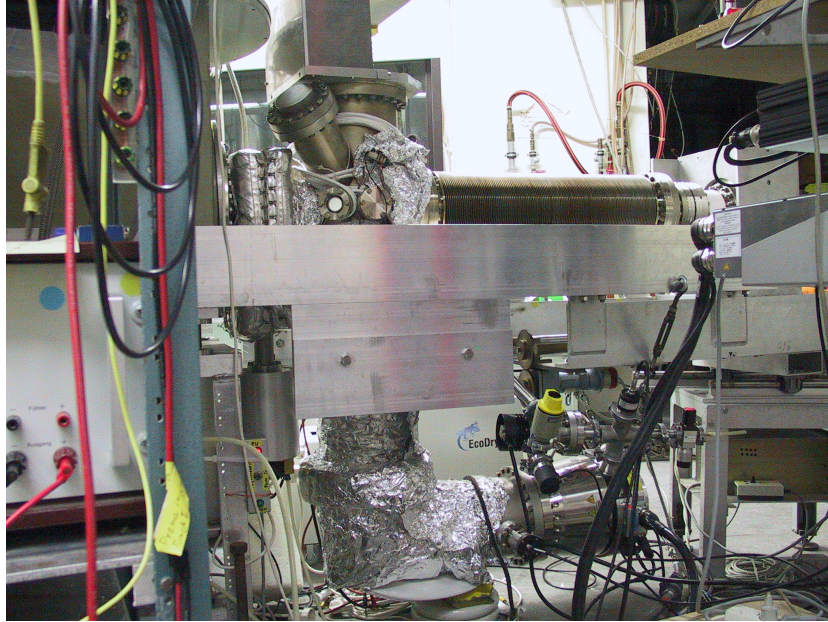


Figure 4.23 An opposite view of the typical setup of the $^{241}\text{Am}/\text{Co}$ source part at Mainz with a cascade of turbo pumps, and an Ar inlet valve.

4.3 Am/Co measurements at Mainz

In spring 2005, a feasibility study of a $^{241}\text{Am}/\text{Co}$ source was completed in Mainz aiming to prove suitability of the $^{241}\text{Am}/\text{Co}$ concept to monitor the energy scale of the KATRIN experiment. The source part of the Mainz spectrometer was reassembled to house the $^{241}\text{Am}/\text{Co}$ source. The new setup allowed the $^{241}\text{Am}/\text{Co}$ source:

- to be placed directly to the spectrometer magnet "B"
- to be parked in the chamber to be Ar etched
- to exchange Co foils.

The setup overview is in fig. 4.1 on page 60. The opposite view is then in fig. 4.23. The $^{241}\text{Am}/\text{Co}$ source was mounted in an ESA12 holder (the one used at the Rez/Prague ESA12 spectrometer), and then fixed in a former quenched condensed tritium source (see fig. 4.2 on page 61). A proper position of the $^{241}\text{Am}/\text{Co}$ source in both the chamber and the spectrometer magnet was guaranteed by a subtle detail shown in fig. 4.24.

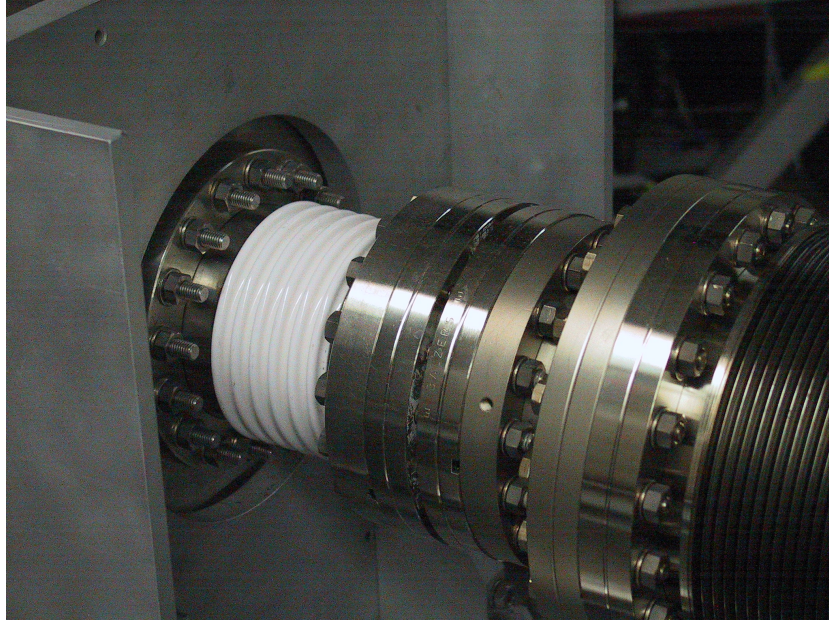


Figure 4.24 A subtle detail of the standard setup of the $^{241}\text{Am}/\text{Co}$ source part to guarantee a proper position of the $^{241}\text{Am}/\text{Co}$ source in both the chamber and the spectrometer magnet of the Mainz spectrometer.

Thanks to a 1500 l/s turbo pump, the source part of the spectrometer could be pumped down to 2×10^{-9} mbar if baked up to 250°C . Besides the original full electrodes, the spectrometer was equipped with two wire electrodes; the intermediate one at the central part of the spectrometer [33], and the inner one covering also the conical parts of the spectrometer, and capable to produce quadrupole electric field [34]. A segmented Si detector (3 rings, 1 cm^2 each) exhibiting resolution of 1.5 keV at the energy region of 20 keV was operated on 40 V.

4.3.1 ^{57}Co check

For a convenient introduction to MAC-E-Filter, a well defined ^{57}Co source was employed to check transmission and efficiency of the Mainz spectrometer, to optimize source position in the magnet B, and to optimize Earth field compensation coils. The ^{57}Co source was produced in Dubna in July 1997 with activity of 640 kBq. Due to the half-life of 272 days the resulting number of K-14.4 electrons was 289 s^{-1} in July, 2005. The source was extensively studied at Rez.

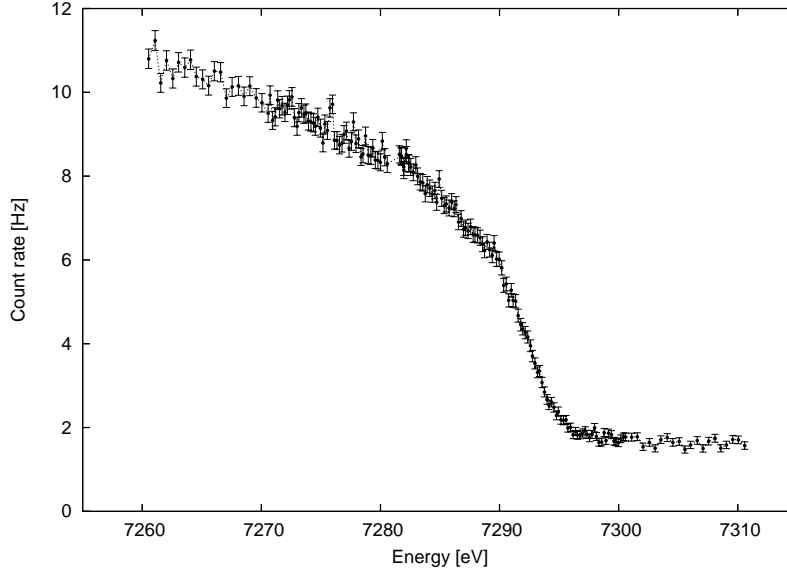


Figure 4.25 ^{57}Co K-14.4 line scanned by the Mainz spectrometer with the energy resolution of 0.8 eV at 7.5 keV

Besides the K-14.4 line emitting electrons with the kinetic energy of 7301 eV, L-14.4 electrons with zero energy-loss components of 13568, and 13692 eV are produced. (All the kinetic energies do not include work functions.)

The ^{57}Co source was moved into the magnet B 1 cm back from the Ti ground electrode in the magnet. The distance was measured by means of a closed electric loop of a thin Cu wire placed in front of the cup housing the ^{57}Co source. The Ti electrode is 25 cm long [35]. Assuming, it is placed at the centre of the magnet, the ^{57}Co source was 13.5 cm off center. This distance was used to calculate spectrometer resolution.

Both the spectrometer magnets were charged up to 50 A (6 T), the detector magnet C up to 60 A (1.7 T). The air coils were set to +8.6 A resulting in resolution of 3.5 eV at 7.5 keV. The source position in the magnet B was optimized first looking for the best signal to background ratio in the energy region of the K-14.4 line. Then the Earth field compensation coils were tuned. Both the steps were repeated three times with improving resolution (+8.6 A, -0 A, and -8.6 A in the air coils), resulting in the compensation coil currents of +5 A (horizontal) and +10 A (vertical).

Then the K-14.4 line was scanned with the resolution of 0.8 eV at 7.5 keV ($I_{air} = -8.6$ A, $B_A = 7.0$ G) applying the constant high voltage of 7350 V to the analyzing plane, and stepping the voltage applied to the ^{57}Co source from 30 V to 80 V in 0.2 V steps. All the voltages were applied with the negative polarity. The measurement time was 250 s/bin. The result is shown in fig. 4.25.

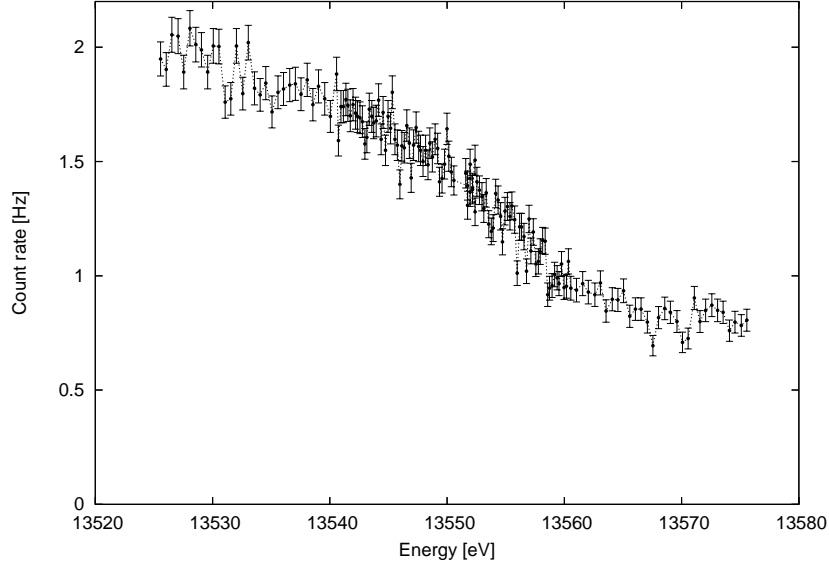


Figure 4.26 ^{57}Co L2-14.4 line scanned by the Mainz spectrometer with the energy resolution of 1.6 eV at 13.5 keV

Keeping the spectrometer setup fixed we scanned the L2-14.4 line with resolution of 1.6 eV at 13.5 keV corresponding to 0.8 eV at 7.5 keV. The result is shown in fig. 4.26. The measurement time was 350 s/bin, and the line was scanned in a single sweep.

The measured count rates are in perfect agreement with our expectation assuming the accepted angle of 0.26 out of 4π and the detector efficiency of 0.9. The K-14.4 line seemed to be little suppressed compared to the L2-14.4 lines. This can be caused by slightly worse detector efficiency for 7.3 keV electrons. A biasing voltages of 3 kV and 1 kV were applied to the ^{57}Co source, but the setup was unstable with significantly higher detector noise.

Further, a tilted geometry of the source was introduced as shown in fig. 4.27 to cut down gamma background if necessary. In the case of $^{241}\text{Am}/\text{Co}$ source, it was planned to cut down the background contribution from Am X-rays in 17.9 keV region, if any observable. Later on, the former geometry will be referred as the direct one. The ^{241}Am source is contained in a monel shielding [30]. ^{241}Am gammas may leave the source with angle lower than 58° . Therefore we tilted the source by 65° .



Figure 4.27 A holder of an electron source for the tilted geometry to cut down background.

Keeping the spectrometer setup constant, the ^{57}Co source position was optimized. The optimization resulted in lowering the source by 1 mm. The Earth compensation coils currents remained untouched. The results of the K-14.4 line scan is given in fig. 4.28

To demonstrate the effect of the lowered 1 mm we scanned the same line again in the former position of the direct geometry. The result is shown in fig. 4.29. And just for completeness, a scan of L2-14.4 line in the tilted geometry follows in fig. 4.30. Although the line looks ugly, the count rate drop due to the tilted geometry can be estimated.

To conclude, the transmission of the spectrometer is fine, and in the tilted geometry is the luminosity lower by factor 2.0.

4.3.2 Adiabatic mode of the Mainz spectrometer

Then, the $^{241}\text{Am}/\text{Co}$ source with the $3\ \mu\text{m}$ Co foil was put in the holder in the direct geometry. All the magnets were charged up to 30 A, and the air coils were set to +2 A. Setting the voltage at the analyzing plane to $U_0 = -18.9\ \text{kV}$ the $^{241}\text{Am}/\text{Co}$ source was scanned with voltage from $-200\ \text{V}$ to $-300\ \text{V}$ in 2 V steps expecting a line at 18,636 eV. The detector window from 15 keV to 21 keV was used. The result is given in fig. 4.31 showing a vanishing effect on the background of 3.2 kHz.

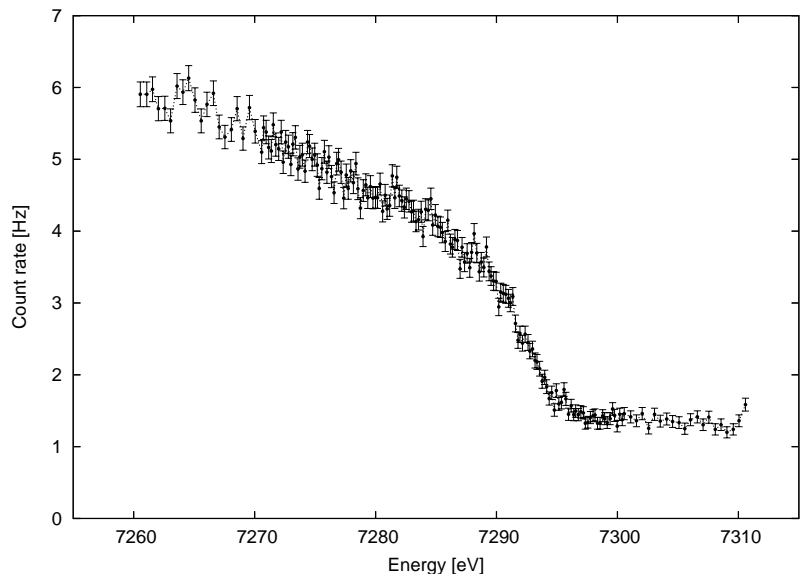


Figure 4.28 ^{57}Co K-14.4 line measured by Mainz spectrometer with resolution of 0.8 eV at 7.5 keV in the tilted geometry.

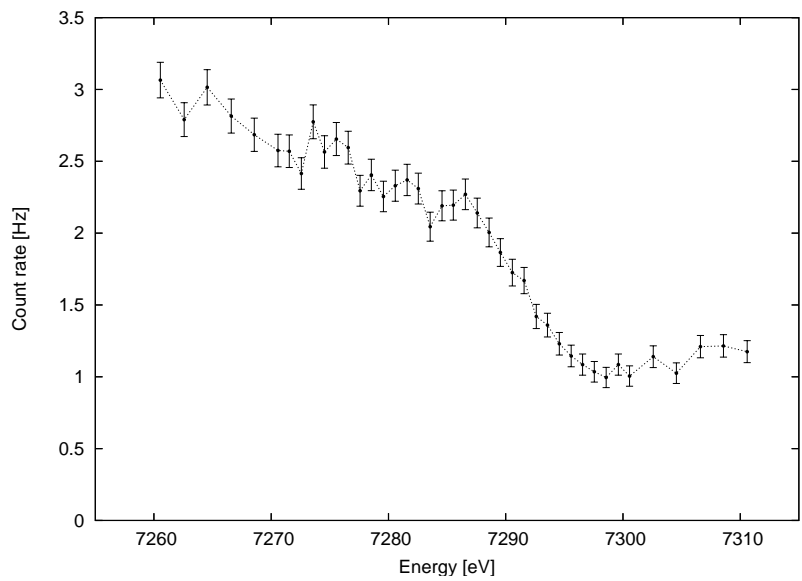


Figure 4.29 ^{57}Co K-14.4 line measured with resolution of 0.8 eV at 7.5 keV in the tilted geometry. The source position corresponded to the position in the direct geometry.

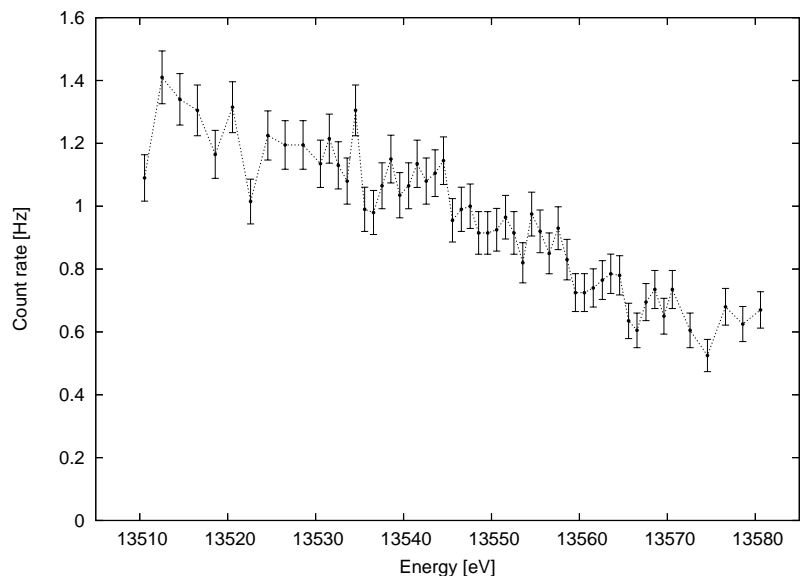


Figure 4.30 ^{57}Co L2-14.4 line scanned with the energy resolution of 1.6 eV at 13.5 keV in the tilted geometry.

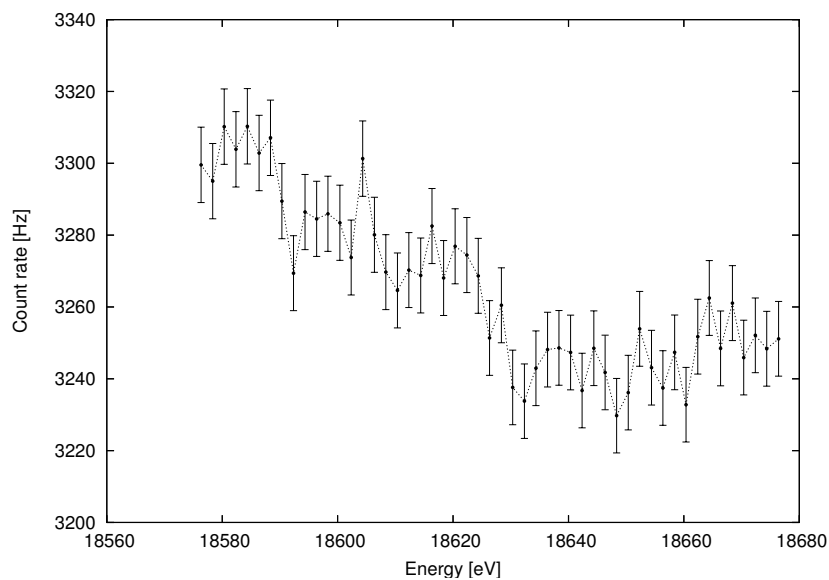


Figure 4.31 The $^{241}\text{Am}/\text{CoK-26.3}$ line measured by the Mainz spectrometer with the $3\ \mu\text{m}$ Co foil in the direct geometry. The spectrum is dominated by the gammas.

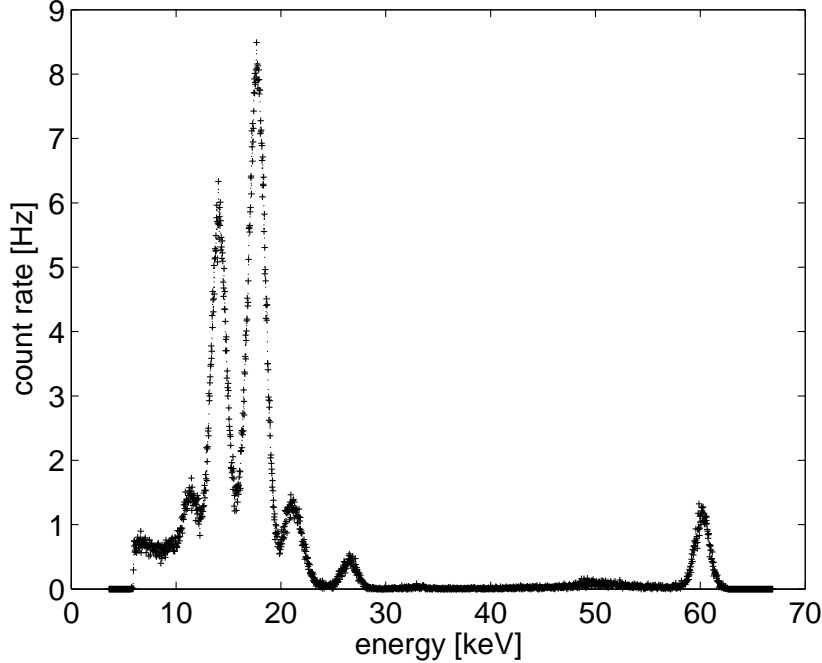


Figure 4.32 Gamma response of the detector of the Mainz spectrometer at the distance of 4.5 m from the $^{241}\text{Am}/\text{Co}$ source.

Further, we focused on identifying our background. Switching off all the magnets and electric fields fig. 4.32 was recorded by the detector. ^{241}Am 26.3 and 59.6 keV gammas can be easily identified, as well as Np X-rays. Further, there are many Am X-rays observable, due to self-absorption, reducing 26.3 keV line by factor 2.2. Unfortunately, all of these can undergo a photoeffect on the Co foil emitting electrons.

The critical gammas contributing to background may be avoided by the tilted geometry. From this moment on, all the measurements were performed in the tilted geometry, with 26.3 keV gammas shielded completely (and so the Np and Am X-rays), and with 59.6 keV line suppressed significantly. Gamma background was practically varying from 5–7 Hz in the detector window from 15 keV to 21 keV. The variations were driven by the $^{241}\text{Am}/\text{Co}$ source position in the holder.

The optimized position of the $^{241}\text{Am}/\text{Co}$ source is just about 1 mm above the ground electrode in the magnet B, and it is not possible to go lower to get reasonable insulation between the cup with the source and the ground electrode, The $^{241}\text{Am}/\text{Co}$ with the $0.1\ \mu\text{m}$ foil was mounted upside down because of the width of the foil in the Al holder (about 2 mm). To achieve the optimized position then we moved the source 1 mm up, increasing the distance to the ground electrode. Finally, the Earth coil compensation were tuned to maximize effect to background

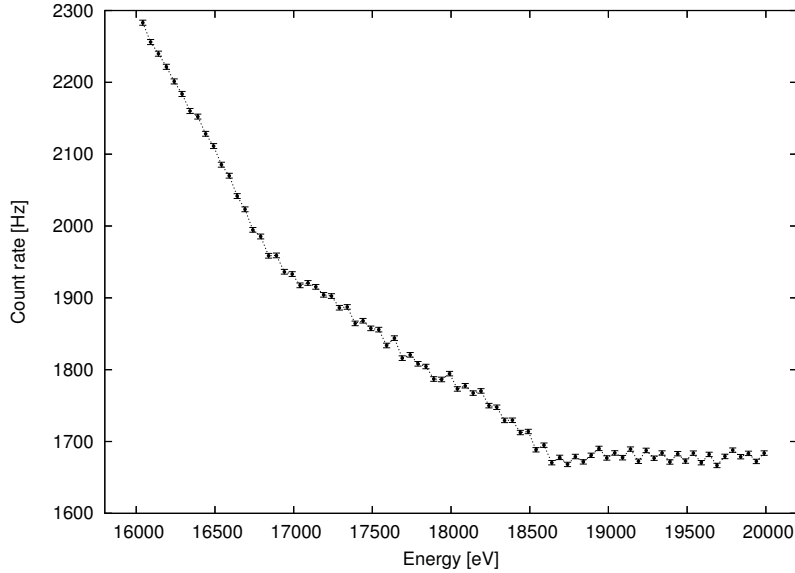


Figure 4.33 The $^{241}\text{Am}/\text{Co}$ K-23.6 line measured with resolution of 4.2 eV at 18.6 keV by the Mainz spectrometer in an adiabatic mode.

ratio in the energy region of 18.6 keV resulting in the compensation coil currents of +10 A (horizontal) and +20 A (vertical)

With such geometry and position the following spectrum was measured. Both the spectrometer magnets were charged up to 50 A (6 T), and the current of the detector magnet was 60 A (1.7 T). We went with moderate resolution of 4.2 eV at 18.6 keV produced by the air coil current of +1 A. The $^{241}\text{Am}/\text{Co}$ source was grounded, and the high voltage applied to the analyzing plane was changed in 50 V steps spending 180 s per bin. The spectrum is shown fig. 4.33.

4.3.3 Turning nonadiabatic

Direct ^{241}Am gammas reaching the detector were suppressed easily, but the background electrons are hard to beat, that is why an intentional breaking of adiabaticity was introduced. Electrons with the significant excess of kinetic energy at the analyzing area are not guided anymore by the magnetic field lines and hit the spectrometer wall. This is an unintended and unavoidable feature of MAC-E-Filters. In simple words, some electrons are too fast to follow the magnetic field lines.

In order to make the magnetic field lines losing ability to guide fast electrons, there are two principle ways: A. make the fields line bend rapidly, which is achieved by improved energy resolution, and B. decrease intensity of the magnetic fields. So

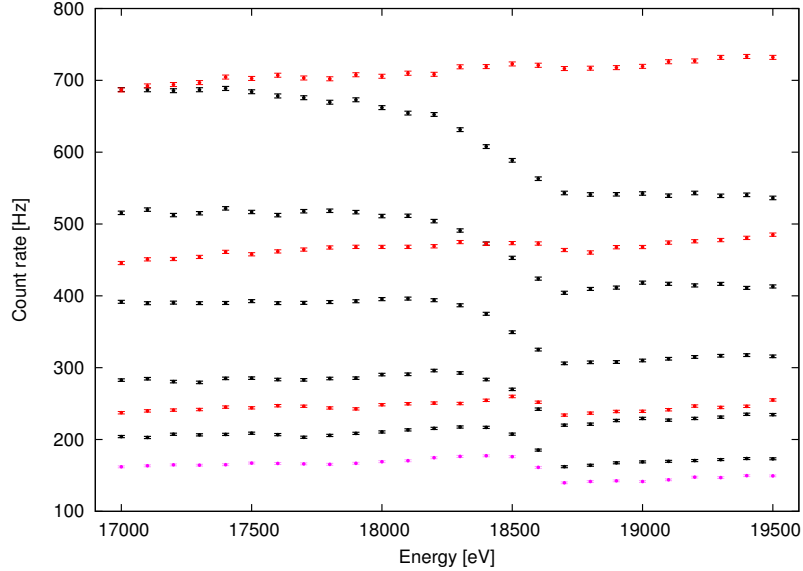


Figure 4.34 Searching for an adiabacity edge by varying energy resolution with a fixed magnetic flux. The edge is indicated with magenta.

it is obvious, that practically adiabacity is easy to break close to the electrodes, and unbreakable on the spectrometer axis. In that respect, a fine segmented detector could help, and/or a mechanical block on axis at the analyzing area. The latter idea is usually neglected because of worries, that the block would increase background.

The following iterative three step process was utilized to tune up nonadibacity. The magnetic flux was fixed, and energy resolution decreased until the signal to background ratio improved. An example is shown in fig. 4.34, with the black spectra being still too adiabatic for us, the magenta one being our favorite on the adiabatic edge, and the red ones being too nonadibatic. At the moment, when adiabacity is broken too much, all the electrons can leave their field lines, while the others (e.g. true secondary electrons produced on electrodes) can bind on them. As a consequence, signal is disappearing and background rising.

In the second step, the resolution found in the first step was fixed, and the portion of analyzing area mapped onto the detector was tuned by varying the detector magnetic field. Repeating, that adibacity breaks more likely at the outer parts of the analyzing plane, the background due to nonadiabacity comes preferably from the outer parts of the analyzing area. If the image is properly zoomed and aligned to the detector, these outer parts of the analyzing plane do not contribute to the signal. An example is shown in fig. 4.35. Usually, the signal to background ratio is optimized. And as the direct consequence, we gain space at the analyzing plane to tune energy resolution again.

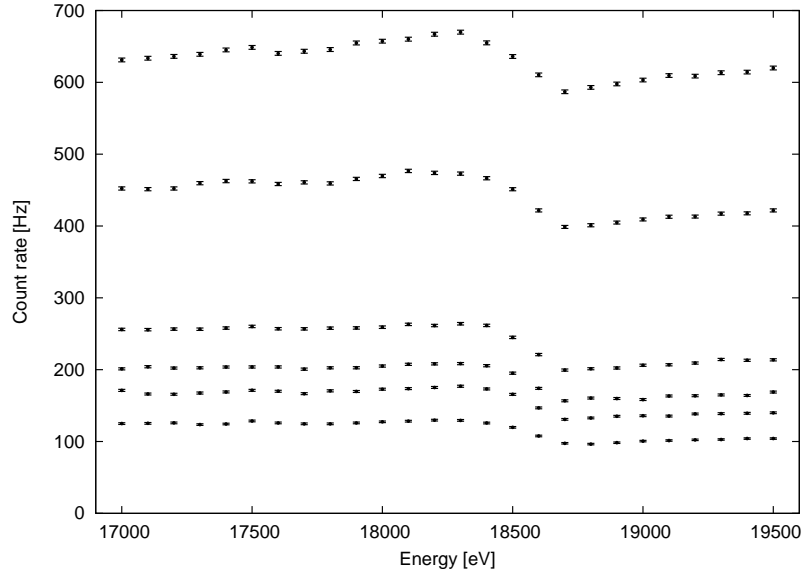


Figure 4.35 Optimizing the beam area mapped to the detector, keeping the energy resolution fixed.

There are several criteria to pick up the best setting in these two steps, and the signal to background ratio is the usual one. On the other side, keeping as much of the signal as possible is a valid choice as well, and was often used in the case of $^{241}\text{Am}/\text{Co}$ measurements, that were critically lacking signal. Anyway it has to be stressed, that the signal is always paid during these steps. And finally, someone may prefer to cut down background, whatever the price is.

And finally in the third step, the overall intensity of the magnetic fields is decreased, and the next iteration may proceed. The resulting $^{241}\text{Am}/\text{Co}$ line achieved after the first turn is shown in fig. 4.36. The second turn finished with the spectrum shown in fig. 4.37.

And the best result achieved after 5 iterations is shown in fig. 4.38 for the K-23.6 Co line. With the setup we scanned also a low energy region fig. 4.39 and a mid energy region in fig. 4.40 to show, how the broken adiabacity scales with energy.

4.3.4 Ar etching of a Co foil

The non adiabatic studies were interrupted by Ar etching, because except for high background, the $^{241}\text{Am}/\text{Co}$ source lacks the signal. The only hope, can be in cleaning the surface of the foil to get rid of contamination and Co oxides in favor of the metal component. Beside this, Ar etching produces a well defined surface

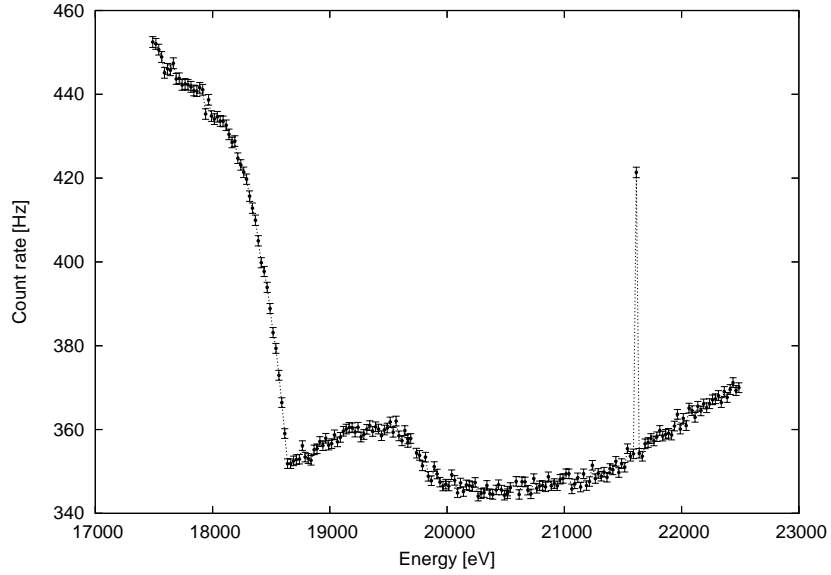


Figure 4.36 Adiabacity tuned for the first time. A $^{241}\text{Am}/\text{Co}$ scan is shown as measured by the Mainz spectrometer in a nonadiabatic mode. Compared to the adiabatic mode, the background is five times lower. The energy regions where the background electrons come from are indentified.

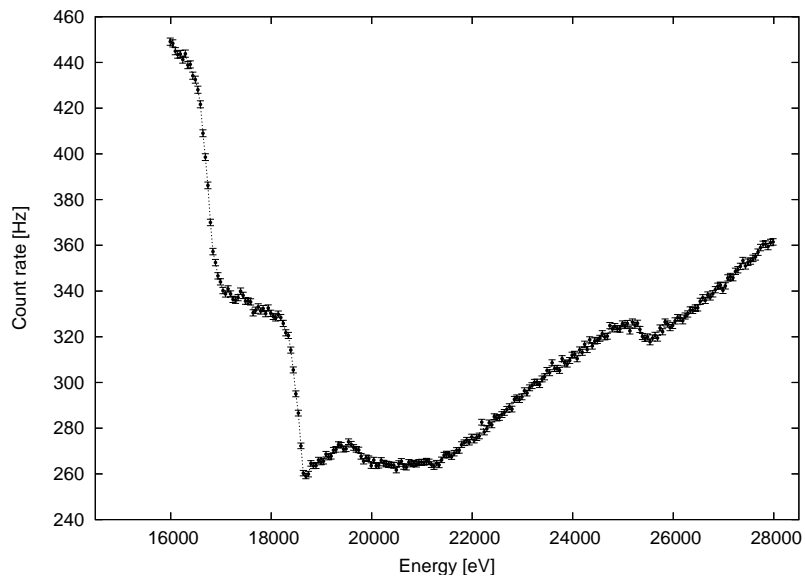


Figure 4.37 Adiabacity tuned for the second time. A $^{241}\text{Am}/\text{Co}$ scan in the region of interest is shown. The background was successfully decreased even more.

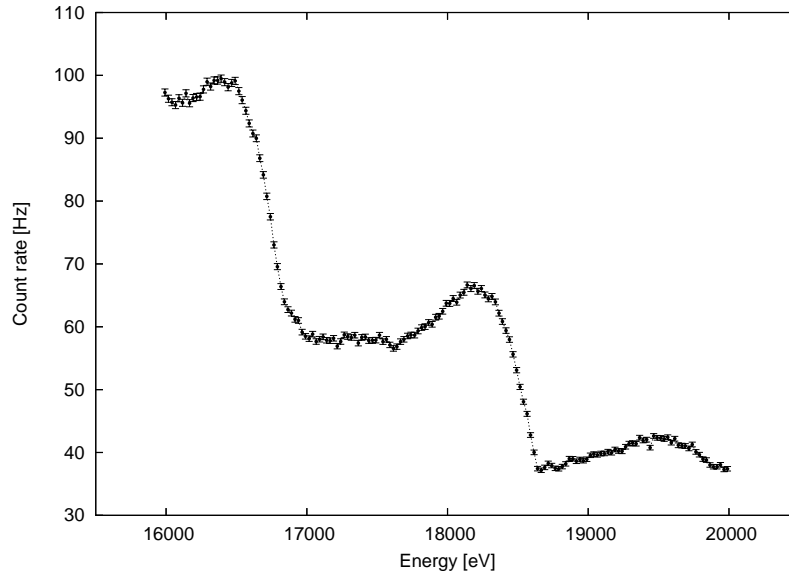


Figure 4.38 A wide scan of the $^{241}\text{Am}/\text{Co}$ K-26.3 line measured with the $3\ \mu\text{m}$ Co foil by the Mainz spectrometer in the tuned nonadiabatic mode. The overall background level was decreased by the factor of 50 if compared to the adiabatic mode.

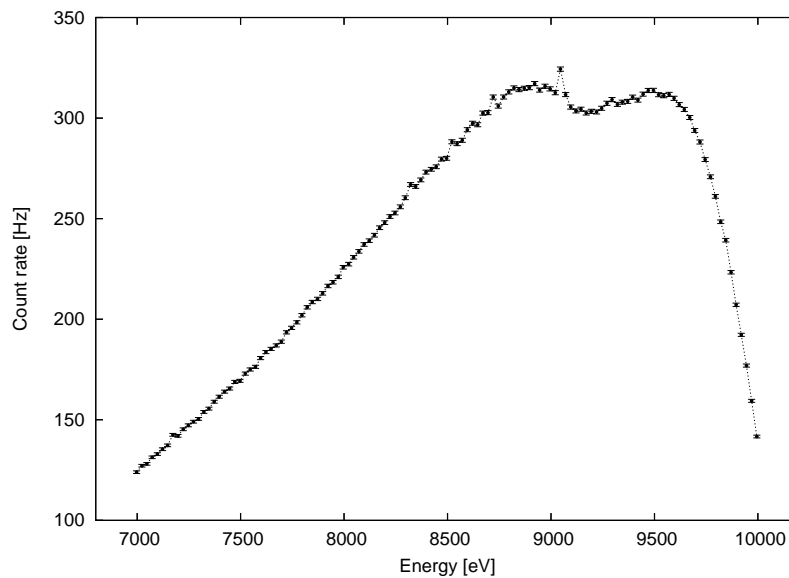


Figure 4.39 A low energy area of a $^{241}\text{Am}/\text{Co}$ spectrum measured by the Mainz spectrometer with the tuned adiabaticity. These low energy scans provide a valuable comparison to electron spectra recorded by the ESA 12 electrostatic spectrometer at Rez.

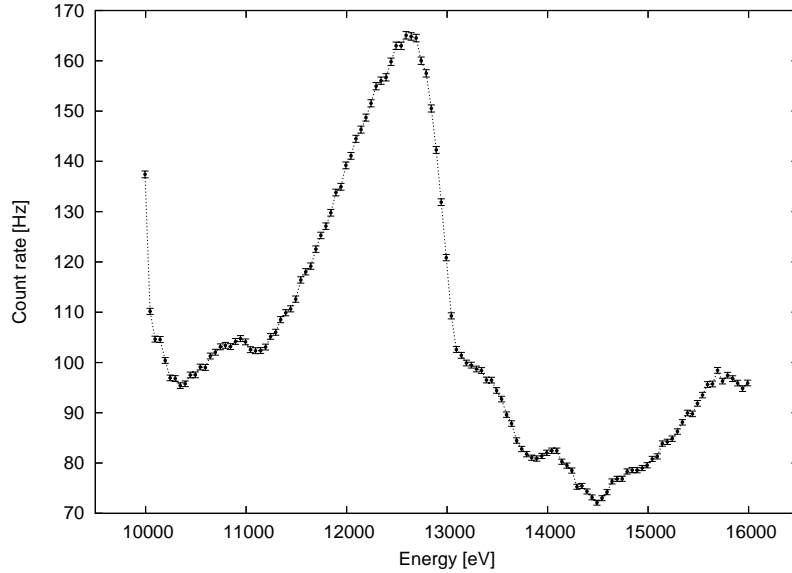


Figure 4.40 Another low energy area of a $^{241}\text{Am}/\text{Co}$ spectrum measured by the Mainz spectrometer with the tuned adiabacity.

in a reproducible way. The $0.1\ \mu\text{m}$ Co foil used up to this moment can not be sputtered because of the Mylar backing. So, it was replaced by the $3\ \mu\text{m}$ one.

The mechanical setup was changed to guarantee required pumping speed at the place of Ar etching (fig. 4.41). Contrary to recommendations, the required anode and cathode current settings, as well as the neutralization current settings had to be used about twice as large to initialize discharge. After the discharge had started, the anode voltage was increased to the maximum value of 170 V, and the anode current to the maximal value of 1 A. These values were kept during all the sputtering. The neutralization current was adjusted to $-0.130\ \text{A}$. These settings resulted in the cathode current of 12.5 A and the emission current of 1.13 A consuming about 7.2 sccm of Ar.

28 min after the initial discharge the dim surface was getting shiny, with half the surface shiny in 37 min. About 3/4 of the surface were shiny in 51 min. The last two small dim island of surface persisted even 60 min after the initial discharge, when the process was finished.

Estimating the current of Ar ions with the energy 100 eV through the coil to $100\ \mu\text{A}/\text{cm}^2$, the incident angle to 45° , and assuming 0.09 sputtered Co atoms per incident ion, 0.26 nm of Co were removed each minute. So, the total layer of 16 nm was removed in 60 min, which is equal to a free mean path of an 18 keV electron in Co. If the top layer was Co oxides, then the etched depth was significantly larger.

Accidentally, the ceramic insulator between the source cup and the support tube got coated with stainless steel, because the Ar beam was broader then the cup

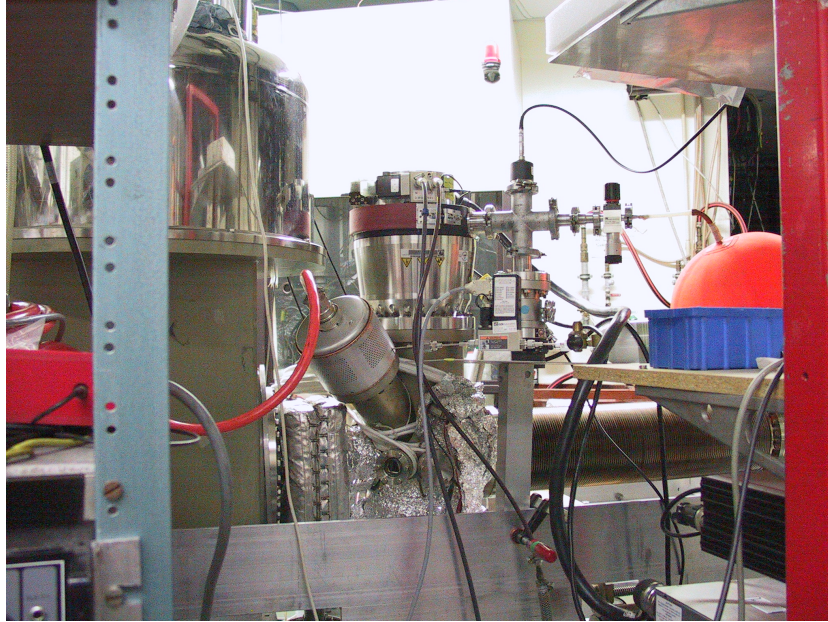


Figure 4.41 A modified setup of the source part of the Mainz spectrometer for Ar etching. The big 1500 l/s turbo was moved as close to the Ar etching head as possible to guarantee the required pumping speed.

diameter. From the side of the etching head the insulator was fully coated (see fig. 4.1), from the other site, the coating was partial only (fig. 4.42). The coating was so hard to remove, that we failed.

The comparison of both the etched spectrum and the reference one, recorded just before the sputtering is shown in fig. 4.43. We used slightly more adiabatic setting, because of better reproducibility, and also the higher magnetic fields in spectrometer magnets were impossible to reach due to the position of the turbo pump. Anyway, the message is clear: the Ar etching improved the sharpness of the effect, decreased background, and failed to enhance the effect.

4.3.5 Nonadiabatic mode of the Mainz spectrometer

Coming back to tuning adiabacity, two more turns were performed resulting in the magnet A and B currents of 20 A (2.4 T), the air coil current of -3.5 A (the magnetic field of 1.8–1.4 G, the energy resolution of 1.4–1.1 eV), and the detector magnet C current of 6 A (0.17 T). The best spectrum measured is in fig. 4.44.



Figure 4.42 An insulator to separate the cup with the $^{241}\text{Am}/\text{Co}$ source and the guiding tube. It was partially coated with steel during the Ar etching of the Co foil. The setup should be improved to avoid such coating.

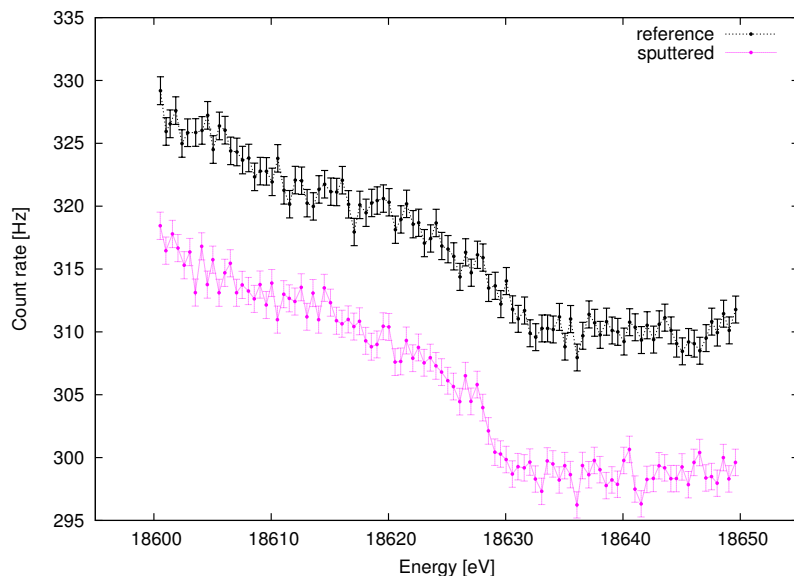


Figure 4.43 Comparison of the etched spectrum in magenta and the reference one prior etching in black.

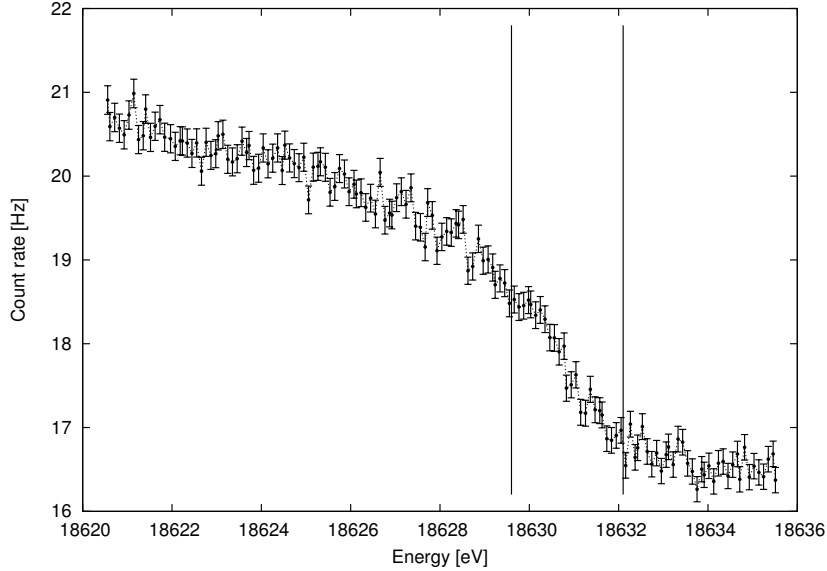


Figure 4.44 The $^{241}\text{Am}/\text{Co}$ K-26.3 line measured with the $3\ \mu\text{m}$ Co foil and with the tuned adiabaticity.

4.3.6 Conclusions of the Mainz $^{241}\text{Am}/\text{Co}$ measurements

To conclude, the $^{241}\text{Am}/\text{Co}$ source proved to be a good and stable source to monitor the energy scale of the KATRIN experiment. 300 electrons per sec of the K-26.3 keV line correspond to expectation (taking into account the source geometry), but only 6 of them leave the Co foil with no energy loss. This is the main disappointment, typically about 20% are the zero energy-loss ones³. Out of the 6 electrons we saved 2, paying 4 of them to cut down the background by factor 100.

The feasibility test seems to be completed. With the measured signal, the 50 meV limit of the energy scale stability would be reached in 22 days.

Lack of effect is the main disadvantage of the $^{241}\text{Am}/\text{Co}$ concept. And there is no apparent way, how to increase the effect, because number of gammas is limited by self-absorption. TOF-mode would in principle help to improve the signal to noise ratio, about 22 days would be required anyway.

³ There is 14 keV transition in ^{57}Co to ^{57}Fe decay. The number of zero energy-loss electrons emitted due to inner conversion is significantly lower than expected, and the energy loss spectrum is hard to explain in the MC way. Both the effects can be cured, if an extra interaction of the emitted electron with the whole atomic electrons is assumed—shake-off effect [31]

As for the outlook, the $^{241}\text{Am}/\text{Co}$ electron line of interest is above the tritium endpoint, therefore the $^{241}\text{Am}/\text{Co}$ photoelectrons have to be slow down by applying positive voltage to the source of about 200 V. Such voltage would accelerate positive ions towards the spectrometer. That could contribute to background. We would expect little or no contribution with respect to the voltage value. Anyway, this has not been tested.

4.4 Voltage stability & divider calibration in NPI Rez

In this section, a short time behaviour of metrologic voltmeters and a high quality divider is shown. These instruments perform excellently in superb conditions of metrological laboratories, where their precision and stability is guaranteed. Practically, it is hard to achieve such conditions in real physics laboratories. Consequently, the instruments may exhibit unexpected drifts and/or jumps. Hopefully, the section will emphasize the role of the monitor spectrometer, and will result in some degree of redundancy in electrical equipment of the monitor spectrometer, especially with respect to the total measurement time of five calendar years.

Measurements were performed with a Fluke 8508A multimeter and its direct predecessor a Solartron 7051 multimeter, and a precision high voltage divider developed in our institute [36] exhibiting a long-term drift of 0.6 ppm/week (from February to November 2007, the dividing ratio was checked about three times per month). First, a comparison of -150 V is shown in fig. 4.45. The voltage was produced by a FUG MCP 650 V power supply, which was loaded appropriately. The voltage difference recorded by the voltmeters changed by 2 ppm within a half an hour. A fit of distribution of the voltage differences results with significantly high $\chi^2/\text{d.o.f.}$ No other indication for such behavior was observed than the raised χ^2 value.

Then, a comparison of 650 V is shown in fig. 4.46. The voltage usually used to calibrate the high voltage divider was produced again by the FUG MCP power supply, with the high voltage divider as a load. A fluctuation of about 2 ppm was observed within ten minutes. The fluctuation was indicated by a lowered correlation coefficient of the voltages. A distribution fit of the voltage differences was useless in this case.

And finally, divider ratio disturbances are shown in fig. 4.47 and fig. 4.48. The first one represents a sine like fluctuation of 1.5 ppm in twenty minutes. The latter one is an example of a divider ratio jump of about 2 ppm. Both disturbances were indicated by unusual values of appropriate correlation coefficients.

All these values are within one year limits of the multimeters. Anyway, these effects introduce systematics into measurements, they are hard to explain, hard to detect, and even harder to beat. We did not expect such effects in our measurements. I learned to use all available consistency checks of the measurements, and proceed with maximum redundancy possible.

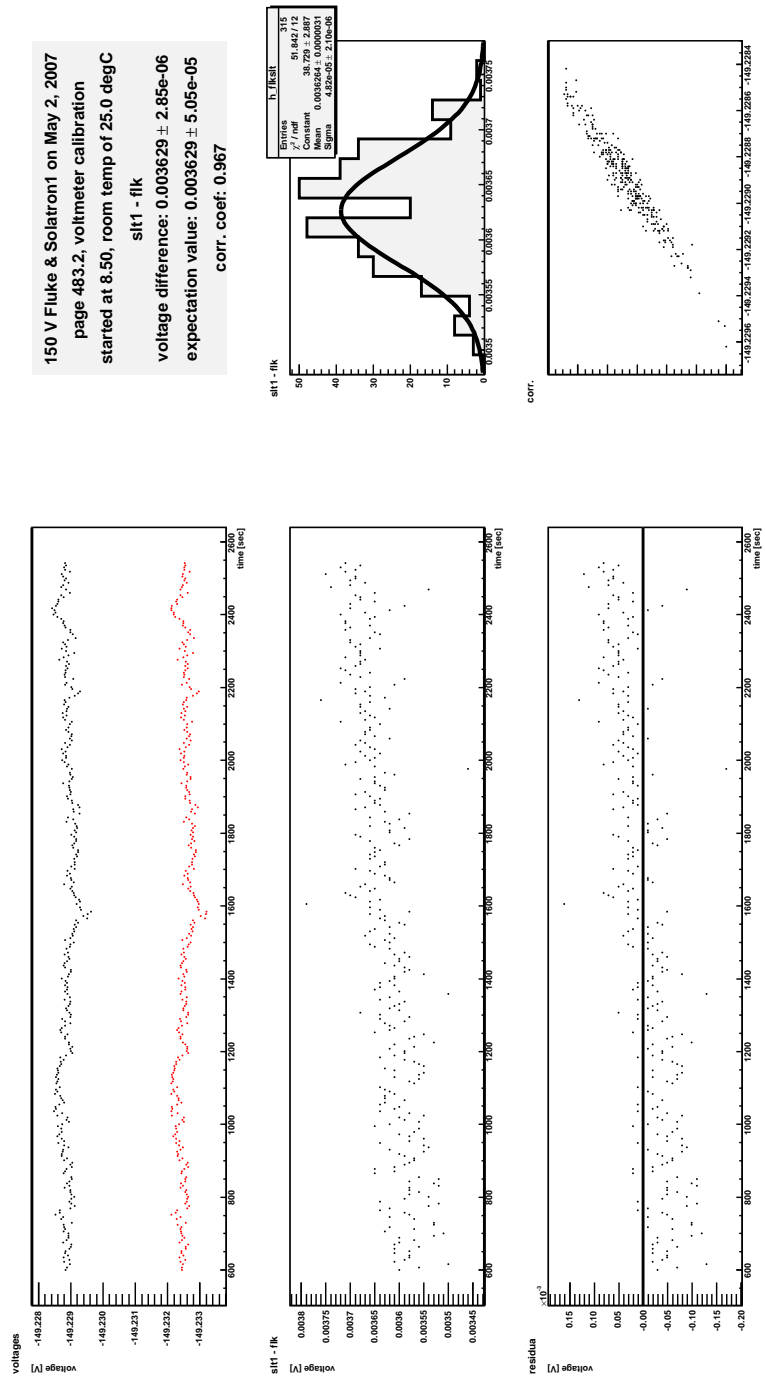


Figure 4.45 A comparison of -150 V by the Fluke and Solaatron voltmeters.

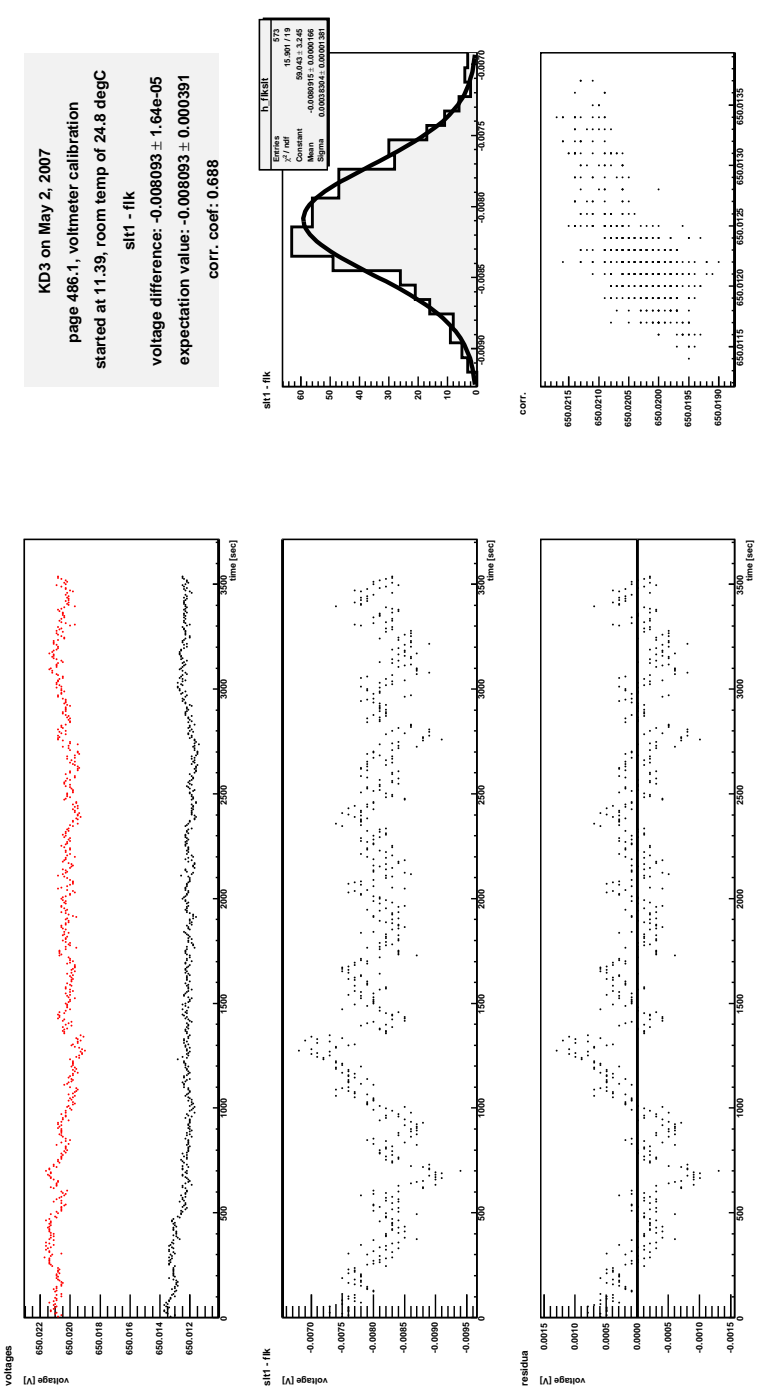


Figure 4.46 A comparison of 650 V by the Fluke and Solartron voltmeters.

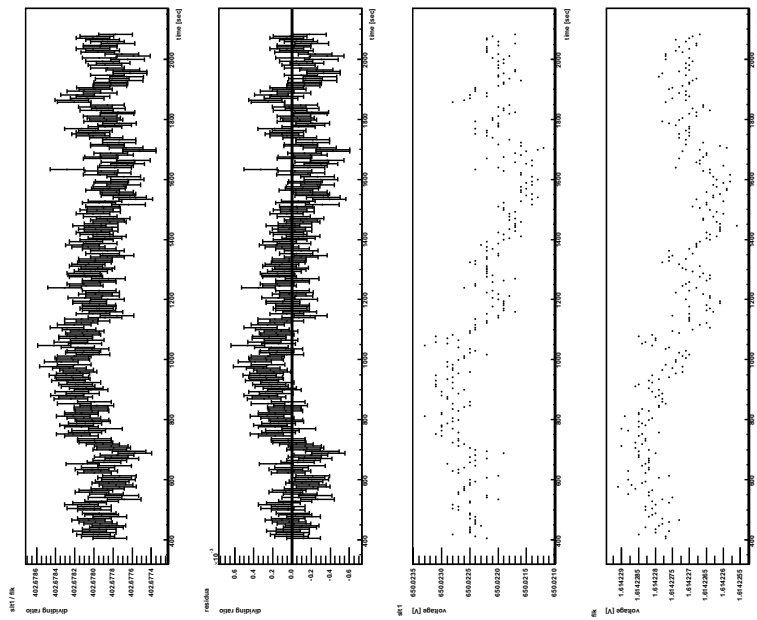
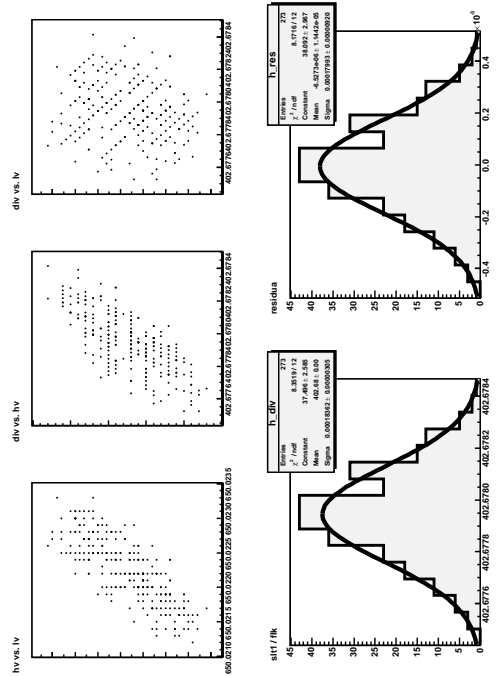
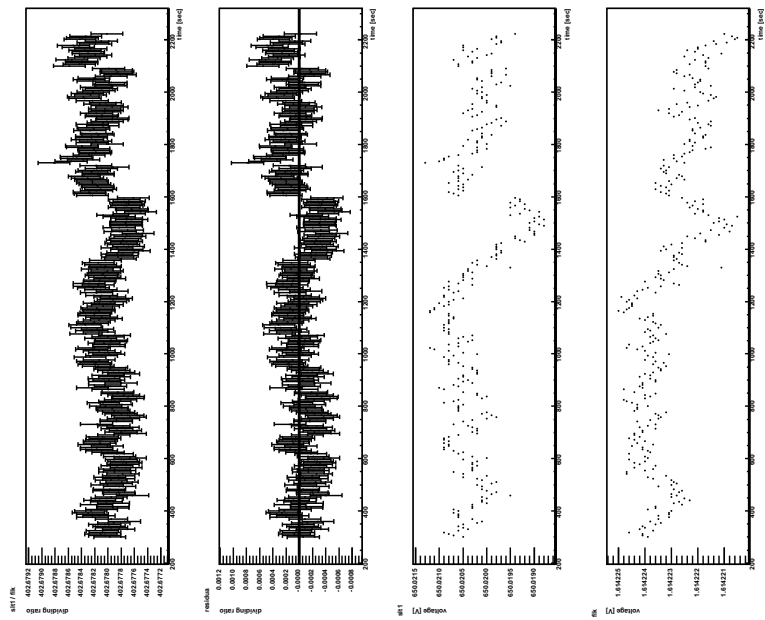


Figure 4.47 A drift of dividing ratio measured by the Fluke and Solartron voltmeters.

KD3 on May 2, 2007
 page 485.2, div ratio indirect comparison: KD3 8kV/20V & flk
 started at 11.03, room: 25.0 degC, divider: 25.2 degC
 silt1 / flk
 div ratio (pure stat): $402.67795 \pm 1e-05$
 div ratio (syst & fit): $402.67795 \pm 1.1e-05$
 div ratio fit ch2 / dof: 261.374 / 271
 hv vs. lv: 0.802, div vs. hv: 0.733, div vs. lv: 0.182





KD3 on May 2, 2007
 page 487.2, div ratio indirect comparison: KD3 8kV/20V & flk
 started at 11.39, room: 24.8 degC, divider: 25.3 degC
 sit1 / flk
 div ratio (pure stat): $402.67803 \pm 1.2e-05$
 div ratio (syst & fit): $402.67803 \pm 1.4e-05$
 div ratio fit ch2 / dof: 249.234 / 310
 hv vs. lv: 0.727, div vs. hv: 0.581, div vs. lv: -0.137

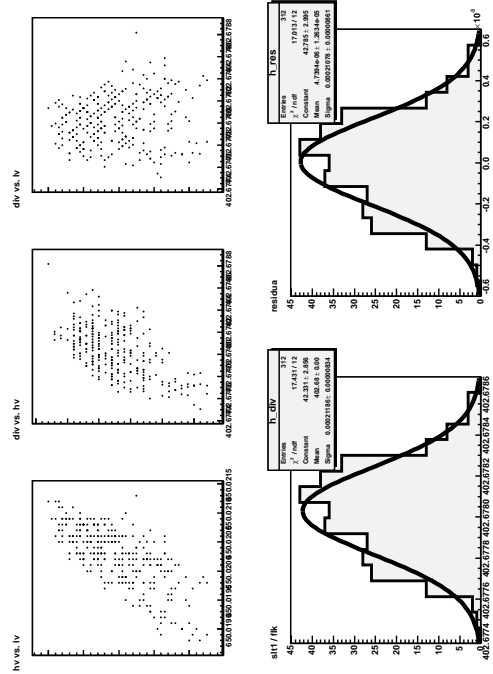


Figure 4.48 A drift of dividing ratio measured by the Fluke and Solartron voltmeters.

4.5 Long term stability of the ESA 12 electrostatic spectrometer

This is an outlook section on the ESA 12 spectrometer at Řež, followed by a general method to monitor an energy scale uniting both the electrical and spectroscopic methods. Strategy to suppress influence of HV dividing ratio change on a position of electron lines is given. A method to check stability of electron line position down to several tens of meV exploiting the retarding mode of ESA12 is proposed.

Checking long term stability of electron lines, we are usually not interested in the absolute line position itself. Just a change of the line position matters. A strategy based on measurements with a retarding mode of ESA12 spectrometer and several passing energies is offered. In the initial measurements we get a line position and a dividing ratio value. Later, the line position value is compared to measurements assuming both a changed dividing ratio value and a biased line position (e.g. due to instabilities of the source itself).

The ESA 12 is a double pass cylindrical spectrometer with a retardation lens. Applying a retarding voltage U to the retardation lens, the retarded energy of eU is subtracted from the original kinetic energy of the electron. If the passing voltage U is applied to the cylindrical part of the spectrometer, the electrons with the kinetic energy of $eU/0.56$ may pass the spectrometer. In so called “retardation mode” of the spectrometer, a typical value of the passing voltage is below 200 V, while the retarding voltage can reach up to 8 kV.

Energy resolution ΔE (FWHM) of the ESA 12 spectrometer is driven by the passing energy of the spectrometer: $\Delta E = 0.011 \times E_{\text{pass}}$. And any retardation cuts down the transmission significantly. The method does not assume long term stability of voltmeters and a high voltage divider. But we require long term stability of the passing energy in the retarding mode of ESA12.

4.5.1 Principles of the method

The method is aiming to disentangle a change of HV divider ration and a drift of a source. The method is based on two features of the ESA 12 spectrometer:

- a given energy of studied electrons can be produced by various combinations of retarding and passing energies
- a sum of the various retarding and passing energies is different from each other thanks to the factor of 0.56 scaling a passing energy to a passing voltage

First, an initial measurement is taken. Later, another measurement is performed to be compared with the initial one.

4.5.2 The initial measurements

The aim of the section is to achieve a value of the electron line position. The value may be in no relation to the absolute (true) line position. In later measurements, we will compare measured line positions with this one. In the following, the present ESA 12 setup is assumed as described in the preceding paragraphs. Further, we assume that during the initial measurement all the electric devices are stable.

4.5.2.1 Line position

Let us have two measurements of the same electron line with retarding mode with two various passing energies $E_{1,2}^{\text{pass}}$.

$$\begin{aligned} E_1^{(1)} &= k_0 e U_1^{\text{vol}} + E_1^{\text{pass}} \\ E_2^{(1)} &= k_0 e U_2^{\text{vol}} + E_2^{\text{pass}} \quad , \end{aligned} \quad (4.1)$$

where $E_{1,2}^{(1)}$ are the evaluated line positions, $U_{1,2}^{\text{vol}}$ are the corresponding voltages as recorded by the voltmeter, and k_0 is the HV dividing ratio unknown and fixed to an arbitrary value (e.g. the last calibration one). Then, subtracting both the equations (4.1) we can express the k_0 value as

$$k_0 = \frac{(E_1^{(1)} - E_2^{(1)}) - (E_1^{\text{pass}} - E_2^{\text{pass}})}{eU_1^{\text{vol}} - eU_2^{\text{vol}}} \quad . \quad (4.2)$$

A wrong k_0 value is the only reason for a possible difference between $E_1^{(1)}$ and $E_2^{(1)}$. (U^{vol} is not a reason, see comments later.) Thus, better choice of dividing ratio is possible, to make both $E_1^{(1)}$ and $E_2^{(1)}$ equal. Let us set the dividing ratio to the value of k_1 so that

$$E_1^{(1)} = E_2^{(1)} = E^{(1)} \quad . \quad (4.3)$$

With respect to eq. (4.2), the proper choice of the dividing ratio value is

$$k_1 = \frac{E_2^{\text{pass}} - E_1^{\text{pass}}}{eU_1^{\text{vol}} - eU_2^{\text{vol}}} \quad . \quad (4.4)$$

The k_1 value may be in no relation to the true (calibrated) dividing ratio value. It is just a parameter, that we chose to bind voltage to the energy scales. We do not describe a method to determine an absolute value of the dividing ratio, because

both the calibration of the divider and the calibration of the voltmeter contribute to the k_1 value. Anyway, a calibration value for a divider-voltmeter tandem can be determined in the region of interest and with the load used.

4.5.2.2 Uncertainty of HV dividing ratio

With respect to (4.2), the standard deviation σ_k of the dividing ratio k_1 can be derived as

$$\sigma_k^2 = \frac{2}{(eU_1^{\text{vol}} - eU_2^{\text{vol}})^2} (\sigma_E^2 + \sigma_{E_{\text{pass}}}^2 + k_0^2 \sigma_{U^{\text{vol}}}^2) \quad , \quad (4.5)$$

where σ_E is the standard deviation of the evaluated line positions (assuming both the uncertainties of $E_1^{(1)}$ and $E_2^{(2)}$ are about the same), $\sigma_{E_{\text{pass}}}$ is the standard deviation of both the passing energies $E_{1,2}^{\text{pass}}$ (the same assumption), and finally $\sigma_{U^{\text{vol}}}$ stands for the standard deviation of both the voltages $U_{1,2}^{\text{vol}}$ (the same assumption again).

As for numerical values let us assume two setups starting with about $E^{(1)} \sim 7000$ eV, $k_1 \sim 500$, and $\sigma_{E_{\text{pass}}} \sim 10^{-3}$ eV:

- a *realistic* one with $\sigma_E \sim 3$ meV, $\sigma_{U^{\text{vol}}} \sim 2 \times 10^{-6}$ V, $U_2^{\text{vol}} - U_1^{\text{vol}} \sim 0.6$ V ($E_1^{\text{pass}} - E_2^{\text{pass}} \sim 300$ eV) resulting in $\sigma_k \sim 7.5 \times 10^{-3}$, e.i. $\sigma_k/k_1 \sim 15$ ppm
- a rather *optimistic* one with $\sigma_E \sim 1$ meV, $\sigma_{U^{\text{vol}}} \sim 1 \times 10^{-6}$ V, $U_2^{\text{vol}} - U_1^{\text{vol}} \sim 0.6$ V ($E_1^{\text{pass}} - E_2^{\text{pass}} \sim 300$ eV) resulting in $\sigma_k \sim 3.5 \times 10^{-3}$, e.i. $\sigma_k/k_1 \sim 7$ ppm

4.5.2.3 Comments

- Practically, we can measure more than two line energies $E_1^{(1)}$ and $E_2^{(1)}$ for several passing energies and than fit the results with a constant k_1 to suppress a dependence on unattended systematic effects and to improve precision of the evaluated $E^{(1)}$.
- Methodically, measurements of $E_1^{(1)}$ and $E_2^{(1)}$ may be rotated several times, or an extra final measurement of $E_1^{(1)}$ can be made and to be statistically tested for good agreement.
- k_1 value in 4.2 is not sensitive for a zero bias (including voltmeter zero bias, work function of the source, divider zero bias, source position), because all the relevant quantities (voltages and energies) are present in subtraction of two their values.
- $\sigma_{E_{\text{pass}}} \sim 10^{-3}$ eV is a safe estimate within a specification of precision voltmeters. $\sigma_{E_{\text{pass}}}$ contributes to the dividing ratio uncertainty in the same way

as the uncertainty of the line position in the optimistic case. Anyway, it is the critical parameter for the method, because we are looking for a long term absolute stability of E^{pass} on that level. All the other uncertainties should be guaranteed with respect to the measurement time of the initial step only.

- In an ultra-optimistic case we could determine the divider ratio with the uncertainty of about 3.5 ppm, assuming $\sigma_E \sim 0.3 \text{ meV}$, $\sigma_{U^{\text{vol}}} \sim 3 \times 10^{-7} \text{ V}$, and $U_2^{\text{vol}} - U_1^{\text{vol}} \sim 0.8 \text{ V}$

4.5.3 Changed dividing ratio

The aim of the section is to gently introduce a change of dividing ratio and energy line position. One by one, in an independent way. Let us have a new measurement few months later. A changed dividing ratio is the only change that has happened in between the measurements. Let k_2 be a new unknown value of dividing ratio,

$$k_2 = k_1 (1 + \Delta_k) \quad , \quad (4.6)$$

where Δ_k is a change of dividing ratio (let us assume, that the change is small). Further, let us assume, that the line position $E^{(1)}$ has not changed. An electron energy E is recorded by the voltmeter as

$$eU^{\text{vol}} = \frac{E - E^{\text{pass}}}{k_2} \quad . \quad (4.7)$$

However, the unknown change of dividing ratio is not taken into account when recording energies. So, the corresponding evaluated line positions are

$$\begin{aligned} E_1^{(2)} &= k_1 \frac{E^{(1)} - E_1^{\text{pass}}}{k_2} + E_1^{\text{pass}} \\ E_2^{(2)} &= k_1 \frac{E^{(1)} - E_2^{\text{pass}}}{k_2} + E_2^{\text{pass}} \quad , \end{aligned} \quad (4.8)$$

where the $E_{1,2}^{\text{pass}}$ are the same passing energies as in the previous section. The change of the evaluated line position with respect to the initial value $E^{(1)}$ is

$$E^{(1)} - E_i^{(2)} = \Delta_k \left(E^{(1)} - E_i^{\text{pass}} \right) \quad , \quad i = 1, 2 \quad . \quad (4.9)$$

So, the shift of the evaluated line positions is proportional to the change of the dividing ratio. Also, the change can be expressed by subtracting both the equations (4.8)

$$\Delta_k = \frac{E_1^{(2)} - E_2^{(2)}}{E_1^{\text{pass}} - E_2^{\text{pass}}} \quad . \quad (4.10)$$

4.5.4 Changed line position

Let us have the same measurement, assuming that the dividing ratio k_1 has not changed, but with a changed line position $E^{(2)}$

$$E^{(2)} = E^{(1)} + \Delta_E \quad , \quad (4.11)$$

where Δ_E is a change of line position. Now, an electron energy E is recorded by the Solartron voltmeter as

$$eU^{\text{vol}} = \frac{E - E^{\text{pass}}}{k_1} \quad . \quad (4.12)$$

The corresponding evaluated line positions are

$$\begin{aligned} E_1^{(2)} &= k_1 \frac{E^{(2)} - E_1^{\text{pass}}}{k_1} + E_1^{\text{pass}} = E^{(2)} \\ E_2^{(2)} &= k_1 \frac{E^{(2)} - E_2^{\text{pass}}}{k_1} + E_2^{\text{pass}} = E^{(2)} \quad , \end{aligned} \quad (4.13)$$

The change of the evaluated line position with respect to the initial value $E^{(1)}$ is

$$E^{(1)} - E_i^{(2)} = E^{(1)} - E^{(2)} = -\Delta_E \quad . \quad (4.14)$$

As expected, both the lines are shifted by the Δ_E .

Both the changes modify the evaluated line position in different way. Thus, we can disentangle the effects. We are going to show it in the next section.

4.5.5 Stability of the line position

A measurement few month later is performed to check the energy stability of the radioactive source. Let us introduce both an unknown changed dividing ratio k_2 and an unknown changed line position $E^{(2)}$ with

$$\begin{aligned} k_2 &= k_1 (1 + \Delta_k) \\ E^{(2)} &= E^{(1)} + \Delta_E \end{aligned} \quad (4.15)$$

An arbitrary energy E is recorded by the voltmeter as

$$eU^{\text{vol}} = \frac{E - E^{\text{pass}}}{k_2} \quad . \quad (4.16)$$

However, the unknown change of dividing ratio is not taken into account when recording energies. So, the corresponding evaluated line positions are

$$\begin{aligned}
E_1^{(2)} &= k_1 \frac{E^{(2)} - E_1^{\text{pass}}}{k_2} + E_1^{\text{pass}} \\
E_2^{(2)} &= k_1 \frac{E^{(2)} - E_2^{\text{pass}}}{k_2} + E_2^{\text{pass}} \quad ,
\end{aligned} \tag{4.17}$$

and these two equations can be solved with respect to two unknowns Δ_k , and Δ_E .

4.5.5.1 Change of the dividing ratio

Subtracting both the equations (4.17) we can express Δ_k as

$$\Delta_k = \frac{E_1^{(2)} - E_2^{(2)}}{E_1^{\text{pass}} - E_2^{\text{pass}}} \quad . \tag{4.18}$$

A comparison to eq. (4.10)) shows that the result is perfectly the same, but the equations being subtracted a different! The corresponding uncertainty δ_{Δ_k} of the change Δ_k of dividing ratio is

$$\delta_{\Delta_k}^2 = \frac{2}{(E_1^{\text{pass}} - E_2^{\text{pass}})^2} (\sigma_E^2 + \Delta_k^2 \sigma_{E^{\text{pass}}}^2) \tag{4.19}$$

As for the typical numerical values, let us assume $E_1^{(2)} - E_2^{(2)}$ about 50 meV. Then the δ_{Δ_k} value is dominated by the σ_E value ($\Delta_k = 1.7 \times 10^{-4}$), resulting in about $\delta_{\Delta_k} = 1.4 \times 10^{-5}$ in the realistic case, and $\delta_{\Delta_k} = 4.7 \times 10^{-6}$ in the optimistic case.

4.5.5.2 Change of the line position

Finally, the change Δ_E of the line position $E^{(2)}$ can be derived from the eq. (4.17)

$$\Delta_E = E_i^{(2)} (1 + \Delta_k) - E^{(1)} - \Delta_k (1 + \Delta_k) E_i^{\text{pass}} \quad . \tag{4.20}$$

The uncertainty δ_{Δ_E} of the error Δ_E can be estimated as

$$\begin{aligned}
\delta_{\Delta_E}^2 &= (1 + \Delta_k)^2 \sigma_E^2 + \sigma_E^2 + [\Delta_k (1 - \Delta_k)]^2 \sigma_{E^{\text{pass}}}^2 + \\
&\quad + \left[E_i^{(2)} + (1 + 2\Delta_k) E_i^{\text{pass}} \right]^2 \delta_{\Delta_k}^2 \\
\delta_{\Delta_E}^2 &\sim 2\sigma_E^2 + \left(E^{(1)} \right)^2 \delta_{\Delta_k}^2 \quad .
\end{aligned} \tag{4.21}$$

So, the uncertainty δ_{Δ_E} is dominated by δ_{Δ_k} (in the energy range we are interested in). In the realistic case we come to $\delta_{\Delta_E} = 0.1$ eV, and in the optimistic case we finish with $\delta_{\Delta_E} = 0.03$ eV.

4.5.5.3 Comments

- The error of the dividing ratio includes the same error of the voltmeter. We can not disentangle a voltmeter drift from a drift of the HV divider.
- As for the role of k_1 and its uncertainty: we don't need that number at all. The argumentation is straightforward: Using just the divider ratio value of k_0 to record all the lines, we obtain four independent line positions $E_i^{(1)}$ and $E_i^{(2)}$. They represent four equations for the four independent parameters: the initial line position, the divider ratio, the change of the line position (the shift of the radioactive source), and the change of the divider ratio (divider drift). The solution exists.
- If we believe that the drift of the divider ratio is independent of the voltage and the load applied to the divider, we could use photoelectrons emitted by an Al X-ray tube or various Auger lines. Even more, all these electron sources may suffer from long term instabilities. So an extraordinary redundancy should be employed to report on dividing ratio using such electron sources. Standard deviation of the line position in range of few meV can be achieved.
- The method can be in principle enhanced by an idea of Auger electrons as an atomic voltage divider. The idea is to bind several electron lines to increase precision of the line we are interested in. In the other words: the present method is based on the fact that the line position recorded for different voltages has to be the same. This could be improved to: the distance of the various lines has to be the same for different voltages. Anyway, long term stability of these lines should be carefully cross checked. A similar effect can be achieved using various photoelectrons from various subshells.
- The method offered may be used in the other way round, i.e., if one is interested in the divider ratio shift, then the influence of a possible source shift may be suppressed exactly the same way we have already shown.

4.5.6 Examples

Two examples are shown to demonstrate the method. All the numbers about correspond to $^{83}\text{Rb}/^{83\text{m}}\text{Kr}$ L1-9.4 keV line. First, we show how a possible fictitious changes of divider ratio and source line position would affect measured line positions. Then, we show the opposite, i.e., starting with fictitious measured line position we show, what changes of divider ratio and source line position happened.

4.5.6.1 From instabilities to measured line positions

Let the initial line position be $E^{(1)} = 7000$ eV, the initial choice of the divider ratio $k_1 = 500$, the long-term error of the divider ratio $\Delta_k = 20$ ppm, and the long-term energy shift of the line position $\Delta_E = -100$ meV. Further, let us set the passing energies to $E_1^{\text{pass}} = 100$ eV and $E_2^{\text{pass}} = 400$ eV. When checking the line position, following mean values of the line positions will be recorded (eq. (4.17)):

$$E_1^{(2)} = 6999.762 \text{ eV} \quad E_2^{(2)} = 6999.768 \text{ eV} \quad . \quad (4.22)$$

4.5.6.2 From line positions to instabilities

Now, let us assume, we recorded the line positions $E_i^{(2)}$ as calculated in the previous step. Then, following eq. (4.18) and eq. (4.19) (in the optimistic case)

$$\Delta_k = 20.0 \pm 4.7 \text{ ppm} \quad . \quad (4.23)$$

And finally, following eq. (4.20) and eq. (4.21), the change of the line position is derived as (in the optimistic case):

$$\Delta_E = -100 \pm 33 \text{ meV} \quad . \quad (4.24)$$

4.5.7 Conclusions and outlook

A method to distinguish an energy shift of a radioactive source from drift of a high voltage divider is described deploying unique properties of the ESA12 spectrometer. Under realistic assumptions, the uncertainty of the change of the line position of $\delta_{\Delta E} = 0.1$ eV is achieved. In the case of optimistic assumptions, we come to $\delta_{\Delta E} = 0.03$ eV.

In place of an outlook, the method may be improved by

- development of a dedicated statistics to decide between two hypothesis: a stable one, and a biased one. Such a test could be more sensitive than evaluations of line positions and errors of dividing ratios.
- an active 1:2 high voltage divider consisting of two same resistors. The high voltage is applied to both of them and the high voltage applied to spectrometer is taken in parallel from one of them. Then the resistors are exchanged and the second one is used to supply the spectrometer.

From the sum of both the measurements with both the resistors we can decide on stability of the high voltage applied, because the sum is independent of 1:2 divider drift⁴. It does not sound practical, because twice as many measurements are required and twice as precise, which results in factor eight in time. Anyway, at half the voltage, spectrometers exhibit better resolution, and more intense lines are usually easier to obtain, and in the case of the ESA 12 spectrometer the losses due to retardation are significantly lower.

⁴ This is true, if the total resistance of the spectrometer to measure the monitoring line is constant during both the measurements.

5 Summary

The aim of the thesis was a feasibility study of a $^{241}\text{Am}/\text{Co}$ photoelectron source in the context of monitoring of the KATRIN experiment.

Theoretically, the feasibility study could proceed in an idealistic way; using a perfectly stable and precise electric equipment we develop standards of monoenergetic electrons, in particular the $^{241}\text{Am}/\text{Co}$ source. When the standards are ready we consider them stable further on, and use them to monitor the electric equipment. This is not realistic, definitely, because such the electric devices do not exist. In a more realistic way, both the electron standards and electric equipment are developed in parallel, cross-checking each other. And redundancy is crucial in this approach. This is the way I followed.

First, the status of neutrino physics was reviewed, stating that the KATRIN experiment was an important experiment to solve the neutrino mass puzzle. More, direct search for the neutrino mass is complementary to neutrinoless double beta decay and cosmology studies. The main advantage of the KATRIN approach is the model independence.

Further, an introduction to energy scale monitoring of the KATRIN experiment is presented to show that long-term stability on the metrological level is critical for a success of the KATRIN experiment. It is not possible to rely on electrical equipment only. Even more, redundancy is highly desirable. The concept of a monitor spectrometer was introduced, followed by a possible feedback from energy scale monitoring to the tritium data. Several monitoring (and calibration) sources of monoenergetic electrons are being developed in the KATRIN collaboration. Within the thesis, the $^{241}\text{Am}/\text{Co}$ photoelectron source was stressed.

Also in the chapter, the simulations that preceded the experiments at Mainz and Rez are covered. The first section presented a method to optimize the distribution of the total measurement time in single channel experiments, which is our case. Once the experimental setup was fixed, an additional freedom was left to choose a measurement points distribution, a measurement time distribution, and statistics to evaluate the experimental data. The method to optimize time distribution was introduced, and applied to KATRIN beta-spectra, looking in detail on minimal standart deviation of neutrino mass and the tritium endpoint. The method was fully explored in the appendix A. The first section was closed with challenges connected to mesurement point distribution.

Then, dedicated statistical test suitable to decide on stability of the $^{241}\text{Am}/\text{Co}$ line were introduced, based on tuned-up classical statistical test. The study started with the contribution of an energy scale bias to neutrino mass systematics, and continued with study what a reasonable measurement time of an $^{241}\text{Am}/\text{Co}$ line is, in order to monitor such a bias. The performance of a differential spectrometer and an integrating one was compared. The study was finished with the same tests applied on various lines emitted from a $^{83}\text{Rb}/^{83\text{m}}\text{Kr}$ source. A differential spectrometer is easier to understand compared to an integrating one, most probably because of a correlation of the line position and line width in the case of an integrating spectrometer. As expected, the line position itself is a good measure on line stability in the case of a differential spectrometer. Surprisingly, this statement is not true for an integrating spectrometer. At that case, all the test perform better than the position fit, with a test of normal distribution of residuals being the leader.

The theoretical chapter was concluded with a general framework of dedicated statistical tests best suited for a statistical problem specified in terms of a null and an alternative hypothesis.

The chapter on experiments was introduced by a $^{83}\text{Rb}/^{83\text{m}}\text{Kr}$ measurement with the Mainz spectrometer, proved that the spectrometer was the reliable monitor spectrometer operated with the energy resolution of 1.5 eV at 17.8 keV. Then the section of $^{241}\text{Am}/\text{Co}$ measurements with ESA12 differential spectrometer at Rez gave a preliminary tests on $^{241}\text{Am}/\text{Co}$ concept in energy regions reachable with this instrument. Measurements with resolution of 100 eV corresponded well to MC simulation. There was no free parameter in the MC simulation but background.

As for various Co foil comparison, the 5 μm , 3 μm , and 0.1 μm Co foil were tested with the thinnest one exhibiting the lowest background in general, and fast dropping low energy tails thanks to lower probability of electrons to loose energy within the Co layer. Unfortunately this foil was not bakeable, and could not be sputtered with Ar ions to clean the surface. So finally, the leading candidate for a Co convertor was the 3 μm Co foil as delivered.

In the main section on $^{241}\text{Am}/\text{Co}$ measurements at Mainz, I concluded, that the $^{241}\text{Am}/\text{Co}$ source proved to be a good source to monitor the energy scale of the KATRIN experiment. 300 electrons per sec of the K-23.6 keV line corresponded to expectation, but only 6 of them left the Co foil with no energy loss. This was the main disappointment, usually about 20% were the zero energy-loss ones. We tuned the spectrometer to operate in nonadiabatic mode to suppress the high background, unavoidably losing some effect as well. Out of the 6 electrons 2 were saved, paying 4 of them to cut down the background by the factor of 100.

With the measured signal, the 50 meV limit of the energy scale stability would be reached in 22 days. Lack of effect is the main disadvantage of the $^{241}\text{Am}/\text{Co}$ concept. And there is no apparent way, how to increase the effect, because number of gammas undergoing photoeffect is limited by self-absorption in ^{241}Am . TOF-mode would in principle help to improve the signal to noise ratio, about 22 days would be required anyway.

The rest on the experimental chapter was devoted to collecting experimental evidence on some subtle effects connected to monitoring. Starting with voltage stability and divider calibration at Rez, pointing to some short time behaviour of voltmeters and a high voltage divider in real laboratory conditions, showing some typical numerical evidences of the behaviour. Multiple background peaks observed in Mainz we covered in the appendix B. We concluded, that the process was driven by lack of adiabacity. True secondary electrons were suggested to take responsibility for the effect. A simulation mock-up of the process was offered. The simulation is limited by an unknown nonadiabatic process to bind the true secondary electrons on magnetic field lines guiding to the detector.

The thesis was concluded with an outlook section on long term stability in ESA12 spectrometer. A method to distinguish an energy shift of a radioactive source from drift of a high voltage divider was described deploying unique properties of the ESA12 electron spectrometer.

6 Conclusions

The thesis was devoted to the development of the $^{241}\text{Am}/\text{Co}$ photoelectron source in the context of the energy scale monitoring of the KATRIN neutrino experiment. It is impossible to develop a standard of monoenergetic electrons on a ppm level, and not to pay an attention to electrical devices involved in the experiment, and to statistical methods used to evaluate the measured data. I consider the main outputs of the thesis to be the following:

- dedicated statistical tests suitable to decide on stability of the $^{241}\text{Am}/\text{Co}$ line, based on tuned-up classical statistical test
- the first solid source $^{83}\text{Rb}/^{83\text{m}}\text{Kr}$ measurements at Mainz proving that the Mainz spectrometer can be reliably operated with the energy resolution of 1.5 eV at the energy region of 17.8 keV
- the $^{241}\text{Am}/\text{Co}$ feasibility test at Mainz showing that the $^{241}\text{Am}/\text{Co}$ source can monitor the energy scale of the KATRIN experiment
- a method to distinguish an energy shift of a radioactive source from drift of a high voltage divider in the ESA12 electron spectrometer.
- outlook on a general framework of dedicated statistical tests best suited for a physical problem specified in terms of a null and an alternative hypothesis

A Optimal measurement time and point distributions

In the section we cover the method introduced in section 3.3. The full application to the tritium beta spectrum is given. We believe it highlights where the information on the neutrino mass is given in the beta spectrum. To make the section self-supported, we repeat the method description.

Optimizing the setup of our experiment, we also need to distribute the measurement time into individual spectral points, i.e., to set the measurement time in each measurement point. This is done with respect to the physical quantity of interest, in particular, we would like to minimize the standard deviation of the selected fit parameter. The point is, we can not set all the measurement points in parallel (numerically not feasible). Instead, we can fix the measurement time in points one by one, approaching the optimal time distribution in an iterative way. To demonstrate the method, an application on the tritium beta spectrum, and the KATRIN setup is shown. It runs as follows:

Let E_i be a fixed distribution of measurement points, and τ_{tot} the total measurement time. Further, let T_i be the initial time distribution chosen ad hoc, resulting in the initial standard deviation of the neutrino mass $\sigma_{\text{init}} = \sigma(T_i)$ (the parameter of interest). Now, we minimize the standard deviation of the neutrino mass varying the time T_1 in the first point only, keeping the total measurement time equal to τ_{tot} , i.e., scaling the measurement times in the rest points by the same factor. As the result we obtain the time distribution t_i^1 and the corresponding standard deviation of the neutrino mass σ^1 . Then we do the same for all the other measurement points. So, we get n time distributions t_i^k , $k = 1 \dots n$ and sigmas σ^k .

The final time distribution T_i' is then given by the weighted sum

$$T_i' = \frac{1}{n} \sum_{k=1}^n \omega_k t_i^k \quad , \quad (\text{A.1})$$

where ω_k are the weight factors. Further, we offer the following method to estimate the weight factors by extrapolating the partial time distributions t_i^k according the partial standard deviations of the neutrino mass:

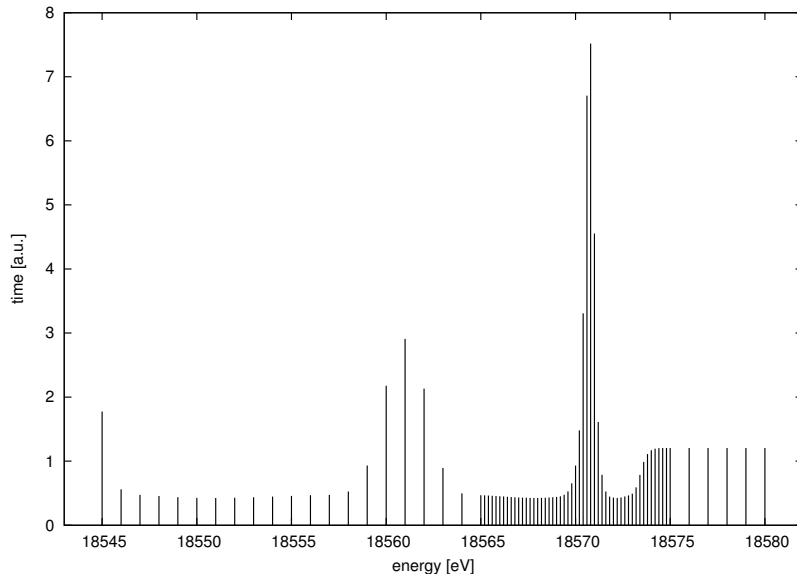


Figure A.1 An optimal time distribution with respect to the minimal standard deviation of the neutrino mass fitting four parameters: amplitude, background, the tritium endpoint, and the neutrino mass.

$$\omega_k = \left(\frac{\sigma_{\text{init}} - \sigma^k}{\frac{1}{n} \sum \sigma^k} \right)^s, \quad (\text{A.2})$$

where s is chosen to minimize $\sigma(T'_i)$. Finally we replace the initial time distribution T_i by T'_i and start a new iteration. Practically, we implement the method on grid. This choice of the weight factors speeds the iterative procedure significantly. However, it decreases the numerical stability as well. If the numerical stability is favored, then setting all the ω_k equal to one is a good choice.

The result is shown in fig. A.1. The standard deviation of the neutrino mass was improved by factor 0.85 compared to the uniform time distribution. The same improvement can be achieved by a prolongation of the total measurement time prolongation by factor of 1.9. A similar method may be used to minimize systematic effects. Fig. A.2 gives the time distribution optimized with respect to the endpoint value, keeping the neutrino mass value fixed and known.

We are going to illustrate how the most sensitive region with respect to the neutrino mass changes with background values. In fig. A.3 the optimal time distribution for background values of 1 mHz and 10 mHz are given. In fig. A.4 the optimal time distribution for background values of 30 mHz and 100 mHz are shown. It follows the theoretical pattern [37] corrected for the energy distribution of rotational-vibrational states.

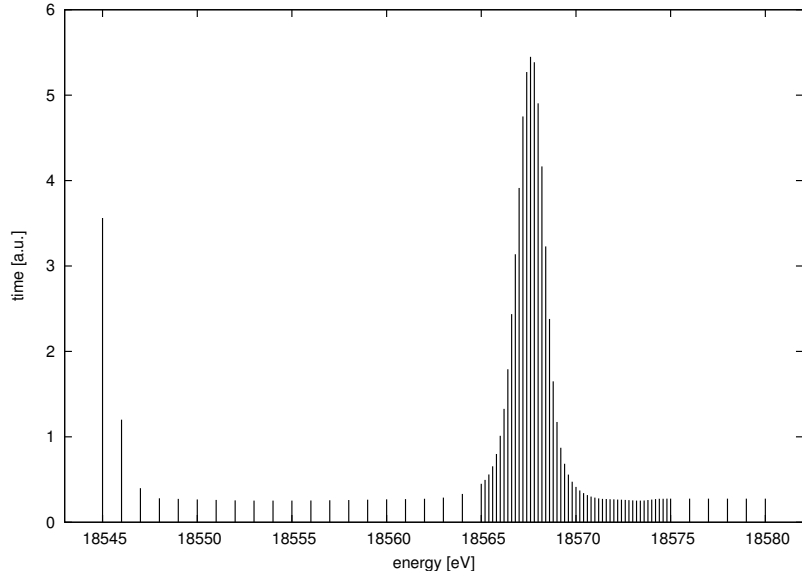


Figure A.2 An optimal time distribution with respect to the minimal deviation of the endpoint energy assuming a fixed and known neutrino mass, and fitting amplitude, background, and the endpoint energy.

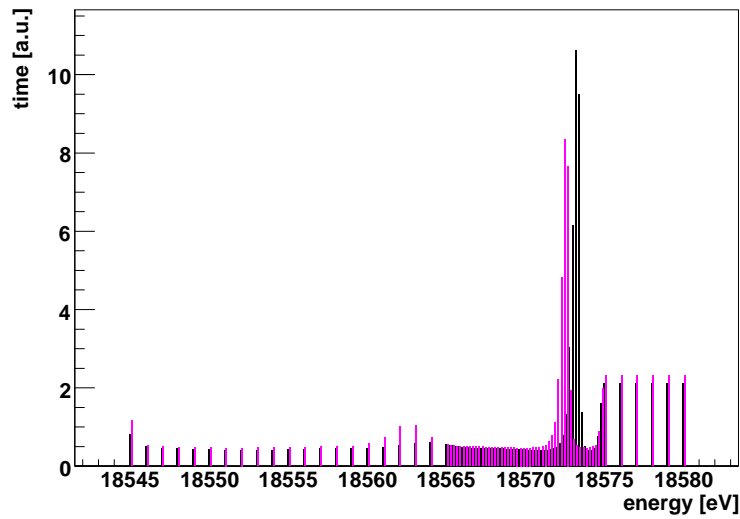


Figure A.3 An optimal time distribution with respect to the minimal neutrino mass deviation fitting all the four parameters. Comparison of 1 mHz background (in black), and 10 mHz background (in magenta).

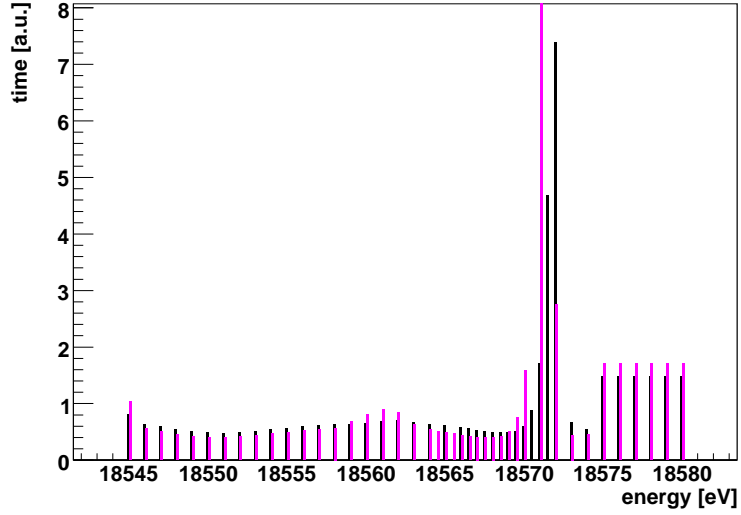


Figure A.4 An optimal time distribution with respect to the minimal neutrino mass deviation fitting all the four parameters. Comparison of 30 mHz background (in black), and 100 mHz background (in magenta).

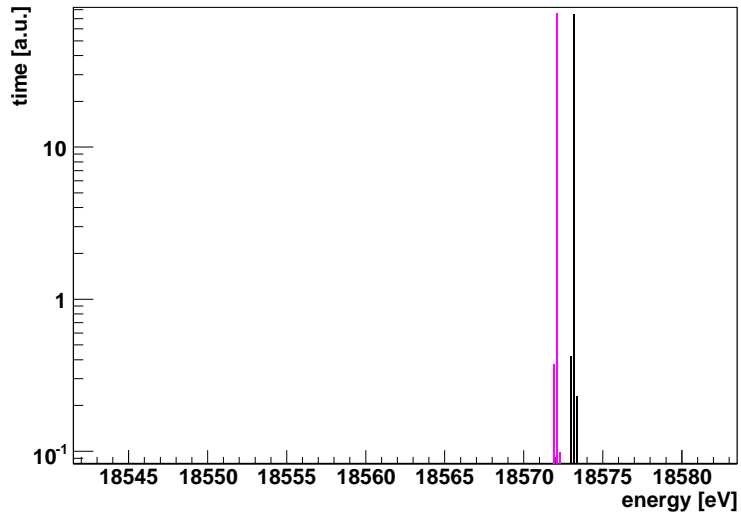


Figure A.5 An optimal time distribution with respect to the minimal neutrino mass deviation. All the parameters but the neutrino mass are fixed to the initial values. The black distribution relates to 1 mHz background, the magenta one to the 10 mHz background.

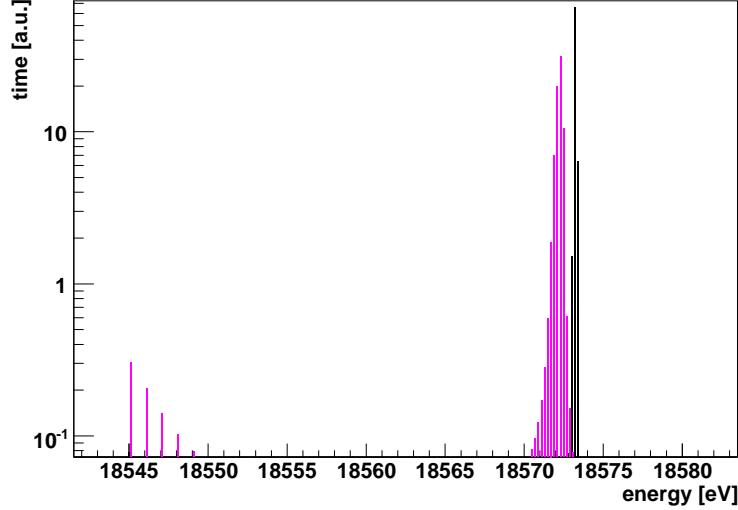


Figure A.6 A time distribution minimizing neutrino mass deviation fitting two parameters: amplitude, and the neutrino mass. Background and the tritium endpoint are kept fixed. The black distribution corresponds to 1 mHz background, the magenta one to 10 mHz background.

To elucidate the final shape of the time distribution, we performed several simulations fixing various parameters during the fits. First, we are going to fix all the parameters but the neutrino mass. Then, we will free the amplitude of the tritium beta spectrum, followed by a release of the background. Then, we will switch from neutrino mass to the endpoint of the beta spectrum. Fixing all the fit parameters but the endpoint, the time distribution will be optimized with respect to the standard deviation of the tritium endpoint. Then, keeping the focus on the tritium endpoint, the amplitude and the background will be freed. The endpoint and neutrino mass results will be compared. Finally, we will focus on the amplitude of the beta spectrum. Again, fixing all the fit parameters but the amplitude first, followed by a release of all the other fit parameters.

As for the neutrino mass, we started fixing all the fit parameters but the neutrino mass. The result is given in fig. A.5. Please note, that the sensitive area is narrower than the distribution of the rotational-vibrational states of the daughter molecule [12]. This requires further investigations. Then, we freed fit amplitude, keeping background and the tritium endpoint fixed. The result is shown in fig. A.6. And finally, background was freed as well, keeping the tritium endpoint the only parameter fixed. The result is given in fig. A.7.

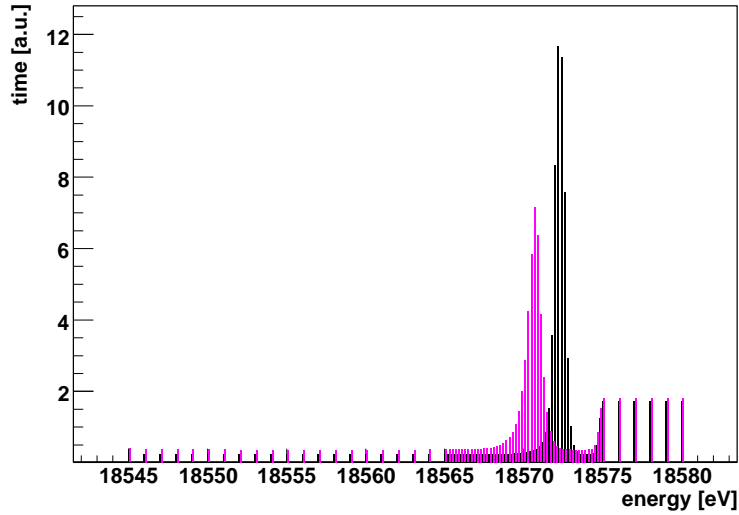


Figure A.7 An optimal time distribution with respect to the neutrino mass fixing the endpoint. The parameters fitted are: amplitude, background, and the neutrino mass. The black distribution relates to 1 mHz background, the magenta one to the 10 mHz background.

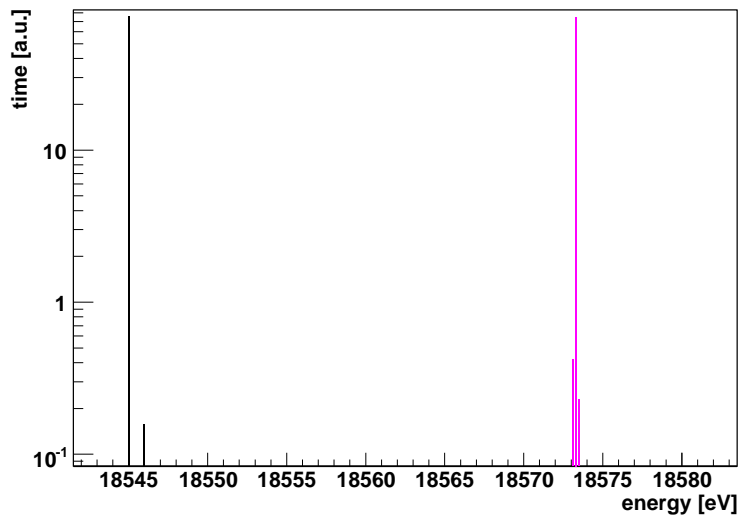


Figure A.8 In black, a time distribution minimizing the standard deviation of the tritium endpoint fixing all the fit parameters but the endpoint is given. In magenta, an optimal time distribution with respect to the neutrino mass fixing all the fit parameters but the neutrino mass is shown.

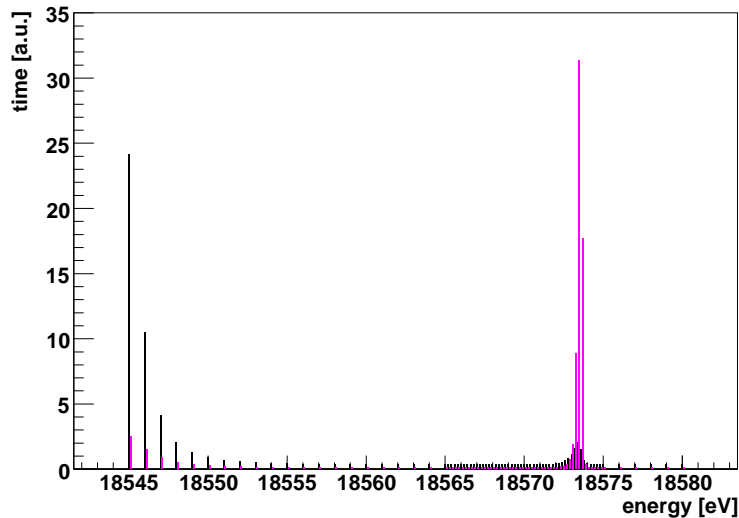


Figure A.9 In black, an optimal time distribution with respect to the minimal standard deviation of the endpoint is given fixing amplitude and background during the fit. In magenta, an optimal time distribution of the neutrino mass is shown fixing again amplitude and background.

Further, we investigated the optimal time distribution with respect to the minimal standard deviation of the tritium endpoint. Hopefully, it helps to understand the shape of the previous time distributions focused on the neutrino mass. In fig. A.8, a time distribution minimizing standard deviation of the endpoint is given, with the endpoint being the only fit parameter. This is compared to the time distribution minimizing neutrino mass standard deviation. In both cases, 1 mHz background value was used.

Then, we released the neutrino mass fit parameter (keeping amplitude and background fixed). The result is given in black in fig. A.9 to be compared to the time distribution focused on the neutrino mass (in magenta) fixing again amplitude and background. So, in both distributions the neutrino mass and the tritium endpoint are free fit parameters.

In fig. A.10 we compared: an optimal time distribution with respect to the tritium endpoint with the neutrino mass and background fixed in the fit (the endpoint and amplitude were free fit parameters), to an optimal time distribution focusing on the neutrino mass fixing the endpoint and background in the fit (keeping the neutrino mass and amplitude the free fit parameters).

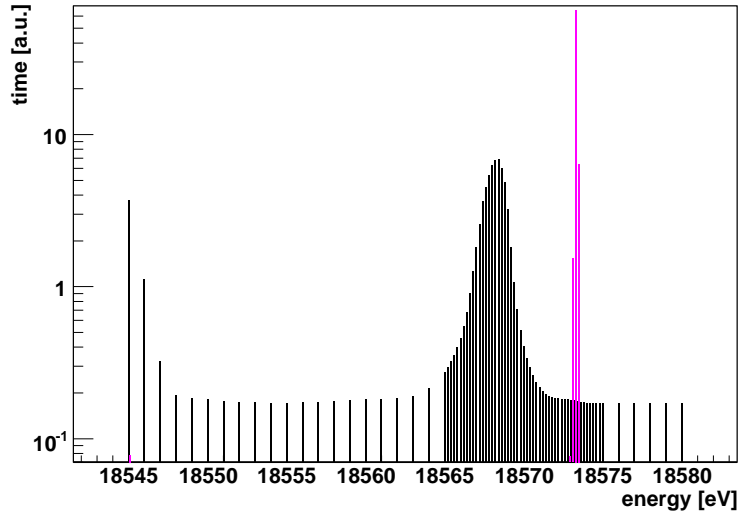


Figure A.10 In black, an optimal time distribution with respect to the standard deviation of the endpoint is given fixing the neutrino mass and background. In magenta, an optimal time distribution focused on the neutrino mass is shown fixing the endpoint and background.

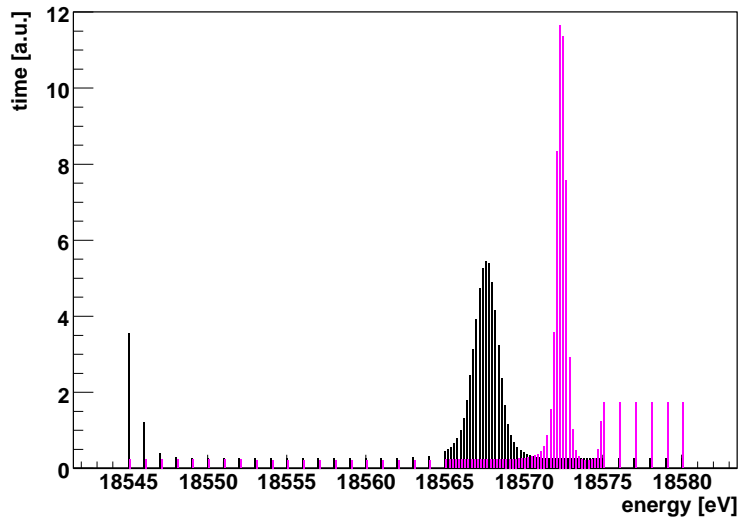


Figure A.11 In black, an optimal time distribution with respect to the standard deviation of the tritium endpoint is given fixing amplitude and background. In magenta, an optimal time distribution minimizing the standard deviation of the neutrino mass is shown fixing again the amplitude and the background.

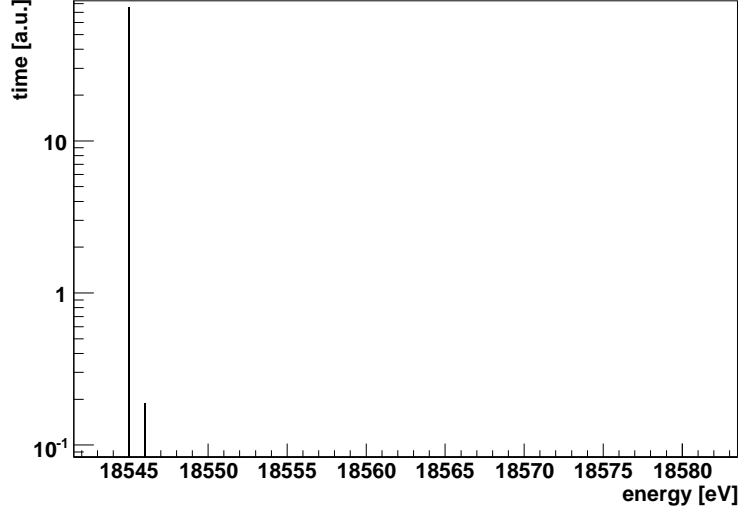


Figure A.12 An optimal time distribution with respect to the minimal standard deviation of the amplitude fixing all the parameters but the amplitude is shown.

To conclude the investigation of the tritium endpoint sensitivity, we found a time distribution minimizing the standard deviation of the tritium endpoint fixing the neutrino mass in the fit (keeping the endpoint, amplitude and background free). And we compared the result (in fig. A.11) to an optimal time distribution with respect to the neutrino mass with the endpoint fixed (the neutrino mass, amplitude, and background were free fit parameters). In all the previous cases, the background value of 1 mHz was assumed.

Relative amplitude of the theoretical spectrum fitted is the last interesting parameter to be possibly studied. So, in fig. A.12 we show the energetic region most sensitive on the amplitude keeping the amplitude the only free fit parameter (background, the endpoint, and the neutrino mass were fixed during the fit).

Then we released the neutrino mass (keeping the tritium endpoint and background fixed). In fig. A.13, we compared the result to an optimal time distribution focused on the neutrino mass also fixing the tritium endpoint and background. So, in both the cases amplitude and the neutrino mass were free fit parameters.

And finally, we fixed background and the neutrino mass, and compared optimal time distribution focused on amplitude and the endpoint (in fig. A.14). In all these studies, the initial background value of 1 mHz was assumed.

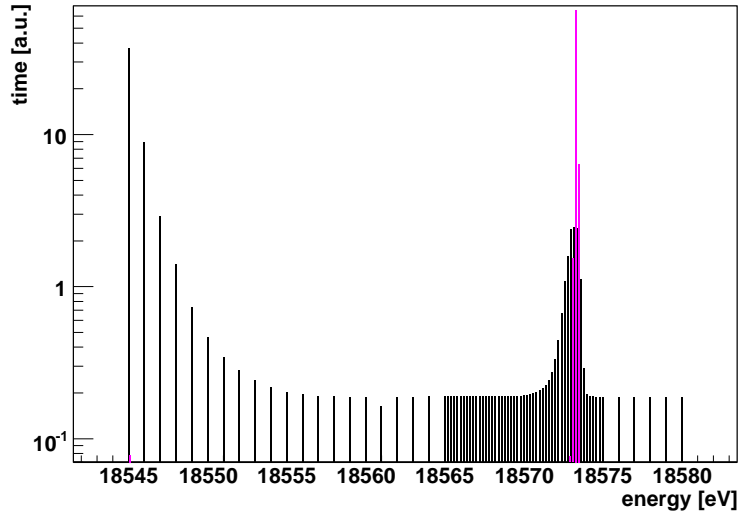


Figure A.13 In black, an optimal time distribution with respect to the minimal standard deviation of the amplitude is given fixing the tritium endpoint and background during the fit. In magenta, an optimal time distribution of the neutrino mass is shown also fixing the tritium endpoint and background.

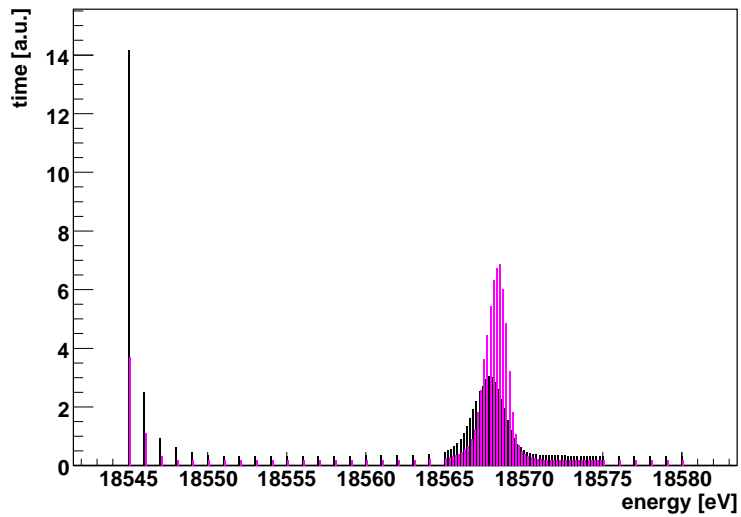


Figure A.14 In black, an optimal time distribution with respect to amplitude is given fixing the neutrino mass and background during the fit. In magenta, an optimal time distribution of the tritium endpoint is shown also fixing the neutrino mass and background.

To conclude the section, we would like to offer the logically reversed method as well. In principle, we can maximize the uncertainty of the quantity of interest with respect to the time distribution. Then, if the quantity is a systematic error, we can search for the measurement points sensitive to that error. These can be simply avoided in measurement, if not in a coincidence with the measurement region sensitive to the fit parameter of our interest.

B Multiple background peaks

B.1 Multiple background peaks at Mainz

In May, 2005, an effect of multiple background events was investigated at Mainz. The experimental results are covered in the section. True secondary electrons are suggested to be responsible for the effect. Our aim was to offer an experimental evidence of this subtle effect of the future monitor spectrometer, and not to answer all the questions raised.

B.2 Experimental evidence

The effect of multiple background events is an effect of several electrons with the retarded energy hitting the detector at the same moment.

The effect was observed by B. Flatt within his background studies when shooting the spectrometer with an X-ray tube [38]. N. Titov observed the effect as well studying background. During the tritium runs the effect was present when sweeping the electrodes with HV and mapping them directly to the detector [38]. On the other side, no evidence for the effect was found in the tritium data.

The example of the effect shown in fig. B.1 was obtained with the following spectrometer setup. Both the pinch magnets A and B were set to currents of $I_A = I_B = 20$ A generating relatively weak magnetic fields of about $B_A = B_B = 2.4$ T. The detector magnet C was set to field of about $B_C = 0.26$ T ($I_C = 9$ A) mapping field flux of 0.26 T cm² to the first segment of the detector (the very inner one of 1 cm²), 0.52 T cm² to both the first segment and the second one (2 cm²), and 0.77 T cm² to all the active segments of the detector (3 cm²). Fixing the air coil current to $I_{\text{air}} = -8$ A a magnetic field at the analyzing plane of -1.6 G was

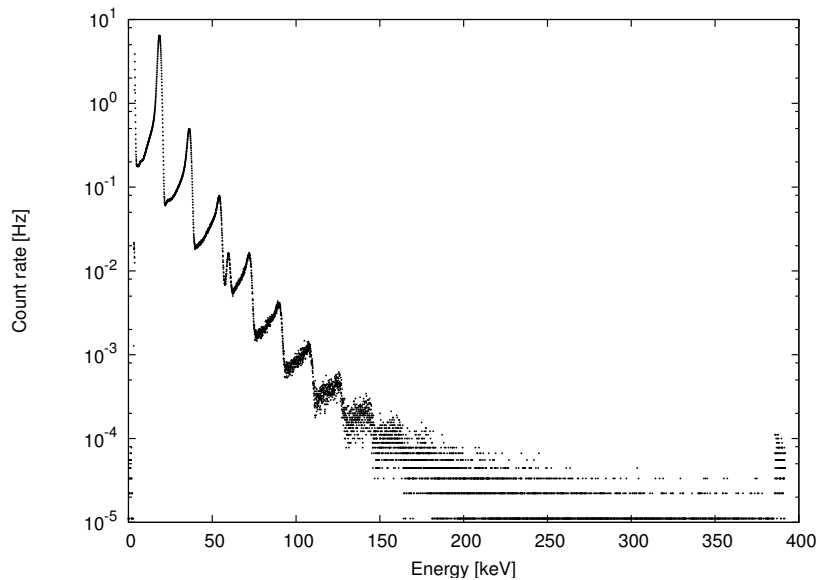


Figure B.1 An example of the multiple background events effect observed by the Mainz spectrometer. This is an effect of several electrons with retarded energy hitting the detector at the same moment. The spectrometer electrodes are directly mapped into the detector. Detector response of the first detector segment is shown.

obtained. So the electrodes were directly mapped to the detector. Retarding voltage of 18.6 keV was chosen. The Earth field compensation coils were set to +30 A (horizontal), and +10 A (vertical). A $^{241}\text{Am}/\text{Co}$ source (a 1.11 GBq Am source, and a $3\ \mu\text{m}$ Co foil) was placed inside the spectrometer magnet B (the source part of the spectrometer). The spectrometer tank was pumped down to pressure of 5×10^{-10} mbar (both the source valve and the detector valve opened). The detector was charged up to 40 V, and shaping time was set to $3\ \mu\text{s}$. The total measurement time was 90 000 s.

B.3 Understanding the effect

In the section, we would like to investigate what physical quantities the effect is dependent on.

B.3.1 Not an electronic effect

First, we would like to note that the effect is not caused by malicious electronics. The $^{241}\text{Am}/\text{Co}$ gammas with energy of 59.6 keV are never multiplied. For an example see fig. B.1.

B.3.2 An oscilloscope look

In the fig. B.2, the multiple events are shown as recorded by an oscilloscope connected in between the detector diode and the amplifiers. It proves the events to be real, but coming too fast to be separated by electronics. Various colors represent different segments of the detector. A huge coincidence between the detector segments is exhibited. The time periods between particular events are not completely random, but rather some multiples of about $1\ \mu\text{s}$, which is a typical time for very slow electrons to pass the spectrometer.

B.3.3 Independence of count rate

The independence of count rate is shown in fig. B.3. Pure spectrometer background was compared to a detector response with a $^{241}\text{Am}/\text{Co}$ source in the magnet B (the source side of the spectrometer). Both the spectra exhibited the same behavior.

A spectrometer setup with $I_A = I_B = 50\ \text{A}$ ($B_A = B_B = 6.0\ \text{T}$), $I_C = 30\ \text{A}$ ($B_C = 0.85\ \text{T}$), $I_{\text{air}} = -10\ \text{A}$ generating magnetic field at the analyzing plane of 4.0 G was used. In the case of the pure background measurement retarding voltage of 25.0 kV was chosen. In the case of measurement with the $^{241}\text{Am}/\text{Co}$ source retarding voltage of 18.2 kV was set. There is no particular reason for picking up different retarding voltages, this happened accidentally.

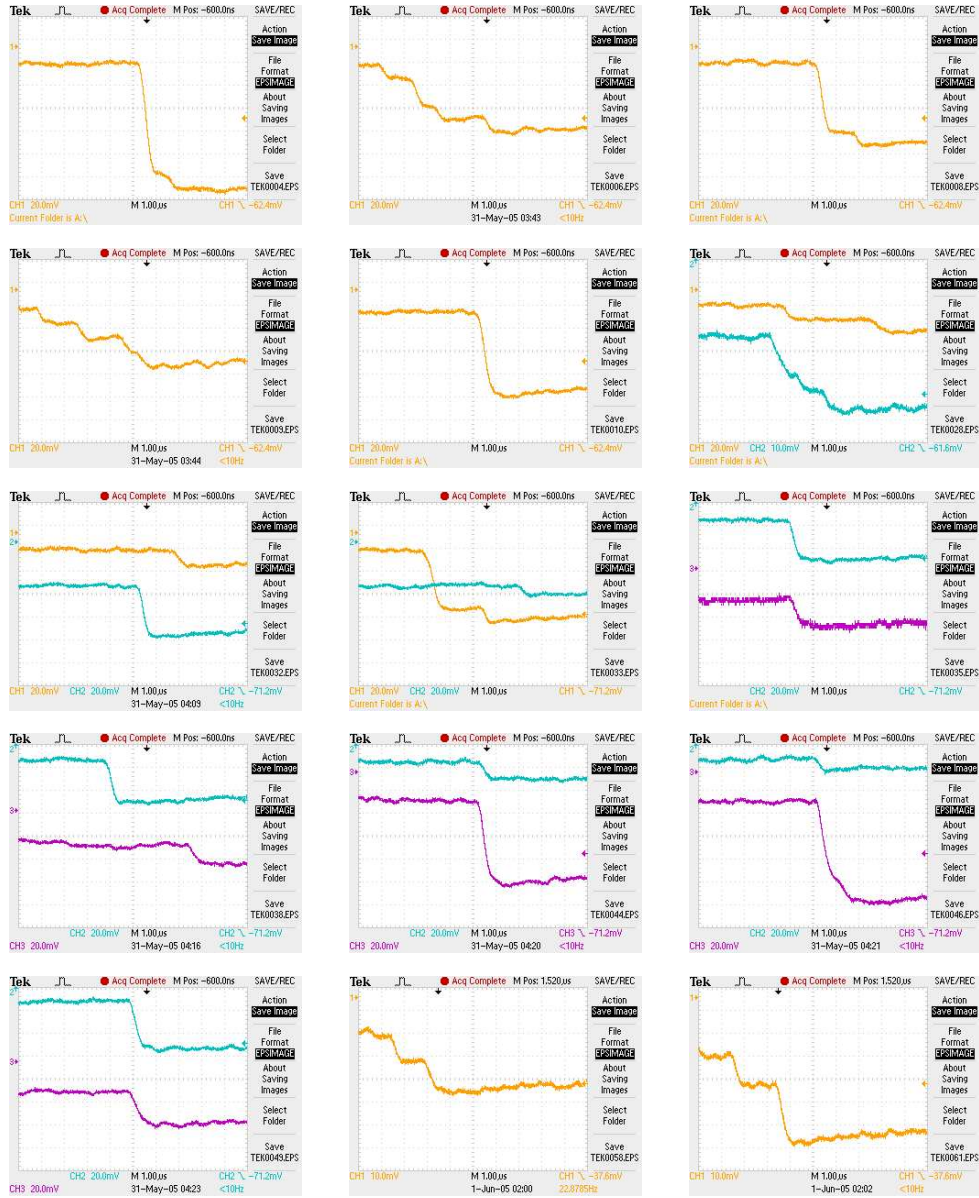


Figure B.2 An oscilloscope look. Various colors represent different segments of the detector. Electrons hit various segments at the same time, or delayed by multiples of $1 \mu\text{s}$.

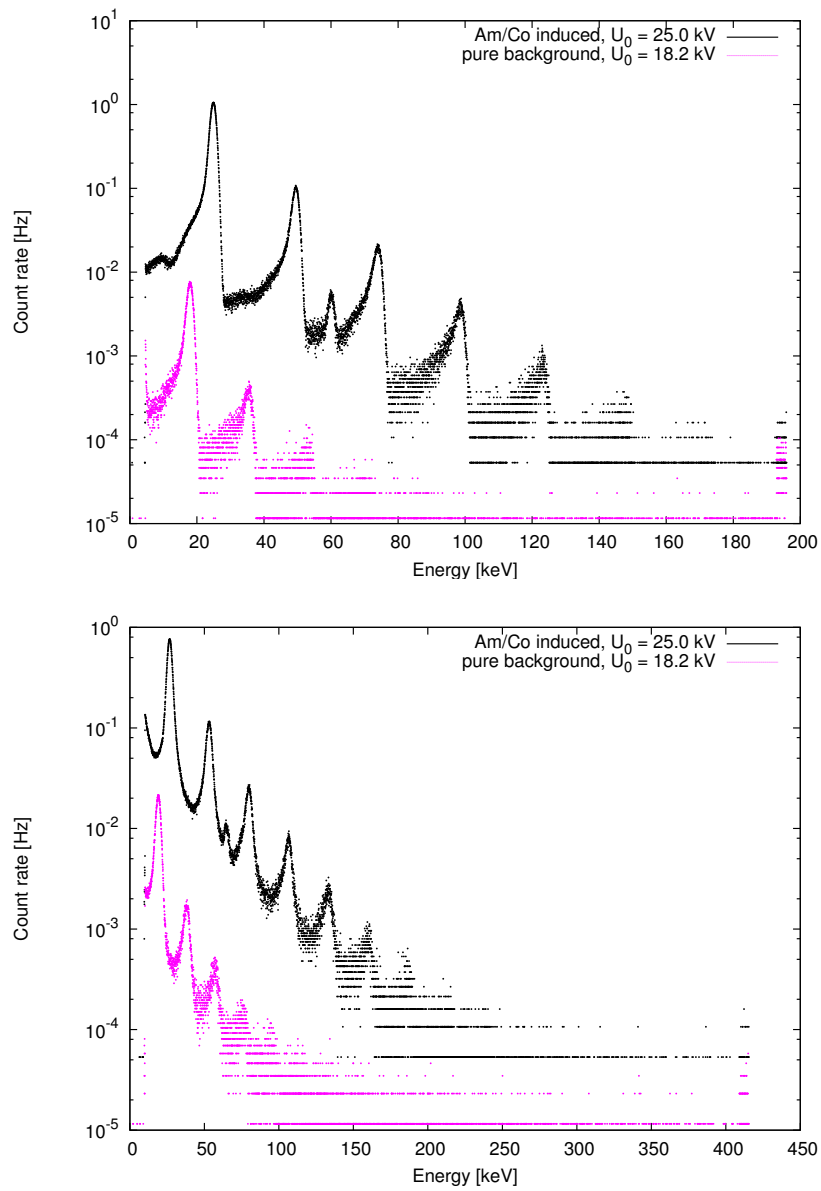


Figure B.3 The influence of count rate on the effect. The pure background measurement compared to a $^{241}\text{Am}/\text{Co}$ spectrum. Data from the first detector segment at the top, from the third one at the bottom. U_0 denotes the HV applied to the analyzing plane.

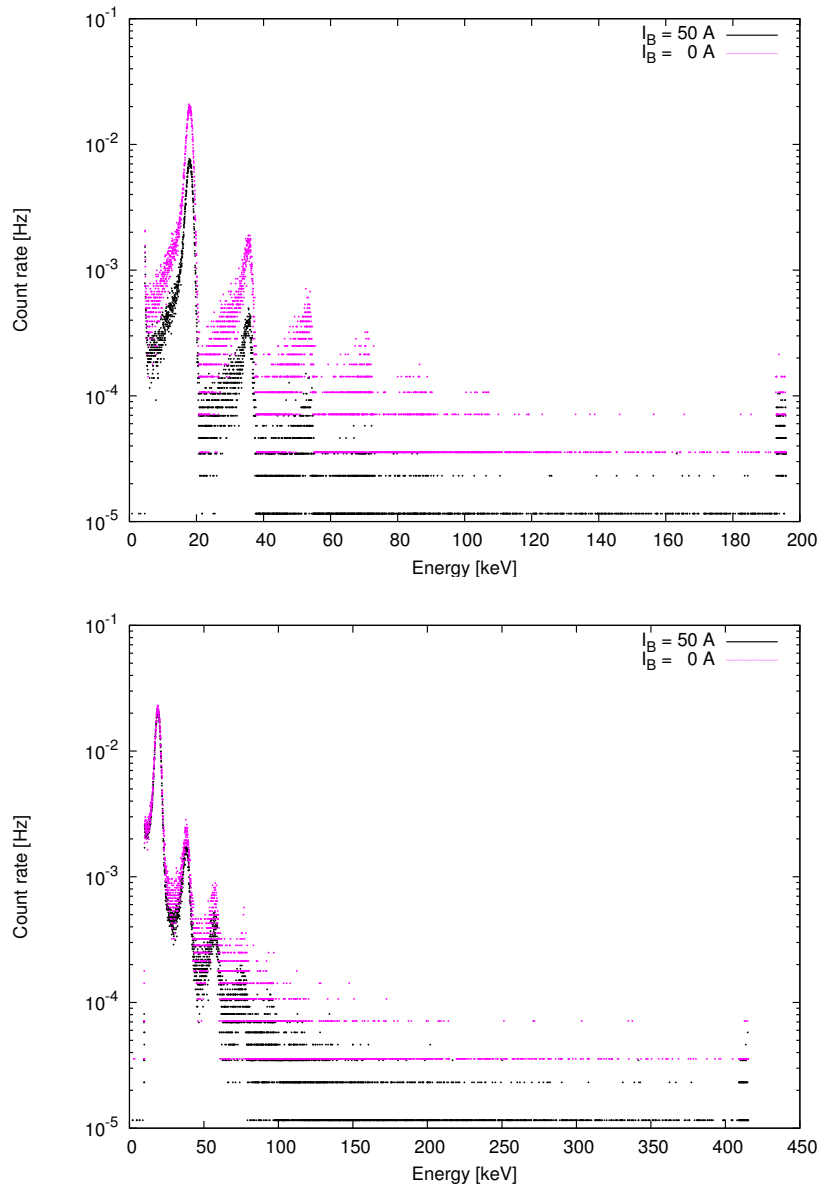


Figure B.4 The influence of possible magnetic and/or electric mirrors inside the spectrometer on the multiple background effect. Data from the first segment of the detector at the top, and the from third one at the bottom.

There is a principle question whether the multiple events energy is equal to a multiple of the retarded energy or a multiple of the $^{241}\text{Am}/\text{Co}$ electron energy. Taking into account the pure background case, the multiples of retarded energy are more probable. Anyway, a further study with a sharp electron source is welcomed.

B.3.4 Mirroring effects

Keeping the retarding voltage of 18.2 kV, we examined a possible influence of magnetic and/or electric traps. There are at least two kinds of electron traps inside the spectrometer. First, a magnetic mirror in between the pinch magnets trapping electrons born inside the spectrometer with an initial angle higher than the accepted one. Then, two electric-magnetic traps created by retarding voltage at the analyzing plane, and a pinch magnet trapping electrons born in the spectrometer with an initial angle that is not accepted to pass the pinch field, and with the initial energy too low to pass the electrical field at the analyzing plane.

Switching off the field in the magnet B, and applying a strong magnetic counter-field at the analyzing plane ($I_{\text{air}} = -10$ A) we canceled all the traps described. The comparison with the magnet B field on is shown in fig. B.4. In the both cases, pure spectrometer background was studied. These traps do not significantly contribute to the multiple events effect. (The test was done ignoring the way how to fill these traps with an appropriate number of charged particles to cause such an effect.)

B.3.5 Shaping time

The influence of shaping times of $3\ \mu\text{s}$, and $1\ \mu\text{s}$ on the effect is shown in fig. B.5. No significant differences were observed at all. Both the shaping times were too long to separate the electrons, even with a pile up regression set on. The spectrometer setup used followed the description in the section B.2 on experimental evidence.

B.3.6 Energy resolution

The dependence on energy resolution is shown in fig. B.6. Starting with the setup described in the section on experimental evidence, we varied air coils current. In particular, current of -4.00 A, -4.25 A, and -4.50 A was chosen generating magnetic field at the analyzing plane of 1.5 G, 1.3 G, and 1.1 G, respectively. Corresponding energy resolutions were 1.2 eV, 1.0 eV, and 0.9 eV at 18.6 keV. Further, these magnetic fields mapped into the first detector segment an electron beam

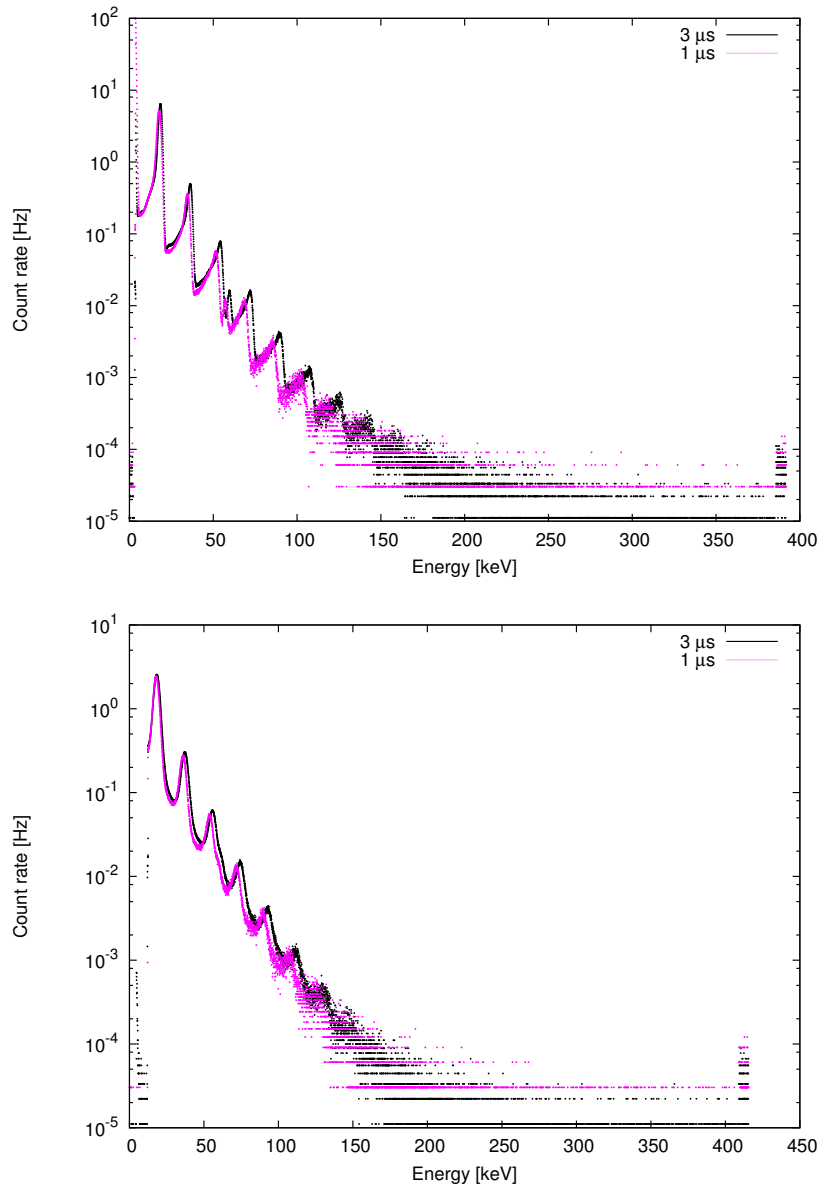


Figure B.5 The influence of shaping times of $3 \mu\text{s}$, and $1 \mu\text{s}$ on the effect. Data from the first segment of the detector at the top, and from the third one at the bottom.

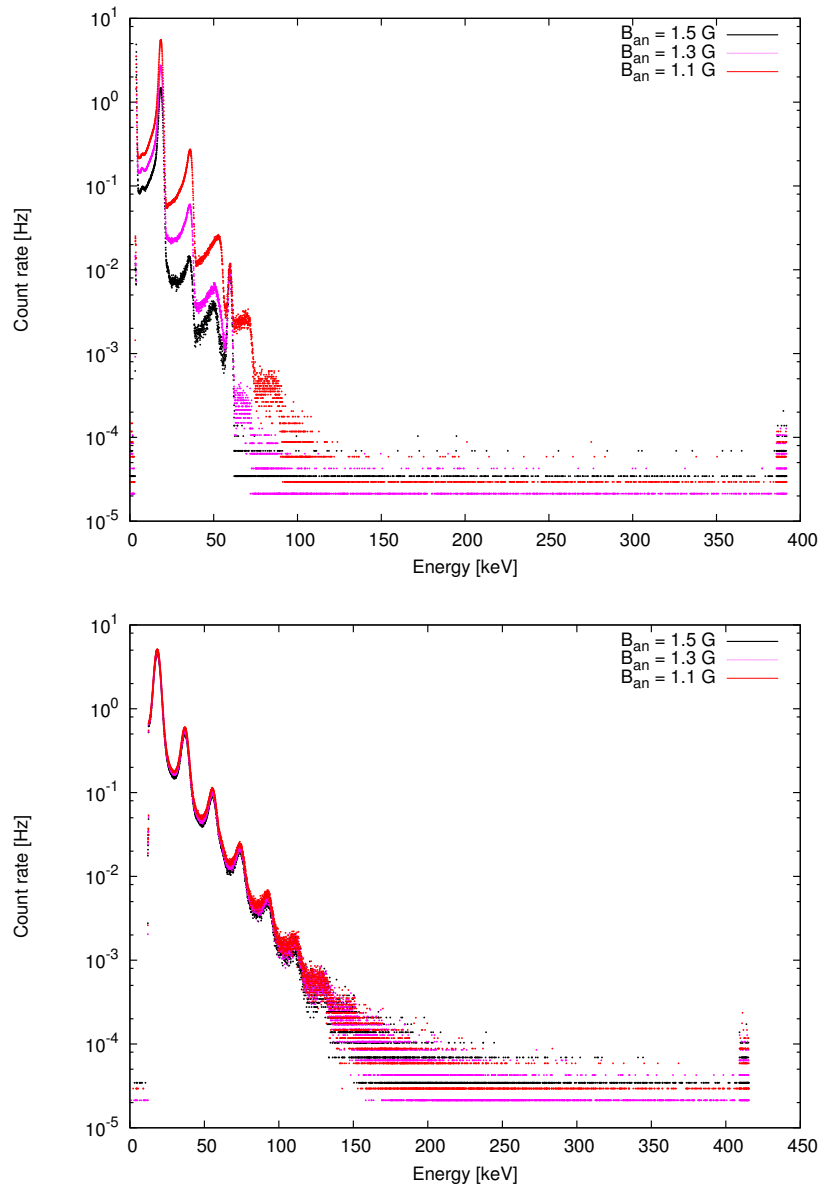


Figure B.6 The energy resolution does not influence the effect. The first segment of the detector at the top, and data from the third one at the bottom.

with diameters of 47 cm, 50 cm, and 55 cm, respectively. As for the third detector segment, a beam with diameter of 80 cm, 87 cm, and 94 cm was being mapped.

The full electrode of the spectrometer is a cylinder with diameter of 100 cm. The intermediate wired electrode is a cylinder with diameter of 89 cm. And the wired dipole electrode is, in the region concerned, a cylinder with diameter of 80 cm. So, the electrodes are directly mapped into the third segment of the detector. On the other side, no electrons born on the electrodes are adiabatically guided into the first detector segment. At least in principle.

In conclusion, better energy resolution (together with larger beam flux and worse adiabacity) enhanced the effect in the spectrometer, while it did not touched the effect on the electrodes.

B.3.7 Beam diameter

In order to disentangle the dependence on beam diameter and energy resolution we fixed the beam diameter at the analyzing plane and varied energy resolution. As for the first detector segment a beam with diameter of 47 cm was being mapped during the test. Regarding the third segment an 80 cm beam was being mapped. The reference data were measured with detector field of $B_C = 0.26$ T ($I_C = 9$ A) and air coils current of $I_{\text{air}} = -4.5$ A generating magnetic field at the analyzing plane of 1.5 G, and magnetic flux of $\Phi = 0.26$ T cm². Then we increased both the magnetic flux and the magnetic field at the analyzing plane by factor of two to $\Phi = 0.51$ T cm² and $I_C = 18$ A. (Achieved by setting the air coil current to $I_{\text{air}} = -2.44$ A resulting in magnetic field of 3.0 G.) So the beam diameter at the analyzing plane was kept constant, while energy resolution changed from 1.2 eV at 18.6 keV (the reference data) to 2.4 eV at 18.6 keV (the latter setup).

The result is shown in fig. B.7. The effect was significantly suppressed in the latter setup (especially in the first segment mapping the inner area of the spectrometer and not the electrodes). We had to increased the air coils current to $I_{\text{air}} = -3.0$ A (keeping magnetic flux at the high level of $\Phi = 0.51$ T cm²) to get an effect comparable to the reference one. That enlarged the beam diameter from 47 cm to about 50 cm and improved the energy resolution to 2.0 eV @ 18.6 keV. The result is shown in the same fig. B.7.

B.3.8 Adiabacity

To sum it up, the effect is driven by neither energy resolution nor beam diameter. Adiabacity (more precisely, a lack of adiabacity, which is a feature) can be still responsible for the effect.

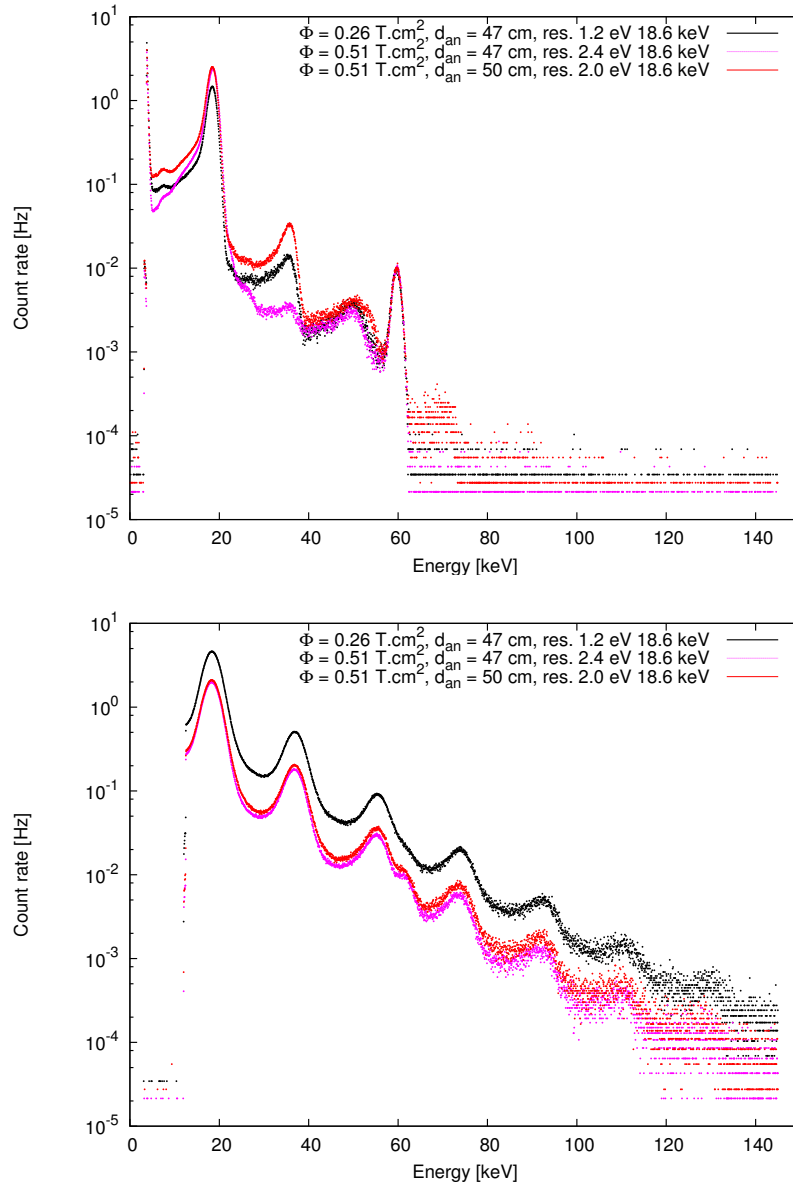


Figure B.7 Keeping the beam diameter at the analyzing plane constant and equal to 47 cm and varying energy resolution. Data from the first segment of the detector at the top, and from the third one at the bottom. The beam diameter of 50 is given for a comparison.

Keeping the magnetic flux at the high level of $\Phi = 0.51 \text{ T cm}^2$ we suppressed the effect by improving adiabacity (i.e. both worsening energy resolution and narrowing the beam diameter at the analyzing plane). In particular, air coils currents of -3.0 A , -1.5 A , -0.0 A , and $+1.5 \text{ A}$ were chosen generating magnetic fields at the analyzing plane of 2.6 G , 3.8 G , 4.9 G , and 6.1 G , respectively. Corresponding energy resolution at 18.6 keV was 1.9 eV , 2.8 eV , 3.6 eV , and 4.5 eV , respectively. Electron beams with diameters of 50 cm , 41 cm , 36 cm , and 33 cm were mapped into the first detector segment. As for the third segment of the detector, beams with diameters of 86 cm , 72 cm , 63 cm , and 57 cm were guided into the segment.

The result is shown in fig. B.8. In principle, it proved that the effect is driven by adiabacity. It is driven in a continuous way. The continuous electron spectrum emitted from Co foil by 59.6 keV gammas should be subtracted. The improved adiabacity allows high energy electrons (compared to retarded energy of 18.6 keV) to be mapped into the detector.

B.3.9 Screening voltage

Finally, we applied screening voltage to both the intermediate cylindrical grid and the dipole electrode. Screening voltage values of $+5 \text{ V}$, $+10 \text{ V}$, and $+15 \text{ V}$ (with respect to the analyzing voltage) were picked up. These prevent low energy electrons created in the electrodes to penetrate into the spectrometer. The air coils current was fixed to -4.0 A , generating magnetic field of 1.8 G , and resulting in energy resolution of 1.3 eV at 18.6 keV . The result is shown in fig. B.9. Screening voltage can cure the effect.

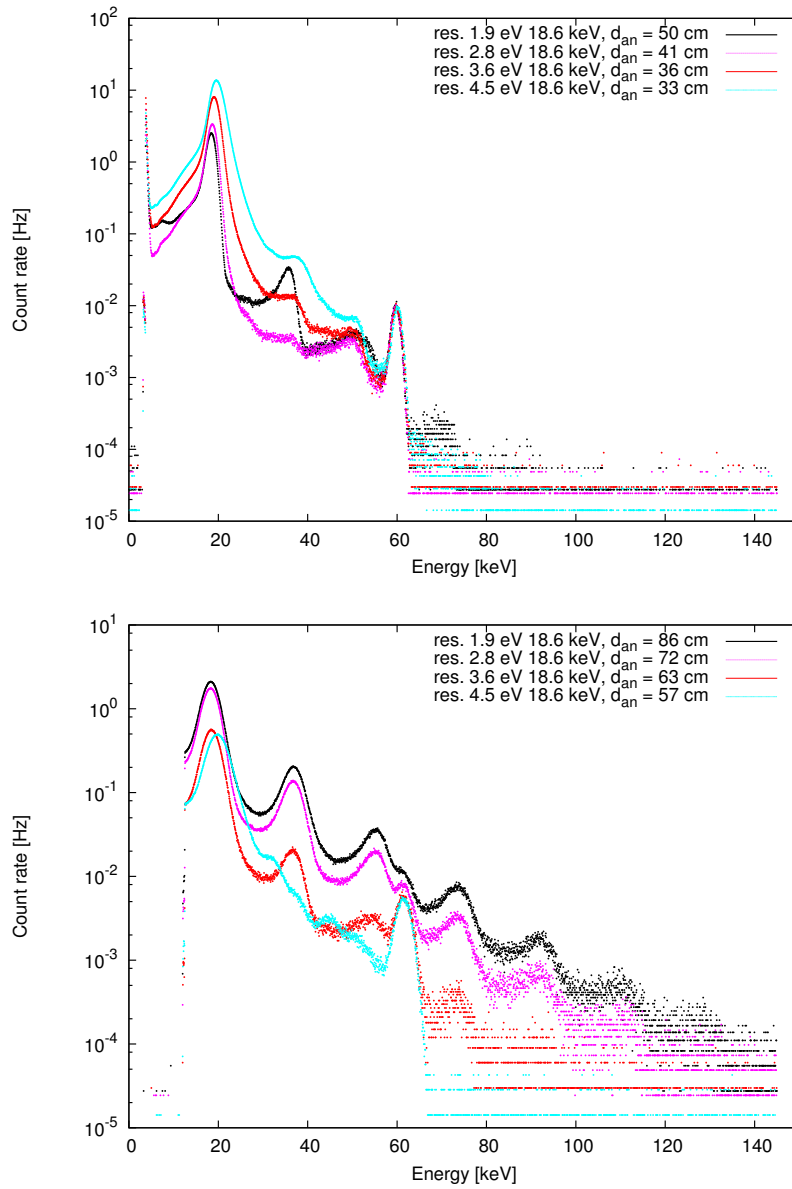


Figure B.8 Suppressing the effect by improved adiabatic conditions along a magnetic field line. Data from the first segment of the detector at the top, and from the third one at the bottom.

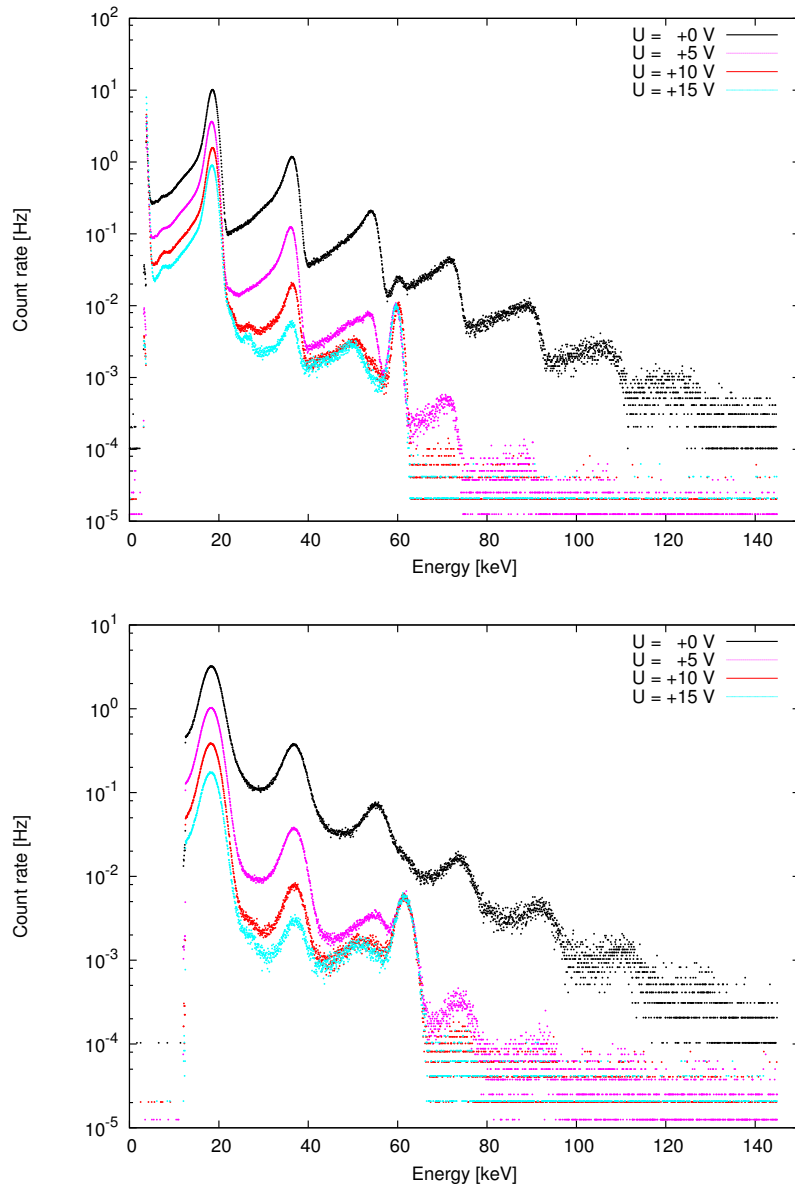


Figure B.9 Applying screening voltage to the grid electrodes suppressed the effect. Data from the first segment of the detector at the top, and from the third one at the bottom.

B.4 True secondary electrons

True secondary electrons are possibly appropriate candidates to explain the effect. They are easy to produce in sufficient amounts with a reasonable price. Let us introduce the secondary electron emission process.

When a steady current of electrons impinges on a surface, a certain portion is reflected elastically while the rest penetrates into the material. Some of these electrons scatter from the material and are reflected back out. These are called “rediffused” electrons. The rest of the electrons interact in a more complicated way with the material and yield the so-called “true secondary electrons”. Two main quantities used in the study of the secondary electron emission process are the secondary electron yield δ and the emitted-energy spectrum $d\delta/dE$. An example of such spectrum induced by a electrons with incident energy of $E_0 = 200$ eV hitting a stainless steel surface in perpendicular direction (normal incidence) is shown in fig. B.10.

In the following, we will focus on the true secondary electrons. To describe the emission process we adopt the phenomenological probabilistic model developed in [39]. Set of parameters for stainless steel surface was used [39]. A surface treatment and/or contamination may change the model parameters substantially.

B.4.1 Probability of the process

First, the probability of an incident electron to emit true secondary electrons was simulated. The dependence of the probability on incident angle is shown in fig. B.11 for several energies of the incident electron. Also shown is the dependence on energy of the incident electron is shown for several incident angles.

B.4.1.1 Yield per incident electron

Then, the true secondary electron yield *per incident electron* is shown in fig. B.12. Again, the dependences on both the incident angle and the incident energy is shown.

B.4.1.2 Yield per penetrated electron

Finally, the yield *per penetrated electron* is shown in fig. B.13. As usual, the dependences on both the incident angle and the incident energy is shown. It is possible to produce tens of electrons at once.

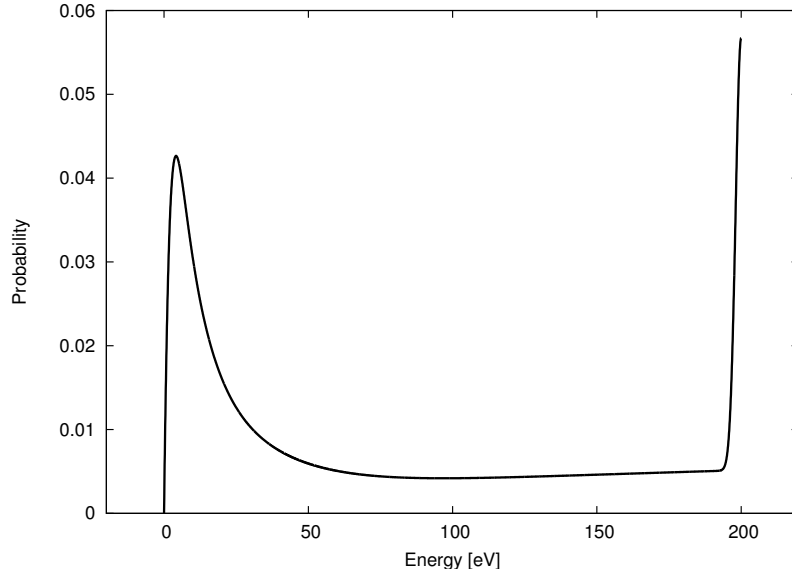


Figure B.10 A simulated example of energy spectrum of the secondary electron emission spectrum for a normal incidence at incident energy of $E_0 = 200$ eV. A stainless steel surface was assumed as described in [39].

B.4.2 A simulation mockup

Having few tens of electrons produced at once on an electrode of the spectrometer, we need to guide them into the detector. First, the true secondary electrons have to bind on a magnetic field line leading to the detector. Most probably, this is a nonadiabatic process probably driven by plasmons. The way the nonadiabatic process runs is completely unclear.

Then, some of them are reflected by the high magnetic field (to conserve their angular momentum). Not many of them. All the electrons born with energy lower than the energy resolution of the spectrometer are completely free to pass the high magnetic field. Even, if the initial energy is higher than energy resolution, the maximum accepted angle is pretty high.

As for the electrons reflected by the high magnetic field, they may hit an electrode of the spectrometer again. Hopefully, the probability of the process is the same as of the reverse process already undergone. Then, the electrons may scatter from the material. And they can try again to bind on a field line. These electrons would hit the detector about $1 \mu\text{s}$ later. The process described may be repeated several times, if the nonadiabatic process assumed is both probable (in wide ranges of angles and energies) and cheap with respect to the energy paid.

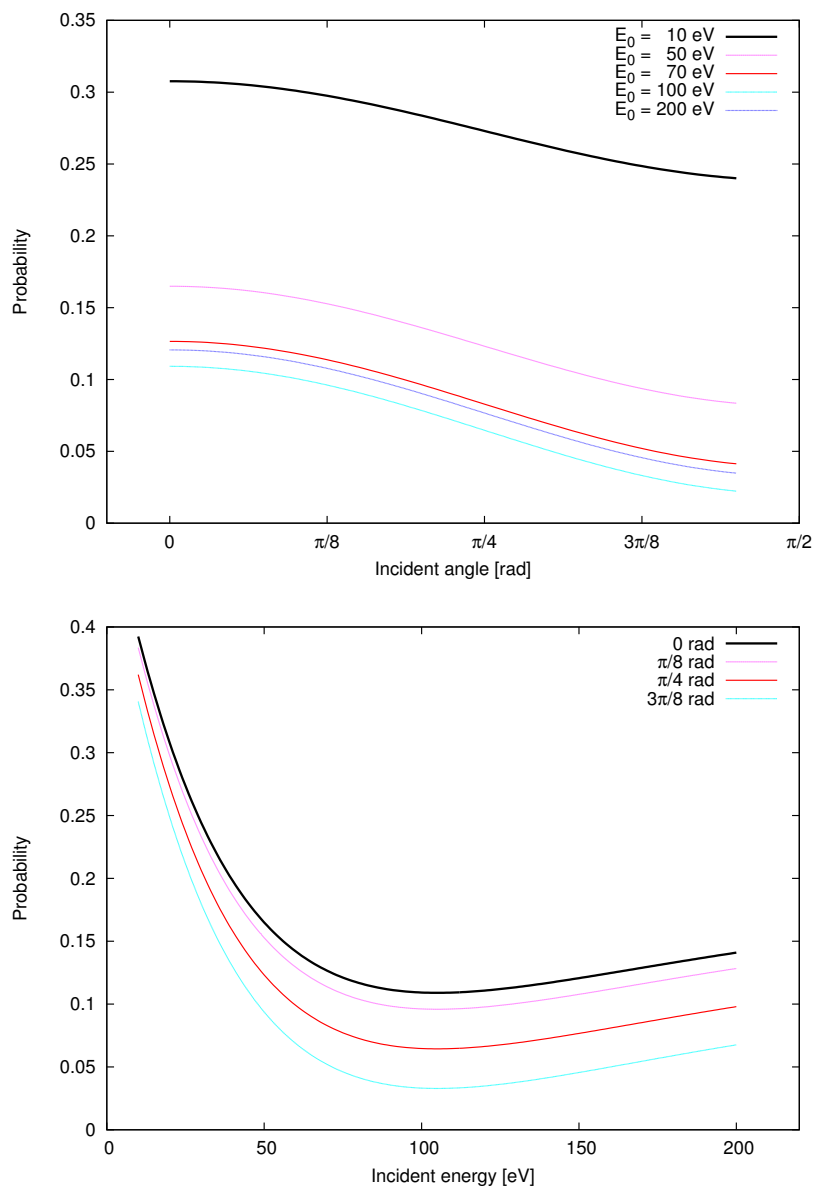


Figure B.11 Simulated probability of the true secondary electron emission process. The dependence on incident angle on the top, the incident energy dependence at the bottom.

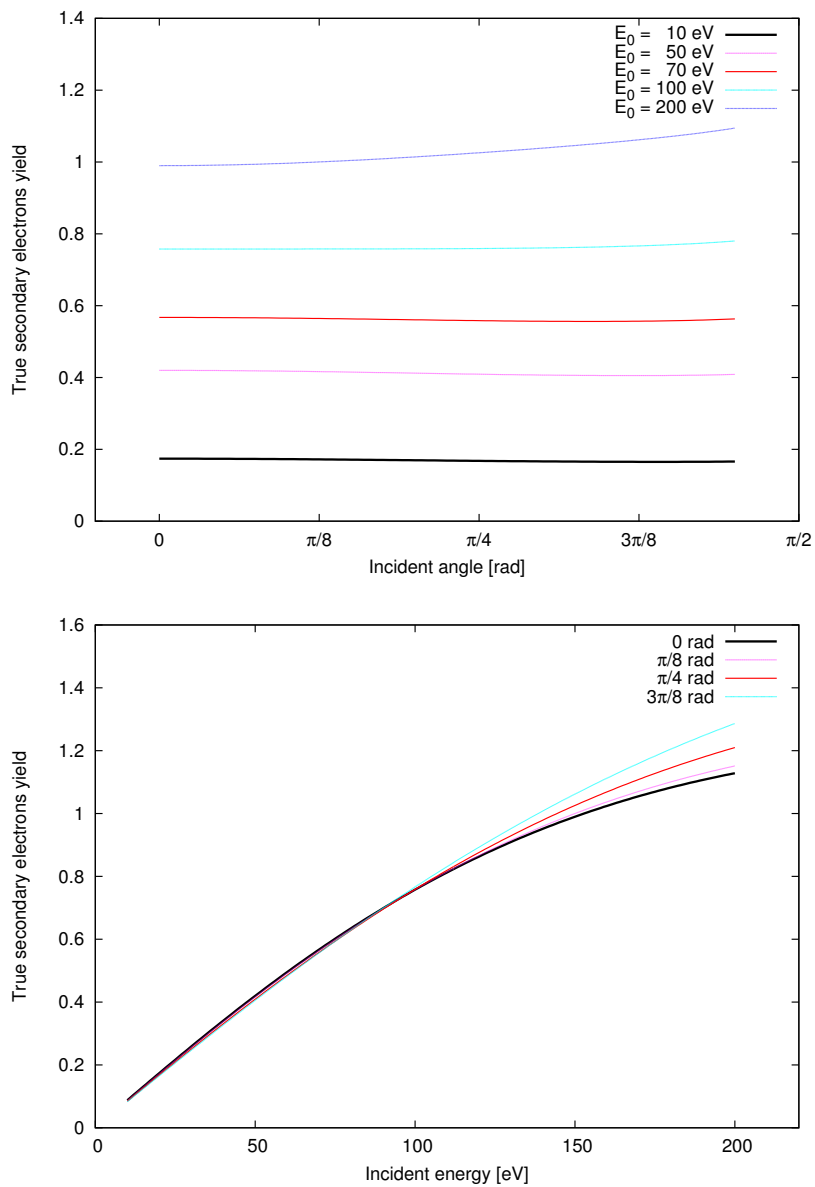


Figure B.12 True secondary electron yield *per incident electron*. The simulated dependence on incident angle on the top, the incident energy dependence at the bottom.

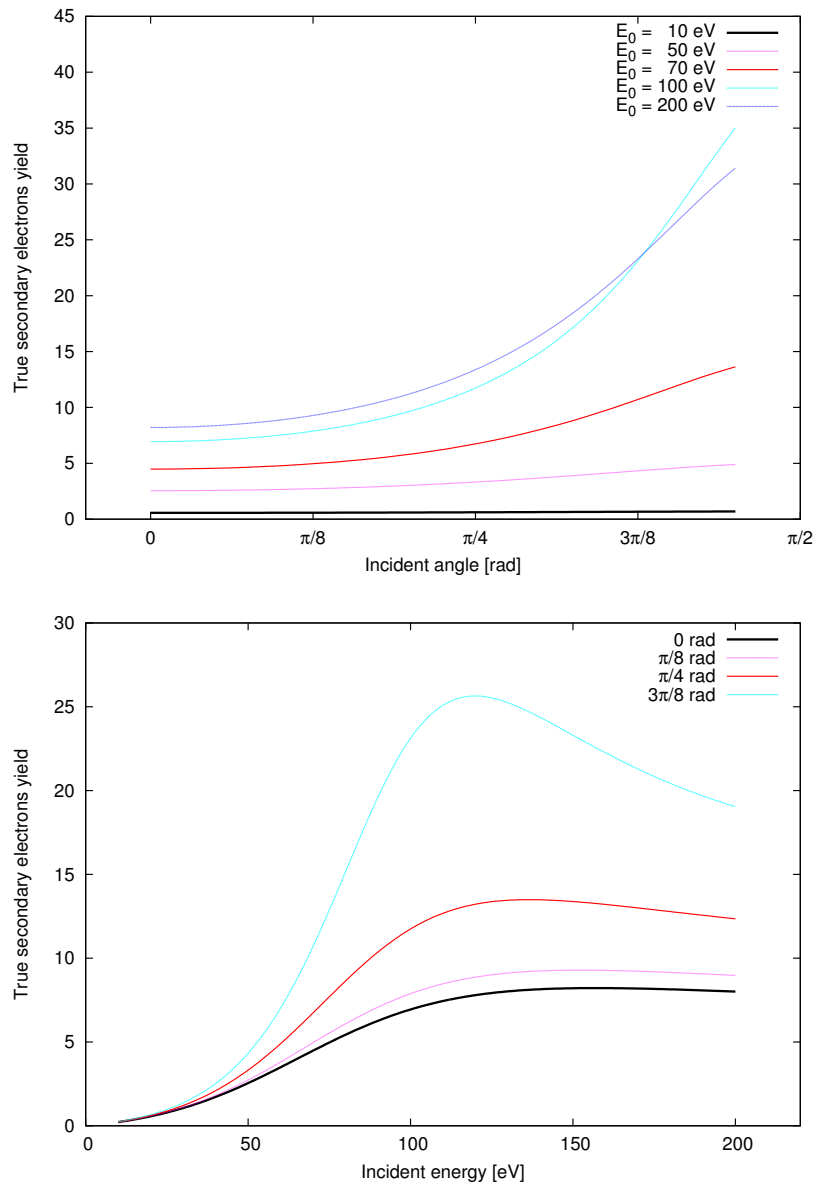


Figure B.13 True secondary electron yield *per penetrated electron*. The simulated dependence on incident angle on the top, the incident energy dependence at the bottom.

B.5 Conclusion

Multiple background events were studied in this section. The process is driven by lack of adiabaticity. True secondary electrons were suggested to take responsibility for the effect. A simulation design of the process was offered. The simulation is limited by an unknown nonadiabatic process to bind the true secondary electrons on magnetic field lines guiding to the detector.

Further studies with a sharp electron source could focus on the threshold energy of the process (the minimum energy paid to produce the true secondary electrons and guide them in the detector).

References

- [1] R.N. Mohapatra *et al.* Theory of Neutrinos: A White Paper. arXiv.org/abs/hep-ph/0510213, 2005
- [2] American Physical Society. The neutrino matrix. <http://www.aps.org/neutrino>, 2005
- [3] The ALEPH, DELPHI, L3, OPAL, SLD Collaborations, the LEP Electroweak Working Group and the SLD Electroweak and Heavy Flavour Groups. arXiv:hep-ex/0509008v3, 2006
- [4] R.N. Mohapatra and A.Yu. Smirnov. Neutrino Mass and New Physics. arXiv:hep-ph/0603118v2, 2006
- [5] A.A. Aguilar-Arevalo *et al.* (MiniBooNE Collaboration). arXiv:0704.1500v3, 2007
- [6] A. Goobar, S. Hannestad *et al.* The neutrino mass bound from WMAP-3, the baryon acoustic peak, the SNLS supernovae and the Lyman- α forest. arXiv.org/abs/astro-ph/0602155, 2006
- [7] P.D. Serpico. arXiv:astro-ph/0701699v2, 2007
- [8] H.V. Klapdor-Kleingrothaus, A. Dietz, I.V. Krivosheina and O. Chkvorets. *Phys. Lett. B*, 586:198, 2004.
- [9] A. Nucciotti. Double Beta Decay: Experiments and Theory Review. arXiv:0707.2216v3, 2007
- [10] Ch. Kraus *et al.* *Eur. Phys. J.*, C40:447-468, 2005.
- [11] V.M. Lobashev. The search for the neutrino mass by direct method in the tritium beta-decay and perspectives of study it in the project KATRIN. *Nucl. Phys. A*, 719:153c, 2003.
- [12] J. Angrik *et al.* (KATRIN collaboration). KATRIN design report 2004. FZKA Scientific Report 7090, 2005 <http://www.fzk.de/katrin/>.
- [13] A. Osipowicz *et al.* (KATRIN Collaboration). arXiv:hep-ex/0109033, 2001
- [14] T. Thümmler *et al.* (KATRIN Collaboration). Addendum to the Letter of Intent. <http://www.fzk.de/katrin/>, 2002
- [15] J.D. Jackson. *Classical Electrodynamics*. Wiley, New York, 3rd edition, 1999.

- [16] V.N. Aseev *et al.* *Eur. Phys. J. D*, 10:39–52, 2000.
- [17] J. Kaspar. *Influence of energy scale imperfections on neutrino mass sensitivity in the KATRIN experiment*. Diploma thesis, Czech Technical University, 2003. <http://www.fzk.de/katrin/>.
- [18] R.G.H. Robertson and D.A. Knapp. *Ann. Rev. Nucl. Part. Sci.*, 38:185, 1988.
- [19] T. Thümmeler. Status & Perspectives of HV and Calibration. KATRIN internal document *95-TRP-4248-S6*, 2007
- [20] A. Picard *et al.* *Z. Phys.*, A342:71, 1992.
- [21] E.G. Kessler, Jr. private communication. 2002
- [22] R.G. Helmer and C. van der Lauen. *Nucl. Instr. and Meth.*, A450:35, 2000.
- [23] R. D. Deslattes *et al.* *Rev. Mod. Phys.*, 75:3, 2003.
- [24] O. Dragoun, M. Ryšavý and A. Špalek. Statistical tests of invariability of measurement conditions in the beta-ray spectroscopy. *Nucl. Instr. Meth.*, A391:345, 1997.
- [25] D.W.O. Rodgers. *Nucl. Instr. Meth.*, 127:253–260, 1975.
- [26] M. Ryšavý and J. Kaspar. *Nucl. Instr. Meth. A*, 2008 Accepted paper, doi:10.1016/j.nima.2008.03.101.
- [27] S. Baker and R.D. Cousins. *Nucl. Instr. Meth.*, 221:437, 1984.
- [28] F.M.L. Almeida Jr., M. Barli and M.A.B. do Vale. *Nucl. Instr. Meth.*, A449:383, 2000.
- [29] A. Kovalik and V.M. Gorozhankin. *J. Phys. G: Nucl. Part. Phys.*, 19:1921–1927, 1993.
- [30] High Tech Sources Limited. <http://www.hightechsource.co.uk/>, 2007
- [31] O. Dragoun *et al.* *Nucl. Instr. and Meth.*, B194:112, 2002.
- [32] A. Spalek *et al.* *Nucl. Instr. Meth.*, A438:433, 1999.
- [33] B. Müller. Diploma Thesis. Johannes Gutenberg-Universität in Mainz, 2002
- [34] B. Flatt. PhD Thesis. Johannes Gutenberg-Universität in Mainz, 2004
- [35] B. Bornschein. PhD Thesis. Johannes Gutenberg-Universität in Mainz, 2000
- [36] N. Dragounova. *IEEE Trans. Instr. Meas.*, 54:1911, 2005.
- [37] E. Otten and CH. Kraus. On self calibration of the inelastic T2- β -spectrum and correlations of fit parameters. KATRIN internal document *65-ME-4005-1*, 2003

- [38] J. Bonn. Private talk. 2005
- [39] M.A. Furman and M.T.F. Pivi. Simulation of secondary electron emission based on a phenomenological probabilistic model. report *LBL-52807*, 2003

Acknowledgement

This thesis would not have been written without help of my wife, my parents, and colleagues. I would like to thank them very much for it.

In particular, I am most grateful to my supervisor O. Dragoun, who has learnt me being a physicist. I appreciate a lot the time he spent with me.

I am grateful to J. Bonn for sharing his experience, a lot of assistance, and many ideas. I would like to thank E. Otten for valuable discussions and financial support.

A. Kovalik took part in Am/Co and Rb/Kr measurements in Mainz. I appreciate it.

I would like to thank to D. Venos who designed the source part to house the Am/Co source in the Mainz spectrometer, took part in the first Am/Co measurements, and together with A. Spalek prepared Rb/Kr sources to check the performance of the Mainz spectrometer.

A. Spalek also wrote a MC code to understand the Am/Co source. Thank you.

I am grateful to M. Rysavy for many discussions on statistical methods and data evaluation.

Many thanks go to N. Dragounova, who kept the ESA12 spectrometer running during the Am/Co measurements.

I would like to thank B. Flatt for an introduction to the Mainz spectrometer, and F. Glueck who wrote a code to calculate both magnetic and electric field maps of the Mainz spectrometer.

And above all, thank you to my wife for always believing in me, and for her patience.

